Fault Analysis and Protection for Wind Power Generation Systems

Jin Yang

Submitted in fulfilment of the requirements for
the degree of Doctor of Philosophy (Ph.D.)

Electronics and Electrical Engineering
School of Engineering
College of Science and Engineering
University of Glasgow

March 2011

To my family ...

Abstract

Wind power is growing rapidly around the world as a means of dealing with the world energy shortage and associated environmental problems. Ambitious plans concerning renewable energy applications around European countries require a reliable yet economic system to generate, collect and transmit electrical power from renewable resources. In populous Europe, collective offshore large-scale wind farms are efficient and have the potential to reach this sustainable goal. This means that an even more reliable collection and transmission system is sought. However, this relatively new area of offshore wind power generation lacks systematic fault transient analysis and operational experience to enhance further development. At the same time, appropriate fault protection schemes are required.

This thesis focuses on the analysis of fault conditions and investigates effective fault ride-through and protection schemes in the electrical systems of wind farms, for both small-scale land and large-scale offshore systems. Two variable-speed generation systems are considered: doubly-fed induction generators (DFIGs) and permanent magnet synchronous generators (PMSGs) because of their popularity nowadays for wind turbines scaling to several-MW systems. The main content of the thesis is as follows. The protection issues of DFIGs are discussed, with a novel protection scheme proposed. Then the analysis of protection scheme options for the fully rated converter, direct-driven PMSGs are examined and performed with simulation comparisons. Further, the protection schemes for wind farm collection and transmission systems are studied in terms of voltage level, collection level – wind farm collection grids and high-voltage transmission systems for multi-terminal DC connected transmission systems, the so-called “Supergrid”. Throughout the thesis, theoretical analyses of fault transient performances are detailed with PSCAD/EMTDC simulation results for verification. Finally, the economic aspect for possible redundant design of wind farm electrical systems is investigated based on operational and economic statistics from an example wind farm project.

Acknowledgements

Firstly, I would like to express the deepest gratitude to my supervisor Professor John O'Reilly for taking me under supervision after changes to my Ph.D. study. He is so kind in his support and advice. I would also like to thank my second supervisor Dr. John E. Fletcher formerly at the University of Strathclyde (now with the University of New South Wales, Sydney, Australia) for much technical guidance. Thanks also to Dr. David G. Dorrell (now with the University of Technology, Sydney, Australia) for giving me this opportunity to pursue a Ph.D. degree at the University of Glasgow.

The financial support for this research project given by the Scottish Funding Council in name of Glasgow Research Partnership in Engineering (GRPE) is gratefully acknowledged. Thanks are also due to the Department of Electronics and Electrical Engineering for support in academic visits, in particular Professor John M. Arnold and Dr. Scott Roy.

Further, many thanks go to my friends and colleagues in the Power System and Power Electronics Group in Electronics and Electrical Engineering, especially Ms. Laura Nicholson, Mr. Sze Song Ngu, Mr. Majid Mumtaz, and Mr. Bazad Kazemtabrizi, for making the working environment enjoyable. I would like to thank the project group at the University of Strathclyde, consisting of Dr. Huibin Zhang, Mr. Shixiong Fan, and Mr. Yuanye Xia. They are all gratefully acknowledged for providing valuable input during the project.

Finally, I would like to thank my family for their love and support throughout.

Table of Contents

List of Figures

List of Tables

Abbreviations and Nomenclature

CB	Circuit Breaker
CG	Collection Grid
CSC	Current-Source Converter
DFIG	Doubly-Fed Induction Generator
DNO	Distribution Network Operator
ETO	Emitter Turn-Off device
FRT	Fault Ride-Through
GSC	Grid-Side Converter
GTO	Gate Turn-Off thyristor
HVAC	High-Voltage Alternative Current
HVDC	High-Voltage Direct Current
IG	Induction Generator
IGBT	Insulated-Gate Bipolar Thyristor
MPPT	Maximum Power Point Tracking
PMSG	Permanent Magnet Synchronous Generator
PWM	Pulse-Width Modulation
RSC	Rotor-Side Converter
SDR	Series Dynamic Resistor
SSCB	Solid-State Circuit Breaker
TNO	Transmission Network Operator
VSC	Voltage-Source Converter
VSCF	Variable-Speed Constant-Frequency
VSI	Voltage-Source Inverter
WPGS	Wind Power Generation System

Wind Turbine

P_m	Mechanical output power.
λ	Tip-speed ratio.
C_p	Performance coefficient.
β	Blade pitch angle.
V_{wind}	Wind speed.

Induction Generator

$\vec{v}$, $\vec{i}$, $\vec{\psi}$	Voltage, current and flux vectors.
V_s, V_r	Stator, rotor voltage amplitudes.
R_s, R_r	Stator, rotor resistances.
L_s, L_r, L_{ls}, L_{lr}	Stator, rotor self- and leakage inductances.
L_m	Magnetising inductance.
s	Rotor slip.
ω_s, ω_r, $s\omega_s$	Synchronous, rotor and slip angular frequencies.
τ_s, τ_r, τ	Stator, rotor and combined time constants.
P_s, Q_s	Stator side active and reactive power.
s, r	Stator and rotor value subscripts.
n	Nominal value subscript.
d, q	d- and q-axis value subscripts.
ref	Reference value superscript.

Permanent Magnet Synchronous Generator

P_n	Rated power.
V_{sn}	Rated stator voltage amplitude.
R_s	Stator winding phase resistance.
L_s	Stator winding phase inductance.

Chapter 1

Introduction

1.1 Wind Energy Industry

Wind, as a well-known renewable energy resource, has stood out to be one of the most promising alternative sources of electrical power. It is environmentally friendly and has the possibility of large-scale implementation in offshore scenarios. The British Wind Energy Association has performed a quantitative assessment of the reduction in emissions [1.1] and hypothetical studies have been performed in Ireland [1.2] and both studies show considerable CO_2, SO_2 and NO_X reductions with increasing installed wind capacity. Wind generation should also be combined with alternative emission reduction measures such as emission taxes or trading schemes, substitution of fossil fuelled plant, and demand reduction schemes.

Wind power is being promoted in many countries by way of government-level policy and established by real commercial generation projects. Large-scale offshore wind farms are planned, especially in Europe, where shallow-water and offshore wind resources are numerous. By 2020, it is planned that 20% of power consumed in Europe may well be supplied by renewable resources. The realisation of this ambitious plan relies heavily on large-scale offshore wind farm operation. Using the UK as an example, in the 2020 target, offshore wind farms will need to contribute as much as 9.4% of the total installed power capacity [1.3]. Europe is now planning for more than 30 GW in offshore wind farm capacity by 2015 - almost 30 times more than currently installed [1.4], [1.5]. Other countries also have promising offshore wind power resources, including China and the USA. Moreover, population centres along coastlines in many parts of the world are close to offshore wind resources, which would reduce wind power transmission costs. Therefore, the reliability of offshore wind farms needs to be assessed in detail because of the costly maintenance

and repair in the offshore environment. The reliability is distributed between the wind turbines, the wind power generation systems, the collection grids and the transmission systems [1.6].

In addition, in terms of existing power networks, transmission network operators (TNOs) and distribution network operators (DNOs) are having to reinforce networks, due to the considerable penetration of wind power into the onshore transmission and distribution systems. In the UK, a "Path to Power" project was undertaken in 2006 with the Stage 3 – GB Electricity Network Access [1.7]. The main focus is to minimise costly network reinforcements by gradually replacing conventional fossil-fuelled power plants with renewable power generations. During the first period (2006-2010), it was necessary to study and optimise the wind power electrical system to minimise its influence on the grid. During the second period (2010-2015), deployment of significant projects with large-scale wind turbine arrays with commercially proven technologies will take place. The third period (2015-2020) will see wider project deployment.

Wind power technologies have been rapidly developed since 1980s with growing practical applications. Research areas are focused on the following aspects: 1) wind power conversion technologies [1.8]-[1.13]; 2) power transmission technologies [1.14]-[1.18]; and 3) high-power conversion technologies [1.19]-[1.22] for offshore large-scale wind farm applications. The current development of wind power technologies is presented to demonstrate the state of the art and to provide a justification for the research undertaken. In Section 1.3, two popular variable-speed wind power generation systems are summarised. Existing wind power collection and transmission technologies are presented in Section 1.4 along with promising power conversion technologies. In Section 1.5, the development of emerging DC network protection issues is summarised. This forms the background of the research and motivation for research into protection of wind power generation systems. The research described in this thesis addresses the challenges of protecting wind turbines and associated capture networks, particularly networks that utilise DC interconnections. A thesis outline and list of publications are given after the literature review.

1.2 Objectives and Motivation of the Thesis

In this thesis, wind power generation systems are the research topic. Wind power generation system is defined here as the system of equipment and devices used in the conversion, capture and transmission of energy, including electromechanical generators and power conversion and transmission devices, such as converters and cables. Both large-scale systems used for offshore wind farms and small-scale systems used for distribution systems or micro-grids are discussed. The former is the major goal of the study, while the latter is related to the realisation of a demonstration system for a TSB/EPSRC collaborative research project which has partly funded this research work. The research is focused on protecting wind farm devices and thereby reducing their influence on the onshore grid during faults, analysing the electrical transients in wind power generation systems during faults, and providing design methods for effective protection schemes. System performance will be assessed in relation to the fault ride-through (FRT) grid code requirements. The system performance under grid faults and wind farm faults are analysed in detail to inform the protection scheme design.

Instead of addressing many types of wind turbine generation systems, for example [1.10], the project will focus on the most popular doubly-fed induction generators (DFIGs) and promising fully rated converter permanent magnet synchronous generators (PMSGs). These are likely to form the basic generation components of future large-scale offshore wind turbines. It is assumed that the offshore wind farm is connected to the onshore grid by DC transmission cables [1.16]. This is by no means assured as there are other competitive technologies, but the concept of a high-voltage direct-current (HVDC) Supergrid for Europe is under consideration, and therefore the research reported here is timely and contributes to this discussion. Currently, most wind farms in operation use alternating current systems, which offer a mature technology with over a hundred years of operational experience. However, the research detailed here investigates a topology using a DC medium/low voltage collection grid and high-voltage multi- voltage-source converter (VSC) based transmission technology for large-scale wind power integration, in particular in the offshore environment. Nevertheless, there are still some critical economic and

technical challenges to address: the costs and losses of power electronic devices; and the topology, allocation, and coordination of DC circuit breakers.

As with all engineering systems, the design of a wind farm, including the choice of components and topologies involves a trade-off between the technical specifications and the economic costs. The operational purpose that only requires wind power to be "available" instead of "reliable", and huge cost of offshore wind farms make the economic factor dominant. That should be why there is an "availability" consideration in wind farm design instead of "reliability" in conventional utility substation and infrastructure design. For the utility grids, it is critical to provide electricity continuously and securely to consumers, with reliability, while the wind farm generation system is only a source of energy. If the stage of wind power development is such that it has a limited penetration, the focus is on efficiency of delivery. That means having "available" wind power might be sufficient.

However, this is not the case in large-scale offshore wind farms. A Swedish wind power plant failure survey [1.23] demonstrated that 23% of failures between 2000 and 2004 happened in the wind farm electrical system (including that of generators), ranking it first among wind farm components (compared to drive train, gearboxes, control systems, structure, sensors and so on). It also contributes 23.2% of the total down-time, ranking it first followed by gears and control systems. The survey also included statistics from Germany and France, with similar results. From the statistical data it can be seen that transient stability and reliability analysis of the electrical system are urgently required during the wind farm planning and design phases. In fact, the gearbox and control system failures are partially due to the failures of the electrical systems which can cause electrical torque fluctuations, and also mechanical damage in the gearbox and bearing system. This makes the analysis of electrical systems even more critical.

The survey was not dedicated to large-scale offshore turbines and no details about which parts of the electrical system failed are provided. Nevertheless, the electrical system when subject to the harsh offshore environment can greatly influence the power production and performance. The lack of failure statistics for large-scale offshore wind farms is due to operational inexperience in this relatively new industry.

However, with the increasing capacity of offshore wind farms in planning and construction, and the requirements for fault ride-through capability in the grid codes of many countries, it is urgently required to enhance the understanding of reliability and stability of offshore wind farms, for which the maintenance and repair are expensive and difficult to schedule.

1.3 Wind Power Generation Systems

At present, two popular variable-speed constant-frequency wind power generation systems dominate. They are the doubly-fed induction generator (DFIG) and the permanent magnet synchronous generator (PMSG). This section will introduce the basic wind turbine variable-speed features, generation system power converters and their associated control systems, and current research development of the two systems for wind power applications.

1.3.1 Doubly-Fed Induction Generators

The DFIG is currently the system of choice for multi-megawatt wind turbines [1.10]. If the aerodynamic system is capable of operating over a wide wind speed range then optimal aerodynamic efficiency can be achieved by tracking the optimum tip-speed ratio. Therefore, the generator's rotor should be able to operate at a variable rotational speed. The DFIG system provides this facility by operating in both sub- and super-synchronous modes with a rotor speed range around the synchronous speed. The stator circuit is connected to the grid while the rotor winding is connected via slip-rings to an AC/DC/AC three-phase converter arrangement. For variable-speed systems where the speed range requirements are modest, for example ±30% of synchronous speed, the DFIG offers adequate performance and is sufficient for the speed range required to exploit typical wind resources.

1) DFIG Topology

The AC/DC/AC converter connecting the rotor windings to the grid consists of two voltage-source converters, i.e., rotor-side converter (RSC) and grid-side converter (GSC), which are connected "back-to-back", shown in Figure 1.1. Between the two

converters a DC-link capacitor is placed, as energy storage, in order to keep the voltage variations (or ripple) in the DC-link voltage small. With the rotor-side converter it is possible to control the shaft torque or the speed of the DFIG and also the power factor at the stator terminals. The main objective for the grid-side converter is to keep the DC-link voltage constant regardless of the magnitude and direction of the rotor power. The grid-side converter works at the grid frequency (with a controllable leading or lagging power factor in order to absorb or generate reactive power). A transformer is often connected between the grid-side inverter or the stator, and the grid. The rotor-side converter changes its output frequency, depending on the wind speed.

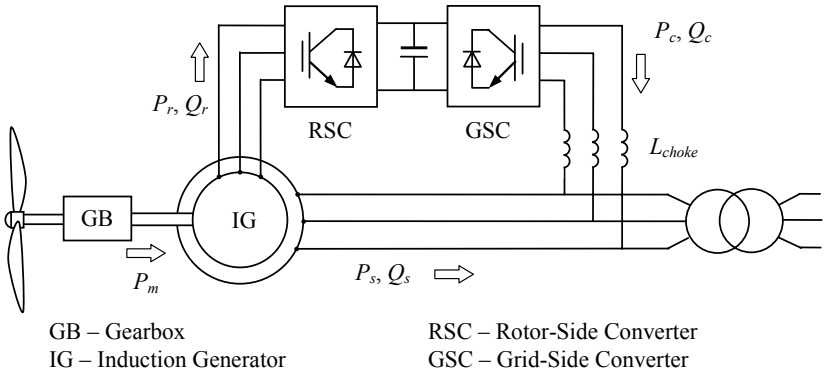

Figure 1.1: Doubly-fed induction generator system and its power flows.

The back-to-back arrangement of the converters provides a mechanism of converting the variable-voltage, variable-frequency output of the generator rotor winding (as its speed changes) into a fixed-frequency, fixed-voltage output compliant with the grid. The DC-link capacitance is an energy storage element that provides an energy buffer between the generator and the grid.

The power electronic converters need only be rated to handle the rotor power which is a fraction of the total power, typically about 30% nominal generator power. Therefore, the losses in the power electronic converter can be reduced, compared to a system where the converter has to handle the nominal generator power, and the system cost is lower due to the partially rated power electronics.

At the current state of development, most DFIG power electronics utilise two-level six-switch voltage-source conversion technology. The switching elements in these power

converters are likely to be insulated-gate bipolar transistors (IGBTs). The six-switch converter can synthesise a three-phase output voltage which can be of arbitrary magnitude, frequency and phase, within the constraint that the peak line voltage is less than the DC-link voltage. The converter is capable of changing the output voltage almost instantaneously – the limit is related to the switching frequency of the pulse-width modulated switching devices, and delays introduced by any filtering on the output.

2) Power Flow

In steady-state at fixed turbine speed with a lossless DFIG system, the mechanical power from the aerodynamic system is balanced by the DFIG power, in Figure 1.1, $P_m = P_s + P_r$. It follows that

$$P_r = P_m - P_s = T_m\omega_r - T_m\omega_s = -T_m\left(\frac{\omega_s - \omega_r}{\omega_s}\right)\omega_s = -sT_m\omega_s = -sP_s \tag{1.1}$$

where s is defined as the slip of the generator: $s = \dfrac{\omega_s - \omega_r}{\omega_s}$.

Therefore if the maximum slip is limited, say to 0.3, the rotor winding converters can be rated as a fraction of the induction generator rated power. This is typically around ±30% for DFIG in wind power generation systems and gives a slip range of ±0.3. From the above relationships, the stator and rotor power are $P_s = P_m/(1–s)$ and $P_r = –sP_m/(1–s)$, respectively. To assess the change in mechanical power during different rotor speeds, the following analysis is carried out with all terms in per unit values. The slip is assumed to vary from a sub-synchronous value of +0.35 to a super-synchronous value of –0.35.

The per unit output power from wind turbine is

$$P_m = C_{p\_pu}V_{wind\_pu}^3 \tag{1.2}$$

Here we use the example wind turbine model in MATLAB (The Mathworks Inc., 2008) [1.24]: $C_p(\lambda,\beta) = c_1\left(\dfrac{c_2}{\lambda_i} - c_3\beta - c_4\right)e^{\frac{-c_5}{\lambda_i}} + c_6\lambda$, $\dfrac{1}{\lambda_i} = \dfrac{1}{\lambda + 0.08\beta} - \dfrac{0.035}{\beta^3 + 1}$,

with the coefficients as $c_1 = 0.5176$, $c_2 = 116$, $c_3 = 0.4$, $c_4 = 5$, $c_5 = 21$ and $c_6 = 0.0068$.

$\lambda = \dfrac{\omega_r R}{V_{wind}}$ is the tip-speed ratio. The maximum value of C_p is 0.48 when $\beta = 0$ and $\lambda = 8.1$. These are defined as base values for per unit calculations. Here base wind speed is 12 ms^{-1}, the gear ratio is 10, rotor radius is 5.16m.

When $s = -0.2$, C_p is 0.48 then P_m is 1.0 p.u. ideally. Hence for 2 pole-pair generator,

$$s = \frac{\omega_s - \omega_r}{\omega_s},\quad \omega_{r\_pu} = 1 - s,\quad \lambda = \frac{\omega_r R}{V_{wind}} = (1-s)\frac{5\pi \times 5.16}{12} = 6.751(1-s) = c_7(1-s).$$

Then at the base wind speed, the expression of P_m in terms of slip s is

$$P_m = \frac{C_p}{0.48} = \frac{1}{0.48}\left[c_1\left(\frac{c_2}{\lambda_i} - c_4\right)e^{\frac{-c_5}{\lambda_i}} + c_6 c_7(1-s)\right],\quad \frac{1}{\lambda_i} = \frac{1}{c_7(1-s)} - 0.035. \quad (1.3)$$

The above analysis is performed in MATLAB programming to assess power flow. This turbine model will be used throughout the thesis. Figure 1.2 shows how the rotor and stator power vary as the rotor slip changes from sub- to super-synchronous modes. The speed of the rotor has to change as wind speed changes in order to track the maximum power point of the aerodynamic system given by the optimum tip-speed ratio. Slip, s, therefore is related to incident wind speed. In this case, a slip of –0.2 occurs with rated wind speed (12 ms^{-1}). As wind speed drops, slip has to increase and in this case has a maximum value of 0.35.

It is clear that the mechanical power, P_m, reaches its peak at super-synchronous speed when $s = -0.2$. When rotating at the synchronous speed ($s = 0$), the DFIG supplies all the power via the stator winding, with no active power flow in the rotor windings and their associated converters. Note that at $s = 0$, the stator power is at maximum. As the wind speed increases, the rotational speed must also increase to maintain optimum tip-speed ratios. In such circumstances, the machine operates at super-synchronous speeds ($s < 0$). The mechanical power flows to the grid through both the stator windings and the rotor windings and their converter. At lower wind speeds, the blades rotate at a sub-synchronous speed ($s > 0$). In such circumstances, the rotor converter system will absorb power from the grid connection to provide excitation

for the rotor winding. With such a scheme it is possible to control the power extracted from the aerodynamic system such that the blade operates at the optimum aerodynamic efficiency (thereby extracting as much energy as possible) by adjusting the speed of rotation according to the incident wind speed.

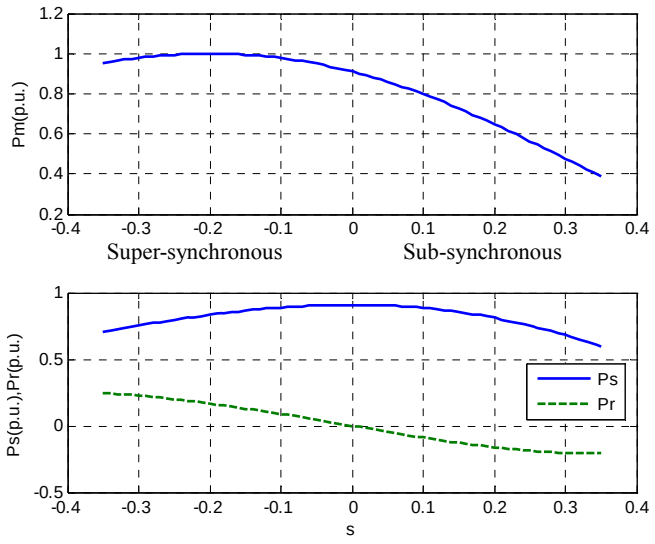

Figure 1.2: DFIG mechanical power, generator stator power and rotor power in per unit (P_m, P_s, and P_r) in respect to rotor slip s.

3) Rotor-Side Converter

The rotor-side converter applies the voltage to the rotor windings of the induction generator for excitation. The purpose of the rotor-side converter is to control the rotor currents such that the rotor flux position is optimally oriented with respect to the stator flux in order that the desired torque is developed at the shaft of the machine. The vector control for the generator can be embedded in an optimal power tracking controller for maximum energy capture in a wind power application [1.8]. By controlling the active power of the converter, it is possible to vary the rotational speed of the generator, and thus the speed of the shaft of the wind turbine. This can then be used to track the optimum tip-speed ratio as the incident wind speed changes thereby extracting the maximum power.

The rotor-side converter uses a torque controller to regulate the wind turbine output power measured at the machine stator terminals. The power is controlled in order to

follow a pre-defined turbine power-speed characteristic to track the maximum power point. The actual electrical output power from the generator terminals, added to the total power losses (mechanical and electrical) is compared with the reference power obtained from the wind turbine characteristic.

The control scheme of the rotor-side converter is organised in a generic way with two series of Proportional-Integral (PI) controllers. The reference *q*-axis rotor current i_{rq}^{ref} can be obtained either from an outer speed-control loop or from a reference torque. These two options may be termed a speed-control mode or torque-control mode for the generator, instead of regulating the active power directly. Another PI controller is included to produce a reference signal for the *d*-axis rotor current component – i_{rd}^{ref} – to control the reactive power required from the generator.

The reference rotor current i_{rq}^{ref} is forced in the rotor winding by the rotor-side converter. The actual i_{rq} component of rotor current is compared with i_{rq}^{ref} and the error is reduced to zero by a PI controller with the inner control loop. The output of this current controller is the voltage v_{rq} generated by the rotor-side converter. With another similarly regulated i_{rd} and v_{rd} component the required 3-phase voltages applied to the rotor winding are obtained and force the i_{rd} and i_{rq} towards their reference values.

In other words, the rotor-side converter provides a varying-frequency excitation depending on the wind speed conditions. The induction generator is controlled in a synchronously rotating *dq*-axis frame, with the *d*-axis oriented along the stator-flux vector position in one common implementation. This is called stator-flux orientation (SFO) vector control. Consequently, the active power and reactive power are controlled independently from each other. Orientation frames applied in traditional vector control of induction generators such as rotor-flux orientation and magnetising-flux orientation, can also be utilised [1.25]. Additionally, the stator-voltage orientation (SVO) is also commonly used in DFIG vector controllers [1.9].

4) Grid-Side Converter

The grid-side converter aims to regulate the voltage of the DC-link capacitor. Moreover, it can generate or absorb reactive power for voltage support. The converter is also current regulated, with the *d*-axis current used to regulate the DC-link voltage and the *q*-axis current component to regulate the reactive power. The vector-control method uses a reference frame oriented along the stator voltage vector position, enabling independent control of the active and reactive power flowing between the grid and the converter. Therefore, the grid-side converter control has the potential for optimising the grid integration with respect to steady-state operation conditions, power quality and voltage stability.

The function is realised with two control loops as well. An outer regulation loop consists of a DC voltage regulator. The output of the DC voltage regulator is a reference current i_{cd}^{ref} for the current regulator. The inner current regulation loop consists of a current regulator controlling the magnitude and phase of the voltage generated by converter from the i_{cd}^{ref} produced by the DC voltage regulator and specified *q*-axis reference i_{cq}^{ref}, which is used to control power factor.

5) DFIG Fault-Ride Through

Recently, research about DFIG systems focuses on its fault-ride through capability during AC-side disturbances. The motivation for this is the grid codes which are now requiring fault-ride through capability for renewable power integration. Appropriate modelling of DFIG systems are analysed for different purposes such as for power system stability analysis [1.26]-[1.28]. For grid integration, under AC-side voltage dip conditions, the DFIG fault-ride through analysis is described in [1.29]-[1.33]. New fault tolerant DFIG topologies and control methods are proposed for the systems [1.34]-[1.36]. More detailed analysis of DFIG fault conditions and converter protection methods will be summarised in Chapter 2, with a new protection scheme being proposed.

1.3.2 Permanent Magnet Synchronous Generators

The DFIG systems utilise a gearbox that couples the wind turbine to the generator. The gearbox suffers from faults and requires regular maintenance. The reliability of the variable-speed wind turbine system can be improved significantly by using a direct-driven PMSG – eliminating the gearbox. With the development of high energy magnet materials, the PMSG has received much attention in wind energy applications because of their self-excitation. The use of permanent magnets in the rotor of the PMSG makes it unnecessary to supply magnetising current. Hence, because of the absence of the magnetising current PMSG solutions are often more efficient than other machines. To extract maximum power from the fluctuating wind, variable-speed operation of the wind-turbine PMSG is necessary. Two power electronic topologies are proposed for variable-speed operation of PMSG. They require different control strategies for the generator. PMSGs are also being used in wind turbines with gearboxes, for example, Doosan Heavy Industries.

1) Large-Scale PMSG System

For this system, control strategies use wind velocity to determine the optimum shaft speed, hence, the generator speed. For a general system, an anemometer-based control strategy increases cost and may even reduce the reliability of the overall system. However, for large wind turbines, the anemometer represents only a very small fraction of the total cost and the control strategy based on wind velocity to determine optimum generator speed is adopted. In [1.11], [1.12], the current vector of an interior-type PMSG is controlled to optimise the wind-turbine operation at various wind speed, which requires six active switches to be controlled, Figure 1.3.

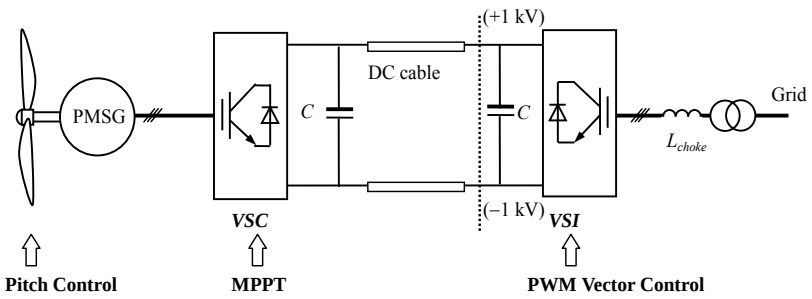

Figure 1.3: Large-scale PMSG power conversion system topology.

2) Small-Scale PMSG System

A control strategy for the generator-side converter (DC/DC boost converter) with output maximisation of a PMSG small-scale wind turbine was developed in [1.13], Figure 1.4. The generator-side switch-mode rectifier (a diode rectifier and boost converter) is controlled to achieve maximum power from the wind. The method requires only one active switching device (IGBT), which is used to control the generator torque to extract maximum power. It is simple and a low-cost solution for a small-scale wind turbine.

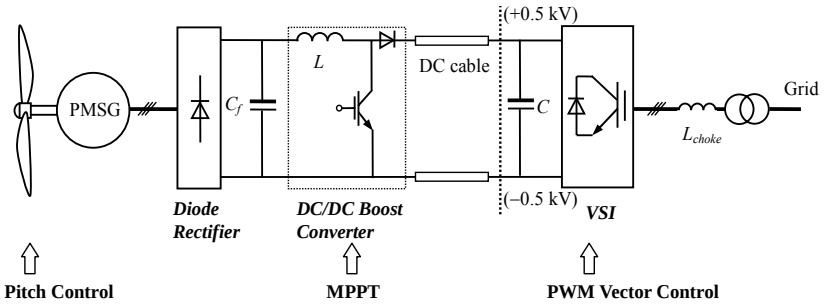

Figure 1.4: Small-scale PMSG power conversion system topology.

For a stand-alone system, the output voltage of the load side voltage-source inverter (VSI) has to be controlled in terms of amplitude and frequency. Previous publications related to PMSG-based variable-speed wind turbine mostly concentrate on grid connected systems [1.37]-[1.39]. However, remote area local small-scale stand-alone distributed generation system can utilise available renewable energy resources when grid connection is not feasible. In [1.13], a control strategy is developed to control the load voltage in a stand-alone mode. As there is no grid in a stand-alone system, the amplitude and frequency of the output voltage has to be controlled. The load-side pulse-width modulated (PWM) inverter uses a vector-control scheme to control the amplitude and frequency of the output voltage. The stand-alone control is featured with output voltage and frequency controller capable of handling variable load conditions. Grid fault analysis of the PMSG system performance is discussed in [1.40], [1.41]. However, these are in terms of the grid disturbance conditions. Chapter 3 will deal with the possible internal DC fault conditions of this wind power generation system.

1.4 Wind Power Collection and Transmission Technologies

Traditional alternating-current (AC) transmission and distribution systems are used for integration of power generation and for long-distance power transmission and distribution to power customers. There has been decades of operational experience and it is mature in system operation and protection. However, since the increasing integration of renewable power, there has been renewed interest in direct-current (DC) transmission for offshore wind farm power collection and transmission, both technically and economically [1.16]-[1.18]. For long-distance transmission and offshore environments, DC transmission is more economic and may offer additional technical benefits.

1.4.1 Collection Grid

Conventional offshore wind farms use AC systems. The wind farm "electrical system" describes the electrical equipment and devices, including transformers, cables/lines linking wind turbines and from them to platforms, and connecting cables/lines from platforms to the shore. Offshore substation platforms may be required in some cases for the transformers. In [1.42], the electrical system is defined as: "basically all equipment required to deliver and control the electrical energy that follows from the generator to the grid."

For AC systems, the offshore linking cables and transformers are called collection grids [1.43]-[1.45], or collector/collection systems [1.46], [1.47]. The collection grids are always of a medium voltage (MV). While the transmission line to the grid are of high voltage (HV) to improve transmission efficiency. Until now, there have been many discussions about the transmission choices such as traditional high-voltage alternative current (HVAC), conventional high-voltage direct current (HVDC), and voltage-source converter based HVDC. This will influence the topology of the collection grid due to different power conversion requirements. More detailed collection grid topologies will be studied in Chapter 6 for redundancy analysis.

1.4.2 High-Voltage Direct-Current Transmission

The history of electric power systems began with DC transmission (1882, Thomas Edison). However, it was quickly replaced by three-phase AC transmission because of several advantages of the latter. The most distinct advantage of AC transmission is that power can be transformed to different voltage level using transformers, which allows efficient long-distance power transmission. In addition, circuit breakers for alternating current can take advantage of the natural current zeros that occur twice per cycle, and AC motors are cheaper and more robust than DC motors.

In spite of the prevailing use of AC transmission in power systems, interest in DC transmission still remained. In 1954, the first commercial HVDC link between mainland Sweden to Gotland island was commissioned. Since then, the installed power of HVDC transmission systems worldwide has increased steadily, and recently a dramatic increase in capacity has been initiated. Given the extra costs and losses related to the converter stations, HVDC transmission is justified by some conditions where the DC technology is the most appropriate or may be the only solution:

Underground Cable Power Transmission: Due to their physical structures, cables have much higher capacitance than overhead lines. The capacitive current in cables created by the alternating voltage makes AC power transmission over long-distance cables inefficient [1.14]. If the power is transmitted by direct currents, there will be no losses related to capacitive currents. Moreover, to transmit the same amount of power, DC transmission needs fewer power lines than AC transmission. Accordingly, the costs and losses of the converter stations are balanced by savings on the overhead lines/cables where the break-even distance is around several hundred kilometres depending on the project specifications.

Unsynchronised AC-System Connection: AC transmission is only possible if the two interconnected AC systems operate synchronously. DC transmission does not have such requirements and can be used to interconnect asynchronous systems. Many back-to-back HVDC links have been built for such purposes [1.14], [1.15].

Power System Stability Improvement: One of the major features of the HVDC technology is its capability to manipulate power flows in a very short time, which can be utilised to improve the stability of the AC system [1.48].

Firewall Function: Large interconnected AC systems have many advantages, such as the possibility to use larger and more economical power plants, reduction of reserve capacity in the systems, utilisation of the most efficient energy resources, and achieving an improved system reliability. However, larger interconnected AC systems also increase the system complexity from the operational point of view. One of the consequences of such complexity is the large blackouts in America and Europe [1.48]. In this aspect, HVDC links have a "firewall" function in preventing cascaded AC system outages.

1) HVDC Transmission Using Line-Commutated Current-Source Converters

Line-commutated converters based on thyristor are called current-source converters (CSCs) [1.14]. The CSC can be used for transmitting power in two directions, i.e., the rectifier mode and the inverter mode. This is achieved by applying different firing angles on the valves (theoretically 0°–90° for rectifier; 90°–180° for inverter). An HVDC link is essentially constructed using two converters, which are interconnected on the DC sides. The interconnection could be overhead lines, underground cables, or a back-to-back connection. The application of CSC-HVDC technology has been very successful. However, the CSC technology suffers from several inherent weaknesses:

Consumption of Reactive Power: One problem is that the CSC always consumes reactive power, either in rectifier mode or in inverter mode. Depending on the firing angles, the reactive power consumption of a CSC-HVDC converter station is approximately 50–60 % of the active power [1.48]. The reactive-power consumption requires compensation by connecting large AC capacitors at the converter stations. For a common CSC-HVDC link, the capacitors not only increase the costs, but also occupy large amounts of space volume of the converter station. Besides, large capacitors also contribute to the transient overvoltage and low-order harmonic resonance problems of the HVDC link when connects to a weak AC system.

Commutation Failures: Another problem of the CSC-HVDC system is the occurrence of commutation failures at the inverter station typically caused by disturbances in the AC system [1.14]. The commutation failure creates a short circuit on the DC side, which temporarily stops the power transmission. Commutation failures are less common phenomena than in the early schemes owing to the vastly improved solid state valve technology that exist nowadays.

Weak AC-System Connection: This problem can become a limiting factor for CSC-HVDC applications. For CSCs, the successful commutation of the alternating current from one valve to the next relies on the stiffness of the alternating voltage, i.e., the network strength of the AC system [1.48]. If the AC system has low short-circuit capacity relative to the power rating of the HVDC link, i.e., low short-circuit ratio (SCR), more problematic interactions between the AC and the DC systems are expected. Besides, the SCR of the AC system also imposes an upper limitation on the HVDC power transmission.

2) HVDC Transmission Using Force-Commutated Voltage-Source Converters

The voltage-source converter (VSC) is a relatively new converter technology for HVDC transmission. The first commercial VSC-HVDC (HVDC-Light) link with a rating of 50 MW was commissioned in 1999 at Gotland Island, Sweden, close to the world's first CSC-HVDC link [1.17]. Voltage-source converters utilise self-commutating switches, gate turn-off thyristors (GTOs) or insulated-gate bipolar transistors (IGBTs), which can be actively turned-on and -off. Therefore, a VSC can produce its own sinusoidal voltage waveform using pulse-width modulation (PWM) technology independent of the AC system. Many different topologies have been proposed for VSCs. For HVDC applications, three major types are favoured: the two-level converter, the multi-level converter, and the modular multi-level converter.

The two-level bridge is the simplest topology to construct a three-phase force-commutated VSC. The bridge consists of six switches with associated anti-parallel diodes. For an HVDC link, two VSCs are interconnected on the DC sides. For high-voltage applications, series connection of switching devices is

necessary. The operation principle of the two-level bridge is simple. Each phase of the VSC can be connected either to the positive DC terminal, or the negative DC terminal. By adjusting the width of pulses, the output voltage can be produced to interface with the grid voltage after filtering by phase reactors and shunt filters.

Multi-level VSCs are promising for medium- and high-power conversion applications [1.49]-[1.51]. There are two common multi-level converters: three-level neutral-point-clamped (3L-NPC) converter and five-level flying capacitor (5L-FC) converter. The key components that distinguish the 3L-NPC topology from the two-level converter are the two clamping diodes in each phase. These two diodes clamp the switch voltage to half of the DC-link voltage. Thus, each phase of the VSC can switch to three different voltage levels, i.e., the positive DC terminal, the negative DC terminal and zero volts (the mid-point). Consequently, voltage pulses produced by a multi-level VSC are a closer match to the reference voltage. Therefore, the multi-level converter has less harmonic content. Additionally, they have lower switching losses. Compared to two-level VSCs, 3L-NPC VSCs require more diodes for neutral-point clamping. However, the total number of switching components does not necessarily have to be higher [1.48]. The NPC concept can be extended to higher number of voltage levels, which can result in further improved harmonic reduction and lower switching losses. However, for high-voltage converter applications, the neutral-clamped diodes complicate the insulation and cooling design of the converter switches [1.48].

The recently proposed modular multi-level converter (MMC) concept has attracted interest [1.50]. Compared to the above two topologies, one major feature of the MMC is that no common capacitor is connected at the DC side. The DC capacitors are distributed into each module, while the converter is built up by cascade-connected modules. The MMC concept is especially attractive for high-voltage applications, since the converter can be easily scaled up by inserting additional modules in each arm. If considerable numbers of modules are cascaded (approximately 100 modules would be typical for HVDC applications), each module theoretically only need to switch on and off once per period, which greatly reduces the switching losses. With only five modules, the waveform already resembles much better the sinusoidal voltage reference than the other two topologies. With MMC, the harmonic content of the voltage

produced by the VSC is so low that additional filtering equipment is almost unnecessary. An additional benefit of the MMC is that the control system has an extra freedom in dealing with faults at the DC side. The DC capacitors are not necessarily discharged during faults. Thus, the fault recovery can be faster.

Compared to the other two topologies, the major drawback of the MMC topology is that the required switching components are doubled since only one of the switches of each module contributes to the phase voltage. In addition, the design and control of the MMC are generally more complex than the two-level converter. On the other hand, the reduction of switching losses and savings on filtering equipment of the MMC may eventually justify its application for HVDC transmission.

The VSC can generally be treated as an ideal voltage source where the control system has the freedom to specify the magnitude, phase, and frequency of the voltage waveform. However, for control design and stability analysis, it is important to take into account the limitation of the converter in terms of active and reactive power transfer capability. One such limit is the converter current limitation, which is imposed by the current carrying capability of the VSC switches since both the active power and the reactive power contribute to the current flowing through the switches. Accordingly, if the converter is intended to support the AC system with reactive power supply or consumption, the maximum active power has to be limited to make sure that the switch current is within the limit.

Another limitation which determines the reactive-power capability of the VSC is the maximum and minimum voltage magnitudes that the VSC can produce (modulation index limitation). The overvoltage limitation is imposed by the DC-link voltage of the VSC. The under-voltage limit, however, is limited by the main-circuit design and the active power transfer capability, which requires a minimum voltage magnitude to transmit the active power.

VSC-HVDC technology overcomes most of the weakness of the CSC-HVDC technology. In addition, it supports the AC system with reactive power. Similar to a CSC-HVDC system, a VSC-HVDC system can quickly run up or run back the active power for AC system emergency power support.

Besides the above features, the most essential one is that a VSC-HVDC system has an advantageous connection capability with AC systems, i.e., with properly designed control systems, VSC-HVDC system has the potential to be connected to any kind of AC system with any number of links [1.52], [1.53]. This outstanding feature will eventually bring the DC transmission technology to ever broader application fields. Multi-terminal VSC-HVDC connection applications for wind power integration are gaining more research effort [1.18], [1.54]-[1.57]. With multi-terminal connections to different onshore grids, the integration of large-scale offshore wind farms and possible multiple weak AC system connections are possible. This is also the application background of the work reported in Chapter 4 and 5.

1.5 Protection Development of DC Systems

Fault vulnerability is one of the most significant issues that constrain the development of voltage-source converter based DC networks, especially in high-power scenarios. In addition, this is due to the lack of mature commercial DC switchgear products. However, as introduced above, VSC-HVDC power transmission provides greater operational flexibility which suits renewable energy sources. One typical application is for large-scale offshore wind farm integration to utility grids [1.16], [1.18], [1.58], [1.59] where a reliable DC network is a prerequisite.

In such systems, cable faults do occur more frequently compared with other parts of the system. The most common reason for cable fault is insulation deterioration and breakdown. There can be several causes [1.60]: physical damage (the most serious short-circuit fault can occur because of this); environmental stresses such as damp, especially at the junctions of cables, where the cabling system is exposed to soil or water; electrical stresses due to overload operation or operation at high temperature; and cable aging. These factors can all lead to a ground fault. There has been limited discussion about the influence of DC faults on DC networks at transmission and distribution levels. The following aspects regarding DC system fault analysis have been reported:

1) Line-Commutated, Current-Source Converter HVDC Systems

Conventional line-commutated CSC-based HVDC transmission systems are robust to DC fault overcurrents because of their current-regulated nature [1.61]. DC voltage change is used for fault detection. Since the application of line-commutated CSC-HVDC systems, the overvoltage phenomenon of this current-regulated DC system has been discussed [1.62]-[1.64]. Recently, HVDC protection research has been focused on specific cable fault location approaches. Protection coordination is seldom studied because of the lack of development in multi-terminal DC networks.

2) Cable Fault Location Techniques

At the current stage, cable fault location research is focused on offline techniques [1.65]-[1.69]. Techniques widely used in industry are commonly time-consuming trace methods using acoustic or electromagnetic approaches [1.65]. Travelling wave based methods have also been researched using different algorithms [1.66]-[1.69]. They utilise a travelling wave model of the cable for overvoltage transient analysis and location. A high-frequency pulse wave is injected into the faulty cable and the fault location is found by the comparison between the original and reflected waves. However, when the system structure is complex (e.g. meshed for multi-terminal connection) the DC bus will experience multiple reflections which will influence location results. A detailed cable model is required for accurate fault location using the transient response to a high-frequency pulse. For AC network and line-commutated CSC-HVDC, these offline methods are adequate because fast fault location may not be critical. However, for VSC-based HVDC systems, a fast and accurate fault location is required for effective operation of protective devices [1.70].

3) VSC under AC-Side Faults

VSCs are widely used as rectifiers or inverters for electrical power conversion. If each conversion element of a DC wind farm is a VSC, the VSC control can cope with grid-side AC disturbances, during which appropriate control and protection methods can be used to protect its power electronic devices [1.71], [1.72]. The short circuit current contribution of VSC-HVDC systems for AC system faults are also

analysed in respect of AC system protection. It is shown that the VSC-HVDC system may contribute short-circuit current determined by the SCR [1.73].

4) VSC Internal Faults

In terms of fault-tolerant VSCs, the research aims are to protect the system from possible IGBT faults (e.g. short-circuits) where there are many opportunities to allocate backup function or include redundant devices [1.74]-[1.77].

In terms of DC network faults, with parallel connected VSCs, severe overcurrents due to discharge of the DC-link capacitances are a major issue: the converters' power electronic devices, particularly the freewheel diodes, are subject to overcurrent with DC-side faults on cables or buses. The overcurrents eventually flow through the freewheel diodes in the basic converter configuration and the converter is defenceless against such DC-side faults, such as a DC-link short-circuit, DC cable short-circuits and DC cable ground faults. These fault conditions need to be analysed and simulated in detail for effective system protection prior to the development of practical high-power VSC-HVDC networks. Relevant works are now summarised:

VSC-Based DC Distribution Systems: For DC distribution networks with VSCs, the following research has been reported: 1) fault simulation of a DC micro-grid and switchgear/fuse allocation [1.78]; 2) fault analysis of a VSC-based DC distribution system for a shipboard application [1.79], [1.80] – by replacing diodes with controllable gate power electronic devices to provide bi-directional current blocking function; 3) dedicated discharge overcurrent protection for DC-link capacitors [1.80], [1.81]. However, these studies are for low-power DC distribution systems and cannot be applied to high-power transmission systems.

VSC-HVDC Systems: Fault detection and location for meshed VSC-HVDC systems is discussed in [1.82], [1.83] at the transmission level. The technique in [1.84] extracts the fault signature by comparing initial current change, the current rise time interval, or current oscillation pattern at different switch locations. Based on this technique, [1.83] proposes a fault location and isolation method. This is mainly based on AC-side circuit breakers, and no DC switchgear configuration is discussed due to cost considerations. VSC-HVDC DC cable overvoltage protection under

line-to-ground faults is analysed in [1.84]. However, the protection scheme is not designed specifically for overcurrents flowing through power electronic devices, which are the most vulnerable devices of the system.

Most of the research reported on DC fault analysis with VSC configurations are based on numerical simulations without a theoretical basis through circuit analysis. There is no detailed analysis of the overcurrent during the fault. Moreover, the speed requirement for DC circuit breakers can only be configured after identifying critical time limits under various fault conditions. AC-side switchgear is not considered fast enough to cope with the rapid rise of fault current characteristic of freewheel diode conduction which can damage power electronic devices in several milliseconds.

In addition, most work focuses on the DC short-circuit faults at the DC rails [1.80]. However, fault analysis in VSC-based DC networks and DC cable faults is seldom reported, but a cable short-circuit fault is potentially more common than a DC rail fault and the impact of a DC cable fault on the freewheel diodes in the VSC can be worse than that of a direct DC rail short circuit due to the inductive component in the discharge path. This problem will be discussed in Chapter 4. Although underground cables are seldom short-circuited in comparison to overhead lines, it is a critical condition and needs to be analysed particularly for switchgear relay and protection design. In contrast, ground faults are more common but less serious. However, accurate fault location for effective protection coordination is required for high-impedance ground faults – this is also addressed in Chapter 4. This protection coordination will be designed for a large-scale meshed wind farm system in Chapter 5. In terms of wind farm topology redundancy, the analysis in Chapter 6 aims at enhancing reliability whilst considering economic costs.

1.6 Outline of Thesis

This thesis is presented in the following chapters:

Chapter 2 – The protection schemes for the DFIG system are introduced. A novel protection circuit based on series dynamic resistors for the rotor-side converter is proposed after detailed analysis of the rotor overcurrent under various fault

conditions. This protection scheme is advantageous particularly for asymmetrical AC-side fault conditions. During such faults, the traditional crowbar protection circuit results in reactive power absorption that deteriorates the grid voltage recovery. The proposed protection system can shorten the time of crowbar operation to minimise reactive power consumption.

Chapter 3 – The PMSG-based wind power generation system protection is presented in this chapter. For large-scale systems, a voltage-source converter rectifier is included; for small-scale systems, a boost circuit is used. Protection circuits for these topologies are studied with simulation results for different fault conditions. These electrical protection methods are all in terms of dumping redundant energy resulting from disrupted path of power delivery. Pitch control of large-scale wind turbines are considered for effectively reducing rotor shaft overspeed.

Chapter 4 – A radial VSC-based DC network for wind farm connection is presented in this chapter. Detailed analysis of this DC system is performed under both short-circuit and ground fault conditions. The critical stages of the progress of the fault are defined for this nonlinear system and these are used to coordinate the protection. Simulation results are used to assess a relay coordination methodology for this system. A ground fault location method is presented and tested under different ground resistances, distances, and operating conditions.

Chapter 5 – Large-scale wind farm collection and transmission systems may potentially utilise a meshed connection to enhance reliability. However, for voltage-source converter based HVDC systems, a meshed network leads to a complex protection coordination strategy. With allocation of economical uni-directional power electronic DC circuit breakers, this chapter presents a protection methodology for this large-scale system. DC bus faults are dealt with in particular due to the complex multi-terminal topology of this large-scale DC system.

Chapter 6 – Redundancy analysis for the wind farm collection and transmission systems is carried out based on economic statistics of an existing UK wind farm project. Equipment investment and economic operational losses are compared resulting in a balance between the technical performance and economic investment.

A redundancy design method is proposed to achieve an optimal degree of redundancy using reliability economic loss statistics.

Chapter 7 – A summary of the key research outcomes and contributions of the thesis is provided along with conclusions of the work and suggestions for future research.

1.7 List of Publications

This thesis has resulted in the following publications:

A. Refereed Journal Papers

[J1] ***J. Yang**, J. E. Fletcher, and J. O'Reilly,* "Short-circuit and ground fault analysis and location in VSC-based DC network cables," IEEE Transactions on Industrial Electronics, invitation from the 2010 ISIE conference for special section publication, submitted, Dec. 2010.

[J2] ***J. Yang**, J. E. Fletcher, and J. O'Reilly,* "Protection of meshed VSC-HVDC transmission systems for large-scale wind farms," IET Renewable Power Generation, submitted, Dec. 2010.

[J3] ***J. Yang**, J. E. Fletcher, and J. O'Reilly,* "Multi-terminal DC wind farm collection grid internal fault analysis and protection design," IEEE Transactions on Power Delivery, vol. 25, no. 4, pp. 2308-2318, Oct. 2010.

[J4] ***J. Yang**, J. E. Fletcher, and J. O'Reilly,* "A series-dynamic-resistor-based converter protection scheme for doubly-fed induction generator during various fault conditions," IEEE Transactions on Energy Conversion, vol. 25, no. 2, pp. 422-432, Jun. 2010.

[J5] ***J. Yang**, J. O'Reilly, and J. E. Fletcher,* "Reliability enhancement of offshore wind farms by redundancy analysis," Journal of Automation of Electric Power Systems, vol. 34, no. 4, pp. 84-91, Feb. 2010.

B. Book Chapter

[B1] *J. E. Fletcher and* ***J. Yang**,* "Introduction to doubly-fed induction generator for wind power applications," *Sustainable Energy*, 978-953-7619-X-X, Oct. 2010.

C. Refereed Conference Papers

[C1] ***J. Yang**, J. E. Fletcher, and J. O'Reilly,* "An overview on DC cable modelling for fault analysis of VSC-HVDC transmission systems," Australasian Universities

Power Engineering Conference, AUPEC 2010, Christchurch, New Zealand, 5-8 Dec. 2010.

[C2] ***J. Yang**, J. E. Fletcher, and J. O'Reilly,* "Protection scheme design for meshed VSC-HVDC transmission systems for large-scale wind farms," the 9th International Conference on AC and DC Power Transmission, IET ACDC 2010, London, UK, 20-21 Oct. 2010.

[C3] ***J. Yang**, J. E. Fletcher, and J. O'Reilly,* "Multi-terminal DC wind farm collection grid internal fault analysis," IEEE International Symposium on Industrial Electronics ISIE 2010, Bari, Italy, 4-7 Jul. 2010.

[C4] ***J. Yang**, Y. Gao, and J. O'Reilly,* "Permanent magnet synchronous generator converter protection analysis during DC wind farm open-circuit fault condition," The 9th IEEE Annual Electrical Power and Energy Conference 2009, Montreal, Quebec, Canada, 22-23 Oct. 2009.

[C5] ***J. Yang**, J. E. Fletcher, and J. O'Reilly,* "A series dynamic resistor based converter protection scheme for doubly-fed induction generator during various fault conditions," IEEE Power & Energy Society General Meeting 2009, Calgary, Alberta, Canada, 26-30 Jul. 2009.

[C6] ***J. Yang**, J. O'Reilly, and J. E. Fletcher,* "Protection scheme switch-timing for doubly-fed induction generator during fault conditions," IEEE PowerTech 2009, Bucharest, Romania, 28 Jun. – 2 Jul. 2009.

[C7] ***J. Yang**, J. O'Reilly, and J. E. Fletcher,* "Redundancy analysis of offshore wind farm collection and transmission systems," The 1st International Conference on SUPERGEN, Nanjing, China, 6-7 Apr. 2009.

[C8] ***J. Yang**, D. G. Dorrell, and J. E. Fletcher,* "Fault ride-through of doubly-fed induction generator with converter protection schemes," IEEE International Conference on Sustainable Energy Technologies, Singapore, 24-27 Nov. 2008.

[C9] ***J. Yang**, D. G. Dorrell, and J. E. Fletcher,* "A new converter protection scheme for doubly-fed induction generators during disturbances," The 34th Annual Conference of the IEEE Industrial Electronics Society, Orlando, Florida, USA, 10-13 Nov. 2008.

D. Non-refereed Conference Papers, Seminar Papers

[N1] ***J. Yang**,* "PSCAD/EMTDC simulations for wind farm transient analysis and protection scheme design," Flux Users Conference, Autrans, France, 21-23 Oct. 2009.

1.8 References

[1.1] British Wind Energy Association. UK Wind Energy Database (UKWED). Available: http://www.bwea.com/ukwed/index.asp, 2010.

[1.2] E. Denny and M. O'Malley, "Wind generation, power system operation, and emissions reduction," *IEEE Trans. Power Syst.*, vol. 21, no. 1, pp. 341-347, Feb. 2006.

[1.3] British Wind Energy Association. Offshore Wind. Available: http://www.bwea.com/offshore/index.html, 2010.

[1.4] The European Wind Energy Association. European Statistics. Available: http://www.ewea.org/index.php?id=1486, 2010.

[1.5] The European Wind Energy Association. Offshore Statistics. Available: http://www.ewea.org/index.php?id=1861, 2010.

[1.6] P. J. Tavner, J. Xiang, and F. Spinato, "Reliability analysis for wind turbines," *Wind Energy*, vol. 10, pp. 1-18, Available: http://onlinelibrary.wiley.com/doi/10.1002/we.204/pdf, 2007.

[1.7] British Wind Energy Association, *Stage 3 Discussion Document – GB Electricity Network Access*. Available: http://www.bwea.com/pdf/pathtopower/Stage3.pdf, Mar. 2006.

[1.8] R. Pena, J. C. Clare, and G. M. Asher, "Doubly fed induction generator using back-to-back PWM converters and its application to variable-speed wind-energy generation," *IEE Proc.-Electr. Power Appl.*, vol. 143, no. 3, pp. 231-241, May 1996.

[1.9] S. Muller, M. Deicke, and R.W. De Doncker, "Doubly fed induction generator systems for wind turbines," *IEEE Ind. Appl. Mag.*, vol., no., pp. 26-33, May/Jun. 2002.

[1.10] Z. Chen, J. M. Guerrero, and F. Blaabjerg, "A review of the state of the art of power electronics for wind turbines," *IEEE Trans. Power Electron.*, vol. 24, no. 8, pp. 1859-1875, Aug. 2009.

[1.11] Z. Chen and E. Spooner, "Grid interface options for variable-speed, permanent-magnet generators," *IEE Proc.-Electr. Power Appl.*, vol. 145, no. 4, pp. 273-283, Jul. 1998.

[1.12] M. Chinchilla, S. Arnaltes, and J. C. Burgos, "Control of permanent magnet generators applied to variable-speed wind-energy systems connected to the grid," *IEEE Trans. Energy Convers.*, vol. 21, no. 1, pp. 130-135, Mar. 2006.

[1.13] M. E. Haque, M. Negnevitsky, and K. M. Muttaqi, "A novel control strategy for a

variable-speed wind turbine with a permanent-magnet synchronous generator," *IEEE Trans. Ind. Appl.*, vol. 46, no. 1, pp. 331-339, Jan./Feb. 2010.

[1.14] J. Arrillaga, *High Voltage Direct Current Transmission, 2nd Edition*. London: The Institution of Electrical Engineers, 1998.

[1.15] M. Bahrman and B. Johnson, "The ABCs of HVDC transmission technologies," *IEEE Power Energy Mag.*, vol. 5, no. 2, pp. 32-44, Mar./Apr. 2007.

[1.16] P. Bresesti, W. L. Kling, R. L. Hendriks, and R. Vailati, "HVDC connection of offshore wind farms to the transmission system," *IEEE Trans. Energy Convers.*, vol. 22, no. 1, pp. 37-43, Mar. 2007.

[1.17] N. Flourentzou, V. G. Agelidis, and G. D. Demetriades, "VSC-based HVDC power transmission systems: an overview," *IEEE Trans. Power Electron.*, vol. 24, no. 3, pp. 592-602, Mar. 2009.

[1.18] D. Jovcic and N. Strachan, "Offshore wind farm with centralised power conversion and DC interconnection," *IET Gener. Transm. & Distrib.*, vol. 3, no. 6, pp. 586-595, Jun. 2009.

[1.19] J. Rodriguez, J.-S. Lai, and F. Z. Peng, "Multilevel inverters: a survey of topologies, controls, and applications," *IEEE Trans. Ind. Electron.*, vol. 49, no. 4, pp. 724-738, Aug. 2002.

[1.20] B. Gemmell, J. Dorn, D. Retzmann, and D. Soerangr, "Prospects of multilevel VSC technologies for power transmission," in *Proc. IEEE/PES T&D Conf. Expo.*, pp. 1-16., Apr. 21-24, 2008.

[1.21] G. P. Adam, O. Anaya-Lara, G. M. Burt, D. Telford, B. W. Williams, and J. R. McDonald, "Modular multilevel inverter: pulse width modulation and capacitor balancing technique," *IET Power Electron.*, vol. 3, no. 5, pp. 702-715, Oct. 2010.

[1.22] S. Kouro, M. Malinowski, K. Gopakumar, J. Pou, L. G. Franquelo, B. Wu, J. Rodriguez, M. A. Perez, and J. I. Leon, "Recent advances and industrial applications of multilevel converters," *IEEE Trans. Ind. Electron.*, vol. 57, no. 8, pp. 2553-2580, Aug. 2010.

[1.23] J. Ribrant and L. M. Bertling, "Survey of failures in wind power systems with focus on Swedish wind power plants during 1997–2005," *IEEE Trans. on Energy Convers.*, vol. 22, no. 1, pp. 167-173, Mar. 2007.

[1.24] The Mathworks Inc., MATLAB (R2008a), Product Help, 2008.

[1.25] P. Vas, *Vector Control of AC Machines*, Oxford University Press, Oxford, UK, 1990.

[1.26] P. Ledesma and J. Usaola, "Doubly fed induction generator model for transient stability analysis," *IEEE Trans. Energy Conver.,* vol. 20, no. 2, pp. 388-397, Jun. 2005.

[1.27] A. Petersson, *Analysis, modeling and control of doubly-fed induction generators for wind turbines*, Ph.D. Thesis, Chalmers University of Technology, Goteborg, Sweden, 2005.

[1.28] I. Erlich, J. Kretschmann, J. Fortmann, S. Mueller-Engelhardt, and H. Wrede, "Modeling of wind turbines based on doubly-fed induction generators for power system stability studies," *IEEE Trans. Power Syst.*, vol. 22, no. 3, pp. 909-919, Aug. 2007.

[1.29] M. S. Vicatos and J. A. Tegopoulos, "Transient state analysis of a doubly-fed induction generator under three phase short circuit," *IEEE Trans. Energy Convers.*, vol. 6, no. 1, pp. 62-68, Mar. 1991.

[1.30] J. Morren, and S.W.H. de Haan, "Ridethrough of wind turbines with doubly-fed induction generator during a voltage dip," *IEEE Trans. Energy Convers.*, vol. 20, no. 2, pp. 435-441, Jun. 2005.

[1.31] J. Morren and S. W. H. de Haan, "Short-circuit current of wind turbines with doubly fed induction generator," *IEEE Trans. Energy Convers.*, vol. 22, no. 1, pp. 174-180, Mar. 2007.

[1.32] J. López, P. Sanchis, X. Roboam, and L. Marroyo, "Dyanmic behavior of the doubly fed induction generator during three-phase voltage dips," *IEEE Trans. Energy Convers.*, vol. 22, no. 3, pp. 709-717, Sep. 2007.

[1.33] J. López, E. Gubía, P. Sanchis, X. Roboam, and L. Marroyo, "Wind turbines based on doubly fed induction generator under asymmetrical voltage dips," *IEEE Trans. Energy Convers.*, vol. 23, no. 1, pp. 321-330, Mar. 2008.

[1.34] D. Xiang, R. Li, P. J. Tavner, and S. Yang, "Control of a doubly fed induction generator in a wind turbine during grid fault ride-through," *IEEE Trans. Energy Convers.*, vol. 21, no. 3, pp. 652-662, Sep. 2006.

[1.35] I. Erlich, H. Wrede, and C. Feltes, "Dynamic behavior of DFIG-based wind turbines during grid faults," in *Proc. Power Convers. Conf.*, Nagoya, Japan, Apr. 2-5, 2007.

[1.36] P. S. Flannery and G. Venkataramanan, "A fault tolerant doubly fed induction generator wind turbine using a parallel grid side rectifier and series grid side converter," *IEEE Trans. Power Electron.*, vol. 23, no. 3, pp. 1126-1135, May 2008.

[1.37] K. Tan and S. Islam, "Optimal control strategies in energy conversion of PMSG wind turbine system without mechanical sensors," *IEEE Trans. Energy Convers.*, vol. 19, no. 2, pp. 392-399, Jun. 2004.

[1.38] S. Morimoto, H. Nakayama, M. Sanada, and Y. Takeda, "Sensorless output maximization control for variable-speed wind generation system using IPMSG," *IEEE Trans. Ind. Appl.*, vol. 41, no. 1, pp. 60-67, Jan. 2005.

[1.39] P. Tenca, A. A. Rockhill, and T. A. Lipo, "Wind turbine current-source converter

providing reactive power control and reduced harmonics," *IEEE Trans. Ind. Appl.*, vol. 43, no. 4, pp. 1050-1060, Jul./Aug. 2007.

[1.40] A. Abedini and A. Nasiri, "PMSG wind turbine performance analysis during short circuit faults," in *Proc. IEEE Canada Electrical Power Conf.*, Montreal, Quebec, Canada, 25-26 Oct. 2007.

[1.41] A. D. Hansen and G. Michalke, "Multi-pole permanent magnet synchronous generator wind turbines' grid support capability in uninterrupted operation during grid faults," *IET Renew. Power Gener.*, vol. 3, no. 3, pp. 333-348, May 2009.

[1.42] J. Ribrant, *Reliability performance and maintenance – a survey of failures in wind power systems*, M.Sc. Thesis. KTH School of Electrical Engineering, Stockholm, Sweden, Apr. 2006.

[1.43] B. Franken, H. Breder, M. Dahlgren, and E. K. Nielsen, "Collection grid topologies for off-shore wind parks," *18th International Conference on Electricity Distribution, CIRED*, Turin, Italy, Jun. 6-9, 2005.

[1.44] A. Sannino, H. Breder, and E. K. Nielsen, "Reliability of collection grids for large offshore wind parks," *9th International Conference on Probabilistic Methods Applied to Power Systems, PMAPS*, KTH, Stockholm, Sweden, Jun. 11-15, 2006.

[1.45] L. Liljestrand, A. Sannino, H. Breder, and S. Thorburn, "Transients in collection grids of large offshore wind parks," *Wind Energy*, Wiley Interscience, Jul. 2007, online http://doi.wiley.com/10.1002/we.233

[1.46] R. A. Walling and T. Ruddy, "Economic optimization of offshore wind farm substations and collection systems," *5th International Workshop on Large-Scale Integration of Wind Power and Transmission Networks for Offshore wind Farms*, Glasgow, UK, Apr. 7-8, 2005.

[1.47] G. Quinonez-Varela, G. W. Ault, O. Anaya-Lara, and J. R. McDonald, "Electrical collector system options for large offshore wind farms," *IET Renew. Power Gener.*, vol. 1, no. 2, pp. 107-114, Jun. 2007.

[1.48] L. Zhang, *Modeling and control of VSC-HVDC Links connected to weak AC systems*, Ph.D. Thesis, Royal Institute of Technology, Stockholm, Sweden, 2010.

[1.49] J. Rodriguez, J.-S. Lai, and F. Z. Peng, "Multilevel inverters: a survey of topologies, controls, and applications," *IEEE Trans. Ind. Electron.*, vol. 49, no. 4, pp. 724-738, Aug. 2002.

[1.50] S. Kouro, M. Malinowski, K. Gopakumar, J. Pou, L. G. Franquelo, B. Wu, J. Rodriguez, M. A. Perez, and J. I. Leon, "Recent advances and industrial applications of multilevel converters," *IEEE Trans. Ind. Electron.*, vol. 57, no. 8, pp. 2553-2580, Aug. 2010.

[1.51] H. Abu-Rub, J. Holtz, J. Rodriguez, and B. Ge, "Medium-voltage multilevel converters – state of the art, challenges, and requirements in industrial

applications," *IEEE Trans. Ind. Electron.*, vol. 57, no. 8, pp. 2581-2596, Aug. 2010.

[1.52] M. Durrant, H. Werner, and K. Abbott, "Model of a VSC HVDC terminal attached to a weak ac system," in *IEEE Conf. Control Appl.*, Istanbul, 2003.

[1.53] L. Zhang, L. Harnefors and H.-P. Nee, "Interconnection of two very weak ac systems by VSC-HVDC links using power-synchronization control", *IEEE Trans. Power Systems*, online early access, 2010.

[1.54] W. Lu and B. T. Ooi, "Multiterminal LVDC system for optimal acquisition of power in wind-farm using induction generators," *IEEE Trans. Power Electron.*, vol. 17, no. 4, pp. 558-563, Jul. 2002.

[1.55] W. Lu and B. T. Ooi, "Optimal acquisition and aggregation of offshore wind power by multiterminal voltage-source HVDC," *IEEE Trans. Power Del.*, vol. 18, no. 1, pp. 201-206, Jan. 2003.

[1.56] G. P. Adam, O. Anaya-Lara, and G. Burt, "Multi-terminal dc transmission system based on modular multilevel converter," in *Proc. 44th Int. Universities Power Eng. Conf.*, Glasgow, UK, Sept. 1-4, 2009.

[1.57] D. Jovcic, and B. T. Ooi, "Developing dc transmission networks using dc transformers," *IEEE Trans. Power Del.*, vol. 25, no. 4, pp. 2535-2543, Oct. 2010.

[1.58] C. Meyer, M. Hoing, A. Peterson, and R.W. De Doncker, "Control and design of DC grids for offshore wind farms," *IEEE Trans. Ind. Appl.*, vol. 43, no. 6, pp. 1475-1482, Nov./Dec. 2007.

[1.59] A. Prasai, J. S. Yim, D. Divan, A. Bendre, and S. K. Sul, "A new architecture for offshore wind farms," *IEEE Trans. Power Electron.*, vol. 23, no. 3, pp. 1198-1204, May 2008.

[1.60] M. J. Mousavi and K. L. Butler-Purry, "A novel condition assessment system for underground distribution applications," *IEEE Trans. Power Sys.*, vol. 24, no. 3, pp. 115-1125, Aug. 2009.

[1.61] P. M. Anderson, *Power system protection*. New York: IEEE Press, 1999.

[1.62] N. G. Hingorani, "Transient overvoltage on a bipolar HVDC overhead line caused by dc line faults," *IEEE Trans. Power Appar. Sys.*, vol. PAS-89, no. 4, pp. 592-610, Apr. 1970.

[1.63] E. W. Kimbark, "Transient overvoltages caused by monopolar ground fault on bipolar dc line: theory and simulation," *IEEE Trans. Power Appar. Sys.*, vol. PAS-89, no. 4, pp. 584-592, Apr. 1970.

[1.64] G. T. Wrate, I. K. Tasinga, S. S. Low, D. J. Melvold, R. S. Thallam, D. W. Gerlach, and J. Y. Chang, "Transient overvoltages on a three terminal dc transmission system due to monopolar ground faults," *IEEE Trans. Power Del.*, vol. 5, no. 2, pp. 1047-1053, Apr. 1990.

[1.65] E. C. Bascom, "Computerized underground cable fault location expertise," in *Proc. IEEE Power Eng. Soc. General Meeting*, pp. 376-382, Apr. 10-15, 1994.

[1.66] X. Liu, A. H. Osman, and O. P. Malik, "Hybrid travelling wave/boundary protection for monopolar HVDC line," *IEEE Trans. Power Del.*, vol. 24, no. 2, pp. 569-578, Apr. 2009.

[1.67] Y.-J. Kwon, S.-H. Kang, D.-G. Lee, and H.-K. Kim, "Fault location algorithm based on cross correlation method for HVDC cable lines," *IET 9th Int. Conf. Developments in Power Syst. Protection*, Glasgow, U.K., 17-20 Mar. 2008.

[1.68] X. Yang, M.-S. Choi, S.-J. Lee, C.-W. Ten, and S.-I. Lim, "Fault location for underground power cable using distributed parameter approach," *IEEE Trans. Power Sys.*, vol. 23, no. 4, pp. 1809-1816, Nov. 2008.

[1.69] M.-S. Choi, S.-J. Lee, D.-S. Lee, and B.-G Jin, "A new fault location algorithm using direct circuit analysis for distribution systems," *IEEE Trans. Power Del.*, vol. 19, no. 1, pp. 35-41, Jan. 2004.

[1.70] J. Yang, J. E. Fletcher, and J. O'Reilly, "Protection scheme design for meshed VSC-HVDC transmission systems for large-scale wind farms," the *9th Int. Conf. on AC and DC Power Transmission, IET ACDC 2010*, London, UK, 20-21 Oct. 2010.

[1.71] L. Xu, B. R. Andersen, and P. Cartwright, "VSC transmission system operating under unbalanced network conditions – analysis and control design", *IEEE Trans. Power Del*, vol. 20, no. 1, pp. 427-434, Jan. 2005.

[1.72] G. Ramtharan, A. Arulampalam, J. B. Ekanayake, F. M. Hughes, and N. Jenkins, "Fault ride through of fully rated converter wind turbines with ac and dc transmission systems," *IET Renew. Power Gener.*, vol. 3, no. 4, pp. 426-438, Aug. 2009.

[1.73] Y. Jiang-Hafner, M. Hyttinen, and B. Paajarvi, "On the short circuit current contribution of HVDC light," *IEEE PES Asia Pacific Trans. Distr. Conf. Exhib.*, vol. 3, pp. 1926-1932, 6-10 Oct. 2001.

[1.74] H. A. Darwish, A.-M. I. Taalab, and M. A. Rahman, "Performance of HVDC converter protection during internal faults," in *Proc. IEEE Power Eng. Society General Meeting*, pp. 57-59, Montreal, Quebec, Canada, 18-22 Jun. 2006.

[1.75] B. Lu and S. K. Sharma, "A literature review of IGBT fault diagnostic and protection methods for power inverters," *IEEE Trans. Ind. Appl.*, vol. 45, no. 5, pp. 1770-1777, Sep./Oct. 2009.

[1.76] F. Wang, R. Lai, X. Yuan, F. Luo, R. Burgos, and D. Boroyevich, "Failure-mode analysis and protection of three-level neutral-point-clamped PWM voltage source converters," *IEEE Trans. Ind. Appl.*, vol. 46, no. 2, pp. 866-874, Mar./Apr. 2010.

[1.77] P. Lezana, J. Pou, T. A. Meynard, J. Rodriguez, S. Ceballos, and F. Richardeau,

"Survey on fault operation on multilevel inverters," *IEEE Trans. Ind. Electron.*, vol. 57, no. 7, pp. 2207-2218, Jul. 2010.

[1.78] D. Salomonsson, L. Soder, and A. Sannino, "Protection of low-voltage dc microgrids," *IEEE Trans. Power Del.*, vol. 24, no. 3, pp. 1045-1053, Jul. 2009.

[1.79] M. E. Baran and N. R. Mahajan, "DC distribution for industrial systems: opportunities and challenges," *IEEE Trans. Ind. Appl.*, vol. 39, no. 6, pp. 1596-1601, Nov./Dec. 2003.

[1.80] M. E. Baran and N. R. Mahajan, "Overcurrent protection on voltage-source-converter-based multiterminal DC distribution systems," *IEEE Trans. Power Del.*, vol. 22, no. 1, pp. 406-412, Jan. 2007.

[1.81] F. Blaabjerg and J. K. Pederson, "A new low-cost, fully fault-protected PWM-VSI inverter with true phase-current information," *IEEE Trans. Power Electron.*, vol. 12, no. 1, pp. 187-197, Jan. 1997.

[1.82] L. Tang and B. T. Ooi, "Locating and isolating DC faults in multi-terminal DC systems," *IEEE Trans. Power Del.*, vol. 22, no. 3, pp. 1877-1884, Jul. 2007.

[1.83] L. Tang and B. T. Ooi, "Protection of VSC-multi-terminal HVDC against DC faults," in *Proc. IEEE 33rd Annual Power Electronics Specialists Conf.*, vol. 2, pp. 719-724, Cairns, Queensland, Australia, 23-27 Jun. 2002.

[1.84] N. Gibo, K. Takenaka, S. C. Verma, S. Sugimoto, and S. Ogawa, "Protection scheme of voltage sourced converters based HVDC system under dc fault," *IEEE PES Asia Pacific Trans. Distr. Conf. and Exhib.*, vol. 2, pp. 1320-1325, 6-10 Oct. 2002.

Chapter 2

Doubly-Fed Induction Generator Fault Protection Schemes

2.1 Introduction

For wind power generation systems, the doubly-fed induction generator (DFIG) currently dominates with its variable wind speed tracking ability, and relatively low cost compared to full-rated converter systems, e.g. permanent magnet synchronous generator (PMSG). However, a significant disadvantage of the DFIG is its vulnerability to grid disturbances because the stator windings are connected to the grid through a transformer and switchgear with only the rotor-side buffered from the grid via a partially rated converter. Therefore, to protect the wind farm from interruptions due to onshore grid faults and wind farm faults, a crowbar protects the induction generator and associated power electronic devices. This protection system is widely used in industrial applications.

A major disadvantage of crowbar protection is that the rotor-side converter (RSC) has to be disabled when the crowbar is active and therefore the generator consumes reactive power leading to further deterioration of grid voltage. In line with developing fault ride-through (FRT) requirements, an active crowbar control scheme is proposed [2.1], [2.2] to shorten the time the crowbar is in operation but this does not avoid the reactive power consumption. Researchers have developed a new fault-control strategy [2.3] and a fault-tolerant series grid-side converter (GSC) topology [2.4]. However, these make the control systems complex or increase the issues with control coordination between normal and fault operation.

A series resistor can share the rotor circuit voltage and hence limit the rotor current during the fault, and is an alternative to crowbar protection. However, to the author's

knowledge, there has been no published literature on such a series resistor-based protection scheme. Therefore, the research in this chapter assesses series protection for effective turbine and converter protection during various fault conditions.

The chapter is organised as follows. In Section 2.2, existing protection schemes for DFIG systems are summarised. Then, a protection scheme with series dynamic resistor (SDR) connected to the rotor winding is proposed. The faults that can occur in wind farms and the currents in the rotor windings of DFIGs are discussed in detail as the basis of the converter protection scheme design: fault rotor current expressions are given theoretically and with simulation results; and the difference between rotor current characteristics for symmetrical and asymmetrical faults is discussed which highlights the advantage of series dynamic resistors as the primary protection of the converter. In Section 2.4, a new converter protection scheme combining the series dynamic resistor and the crowbar is introduced. Analysis and discussion of PSCAD/EMTDC simulations are provided in Section 2.3 and 2.5.

2.2 Converter Protection Schemes for DFIG

2.2.1 Crowbar Protection

The prevalent DFIG protection scheme is crowbar protection. A crowbar is a set of resistors that are connected in parallel with the rotor winding on occurrence of an interruption, bypassing the rotor-side converter. The active crowbar control scheme connects the crowbar resistance when necessary and disables it to resume DFIG control.

For active crowbar control schemes, the control signals are activated by the rotor-side converter devices [which are usually insulated-gate bipolar transistors (IGBTs)]. These have voltage and current limits that must not be exceeded. Therefore, the rotor-side converter voltages and currents are the critical regulation references. The DC-link bus voltage can increase rapidly under these conditions, so it is also used as a monitored variable for crowbar triggering. Bi-directional thyristors [2.5], gate turn-off thyristors (GTOs) [2.2], [2.6] or IGBTs [2.7] are typically used for crowbar switching.

2.2.2 DC-Chopper

In [2.2] and [2.8], a braking resistor (DC-chopper) is connected in parallel with the DC-link capacitor to limit the overcharge during low grid voltage. This protects the IGBTs from overvoltage and can dissipate energy, but this has no effect on the rotor current. It is also used as protection for the DC-link capacitor in full-rated converter topologies, for example, based on PMSGs [2.9].

2.2.3 Series Dynamic Resistor

In a similar way to the series dynamic braking resistor [2.10], which has been used in the stator side of generators, a dynamic resistor is proposed to be switched in series with the rotor (series dynamic resistor) and this limits the rotor overcurrent. Being controlled by a power electronic switch, in normal operation, the switch is on and the resistor is bypassed; during fault conditions, the switch is off and the resistor is connected in series to the rotor winding.

The difference between the series dynamic resistor and the crowbar or DC-link braking resistor is its topology. The latter are shunt-connected and control the voltage while the series dynamic resistor has the distinct advantage of controlling the current magnitude directly. Moreover, with the series dynamic resistor, the high voltage will be shared by the resistance because of the series topology; therefore, the induced overvoltage may not lead to the loss of converter control. Hence, it not only controls the rotor overvoltage which could cause the rotor-side converter to lose control, but also limits the high rotor current. In addition, limiting the current reduces the charging current of the DC-link capacitor, which helps avoid DC-link overvoltage. Therefore, with the series dynamic resistor, the rotor-side converter does not need to be inhibited during the fault.

The crowbar is adequate for protection of the wind turbine system during grid faults in onshore developments. The adverse impact of temporarily losing rotor-side control of a DFIG in a small-scale wind farm can be tolerated since it only involves a small amount of reactive power consumption – which is not presently the case for large-scale offshore wind farms. The series topology is straightforward enough to limit the overcurrent and share overvoltage but there appears to be no literature investigating its use.

To demonstrate the protection schemes and their interaction with the rotor circuit, the rotor equivalent circuit is described first with the general Park's model of induction generators. From the voltage and flux equations of induction generators in a static stator-oriented reference frame [2.11]

$$\vec{v}_s = R_s\vec{i}_s + \frac{d\vec{\psi}_s}{dt} \tag{2.1}$$

$$\vec{v}_r = R_r\vec{i}_r + \frac{d\vec{\psi}_r}{dt} - j\omega_r\vec{\psi}_r \tag{2.2}$$

$$\vec{\psi}_s = L_s\vec{i}_s + L_m\vec{i}_r \tag{2.3}$$

$$\vec{\psi}_r = L_m\vec{i}_s + L_r\vec{i}_r \tag{2.4}$$

where $\vec{v}_s$ is imposed by the grid. The rotor voltage $\vec{v}_r$ is controlled by the rotor-side converter and used to perform generator control.

From (2.3) and (2.4) $\vec{i}_s$ can be eliminated to obtain an expression, eliminating $\vec{\psi}_r$

$$\vec{v}_r = \frac{L_m}{L_s}\left(\frac{d}{dt} - j\omega_r\right)\vec{\psi}_s + \left[R_r + L_r\left(1 - \frac{L_m^2}{L_sL_r}\right)\left(\frac{d}{dt} - j\omega_r\right)\right]\cdot\vec{i}_r . \tag{2.5}$$

Defining the leakage factor as $\sigma = 1 - \frac{L_m^2}{L_sL_r}$. (2.6)

Then, using a voltage source $\vec{v}_{ro}$ to represent the voltage due to the stator flux such that $\vec{v}_{ro} = \frac{L_m}{L_s}\left(\frac{d}{dt} - j\omega_r\right)\vec{\psi}_s$. (2.7)

(2.5) becomes

$$\vec{v}_r = \vec{v}_{ro} + \left[R_r + \sigma L_r\left(\frac{d}{dt} - j\omega_r\right)\right]\cdot\vec{i}_r . \tag{2.8}$$

The rotor voltage in (2.8) can be expressed in a rotor reference frame (i.e. multiply both sides by $e^{-j\omega_r t}$)

$$\vec{v}_r^{\,r} = \vec{v}_{ro}^{\,r} + R_r \cdot \vec{i}_r^{\,r} + \sigma L_r \frac{d\vec{i}_r^{\,r}}{dt}. \tag{2.9}$$

This is the relationship between rotor voltage and current. Therefore, the rotor equivalent circuit is obtained and shown with all the above protection schemes in Figure 2.1.

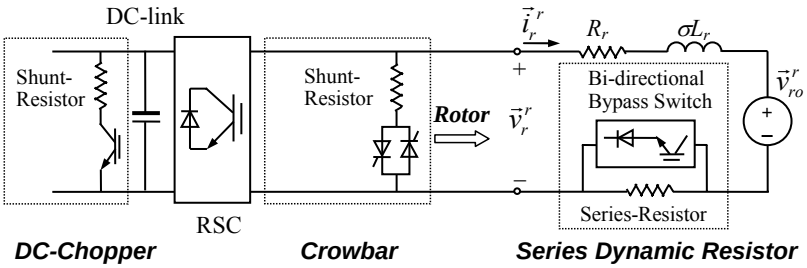

Figure 2.1: DFIG rotor equivalent circuit with all protection schemes shown.

2.3 DFIG Rotor Currents during Fault Conditions

DFIG rotor currents under three-phase short-circuit faults have been thoroughly analysed. In [2.12], exact expressions of stator and rotor currents during the short-circuit are derived mathematically. The approximate maximum stator fault current expression was also discussed from the analysis of DFIG physical response with crowbar protection [2.5]. However, there has been no analysis of fault currents during less serious voltage dips or asymmetrical disturbances. Nonetheless, this is important for the design of DFIG protection systems. In this chapter, the rotor current expressions during various fault conditions will be deduced on the basis of the analysis of [2.11] and [2.13].

The phase-*a* rotor voltage expression is

$$v_{ra}(t) = \mathrm{Re}\{\vec{v}_{ro}^{\,r}\} + R_r \cdot i_{ra}(t) + \sigma L_r \frac{di_{ra}(t)}{dt}. \tag{2.10}$$

This can be written as a linear differential equation for $i_{ra}(t)$

$$\frac{di_{ra}(t)}{dt}+\frac{R_r}{\sigma L_r}i_{ra}(t)=\frac{1}{\sigma L_r}\left[v_{ra}(t)-\mathrm{Re}\{\vec{v}_{ro}^{\,r}\}\right] \tag{2.11}$$

where, with the converter in operation, $v_{ra}(t) = V_r\cos(s\omega_s t + \beta)$, and s is the slip, β is the phase-a rotor voltage angle at the instant the fault occurs.

2.3.1 Symmetrical Fault Conditions

For a symmetrical voltage disturbance on the stator side, if there is a three-phase step amplitude change from V_s to $(1–p)V_s$ (p is the voltage dip ratio), $\vec{v}_{ro}^{\,r}$ in (2.9) can exceed the maximum voltage that the rotor converter can generate, which causes current control to fail. The voltage is [2.11]

$$\vec{v}_{ro}^{\,r}=(1-p)V_s\frac{L_m}{L_s}se^{js\omega_s t}-\frac{L_m}{L_s}\left(\frac{1}{\tau_s}+j\omega_r\right)\frac{pV_s}{j\omega_s}e^{-\frac{t}{\tau_s}}. \tag{2.12}$$

With time constants defined as

$$\tau_r=\frac{\sigma L_r}{R_r};\quad \tau_s=\frac{L_s}{R_s};\quad \tau=\frac{\tau_r\tau_s}{\tau_s-\tau_r}. \tag{2.13}$$

Equation (2.12) can be simplified by omitting $1/\tau_s$, which is very small because of the small stator resistance of the generator, therefore

$$\vec{v}_{ro}^{\,r}\approx V_s\frac{L_m}{L_s}\left[s(1-p)e^{js\omega_s t}-(1-s)pe^{-j\omega_r t}e^{-\frac{t}{\tau_s}}\right]. \tag{2.14}$$

From (2.11) and (2.14), the final expression of $i_{ra}(t)$ can be solved and divided into four components

$$i_{ra}(t)=i_{DC}+i_{vr}+i_{vrf}+i_{vrn} \tag{2.15}$$

where the components are

$$i_{DC} = \left\{ i_{ra}(t_0^-) - \frac{1}{\sigma L_r} \frac{\tau_r}{1+\tau_r^2 (s\omega_s)^2} \left[V_r \cos\beta - V_s \frac{L_m}{L_s} s(1-p) \right] - \frac{1}{\sigma L_r} V_s \frac{L_m}{L_s} (1-s) p \frac{\tau}{1+\tau^2 \omega_r^2} \right\} e^{-\frac{t}{\tau_r}} \quad (2.16)$$

$$i_{vr} = \frac{V_r}{\sigma L_r} \left[\frac{\tau_r}{1+\tau_r^2 \omega_r^2} \cos(s\omega_s t + \beta) + \frac{\tau_r^2 \omega_r}{1+\tau_r^2 \omega_r^2} \sin(s\omega_s t + \beta) \right] \quad (2.17)$$

$$i_{vrf} = -\frac{1}{\sigma L_r} V_s \frac{L_m}{L_s} s(1-p) \times \left[\frac{\tau_r}{1+\tau_r^2 (s\omega_s)^2} \cos(s\omega_s t) + \frac{\tau_r^2 s\omega_s}{1+\tau_r^2 (s\omega_s)^2} \sin(s\omega_s t) \right] \quad (2.18)$$

$$i_{vrn} = \frac{V_s}{\sigma L_r} \frac{L_m}{L_s} (1-s) p \times \left[\frac{\tau}{1+\tau^2 \omega_r^2} \cos(\omega_r t) + \frac{\tau^2 \omega_r}{1+\tau^2 \omega_r^2} \sin(\omega_r t) \right] e^{-\frac{t}{\tau_s}} . \quad (2.19)$$

The components are listed in Table 2.1 with the frequency and time constant characteristics.

Table 2.1: Symmetrical Fault Rotor Current Components

Component	Frequency	Decaying time constant
i_{DC}	DC	τ_r
i_{vr}	$s\omega_s$	-
i_{vrf}	$s\omega_s$	-
i_{vrn}	ω_r	τ_s

2.3.2 Asymmetrical Fault Conditions

For asymmetrical faults, the stator voltage is divided into three parts: positive-, negative-, and zero-sequence components, using symmetrical component theory [2.13]

$$\vec{v}_s = \vec{V}_{s1} e^{j\omega_s t} + \vec{V}_{s2} e^{-j\omega_s t} + \vec{V}_{s0} \quad (2.20)$$

Then, $\vec{v}_{ro}^{\,r}$ in (2.9) can also be expressed as

$$\vec{v}_{ro}^{\,r} = \vec{v}_{r1}^{\,r} + \vec{v}_{r2}^{\,r} + \vec{v}_{rn}^{\,r} \quad (2.21)$$

where

$$\vec{v}_{r1}^{\,r} = V_{s1} \frac{L_m}{L_s} s e^{js\omega_s t} \quad (2.22)$$

$$\vec{v}_{r2}^{\,r} = V_{s2}\frac{L_m}{L_s}(s-2)e^{-j(2-s)\omega_s t} \tag{2.23}$$

$$\vec{v}_{rn}^{\,r} \approx -j\omega_r \frac{L_m}{L_s}\vec{\psi}_{n0}e^{-\frac{t}{\tau_s}}e^{-j\omega_r t} \tag{2.24}$$

The components $\vec{V}_{s1}$, $\vec{V}_{s2}$, $\vec{V}_{s0}$, and $\vec{\psi}_{n0}$ depend on the type of fault.

1) Single-Phase Voltage Dip:

Phase *a* suffers a voltage dip. The positive-, negative-, and zero-sequence components of the stator voltage are

$$\begin{cases} \vec{V}_{s1} = V_s(1-p/3) \\ \vec{V}_{s2} = V_s(-p/3) \\ \vec{V}_{s0} = V_s(-p/3) \end{cases} \tag{2.25}$$

where p is the phase-*a* voltage dip ratio due to the fault. Therefore, the aforementioned $\vec{v}_{r0}^{\,r}$ components are

$$\vec{v}_{r1}^{\,r} = V_s(1-p/3)\frac{L_m}{L_s}se^{js\omega_s t} \tag{2.26}$$

$$\vec{v}_{r2}^{\,r} = V_s(-p/3)\frac{L_m}{L_s}(s-2)e^{-j(2-s)\omega_s t} \tag{2.27}$$

From the natural flux initial value analysis in [2.13]

$$\vec{\psi}_{n0} = \frac{V_s(2/3)p}{\omega_s} \tag{2.28}$$

$$\vec{v}_{rn}^{\,r} \approx -j\frac{2}{3}V_s\frac{L_m}{L_s}(1-s)pe^{-\frac{t}{\tau_s}}e^{-j\omega_r t}. \tag{2.29}$$

hence $$\vec{v}_{ro} \approx V_s\frac{L_m}{L_s}s\left(1-\frac{p}{3}\right)e^{js\omega_s t} - V_s\frac{L_m}{L_s}(s-2)\frac{p}{3}e^{-j(2-s)\omega_s t} - j\frac{2}{3}V_s\frac{L_m}{L_s}(1-s)pe^{-\frac{t}{\tau_s}}e^{-j\omega_r t} \tag{2.30}$$

From (2.11) and (2.30), the final expression of $i_{ra}(t)$ can be solved and divided into five components

$$i_{ra}(t) = i_{DC} + i_{vr} + i_{vr1} + i_{vr2} + i_{vrn} \tag{2.31}$$

where the components are

$$\begin{aligned} i_{DC} = &\left\{ i_{ra}(t_0^-) - \frac{1}{\sigma L_r} \frac{\tau_r}{1+\tau_r^2 (s\omega_s)^2} \left[V_r \cos\beta - V_s \frac{L_m}{L_s} s\left(1-\frac{p}{3}\right) \right] \right. \\ &\left. - \frac{1}{\sigma L_r} V_s \frac{L_m}{L_s} \left[(s-2)\frac{p}{3} \frac{\tau_r}{1+\tau_r^2 (2-s)^2 \omega_s^2} + \frac{2}{3}(1-s) p \frac{-\tau^2 \omega_r}{1+\tau^2 \omega_r^2} \right] \right\} e^{-\frac{t}{\tau_r}} \end{aligned} \tag{2.32}$$

$$i_{vr} = \frac{V_r}{\sigma L_r} \left[\frac{\tau_r}{1+\tau_r^2 \omega_r^2} \cos(s\omega_s t + \beta) + \frac{\tau_r^2 \omega_r}{1+\tau_r^2 \omega_r^2} \sin(s\omega_s t + \beta) \right] \tag{2.33}$$

$$i_{vr1} = -\frac{V_s}{\sigma L_r} \frac{L_m}{L_s} s\left(1-\frac{p}{3}\right) \times \left[\frac{\tau_r}{1+\tau_r^2 (s\omega_s)^2} \cos(s\omega_s t) + \frac{\tau_r^2 s\omega_s}{1+\tau_r^2 (s\omega_s)^2} \sin(s\omega_s t) \right] \tag{2.34}$$

$$i_{vr2} = \frac{1}{\sigma L_r} V_s \frac{L_m}{L_s} (s-2)\frac{p}{3} \times \left[\frac{\tau_r}{1+\tau_r^2 (2-s)^2 \omega_s^2} \cos\left((2-s)\omega_s t\right) + \frac{\tau_r^2 (2-s)\omega_s}{1+\tau_r^2 (2-s)^2 \omega_s^2} \sin\left((2-s)\omega_s t\right) \right] \tag{2.35}$$

$$i_{vrn} = \frac{2}{3} \frac{V_s}{\sigma L_r} \frac{L_m}{L_s} (1-s) p \times \left[\frac{-\tau^2 \omega_r}{1+\tau^2 \omega_r^2} \cos(\omega_r t) + \frac{\tau}{1+\tau^2 \omega_r^2} \sin(\omega_r t) \right] e^{-\frac{t}{\tau_s}} . \tag{2.36}$$

2) Phase-to-Phase Fault:

Here, phases *b* and *c* are shorted together leading to a voltage dip at the stator terminals. Then the positive-, negative-, and zero-sequence components of the stator voltage are

$$\begin{cases} \vec{V}_{s1} = V_s (1 - p/2) \\ \vec{V}_{s2} = V_s (p/2) \\ \vec{V}_{s0} = V_s (p/2) \end{cases} \tag{2.37}$$

where p is the phase *b* and *c* voltage dip ratio due to the fault. Also, the initial value of natural flux is [2.13]

$$\vec{\psi}_{n0} = \frac{V_s p}{\omega_s}. \tag{2.38}$$

The current expression, in this case, is similar to the single-phase fault case, with the same five components, but different amplitudes. The components are

$$i_{DC} = \left\{ i_{ra}(t_0^-) - \frac{1}{\sigma L_r} \frac{\tau_r}{1+\tau_r^2 (s\omega_s)^2} \left[V_r \cos\beta - V_s \frac{L_m}{L_s} s\left(1-\frac{p}{2}\right) \right] \right. \tag{2.39}$$
$$\left. + \frac{1}{\sigma L_r} V_s \frac{L_m}{L_s} \left[(s-2)\frac{p}{2} \frac{\tau_r}{1+\tau_r^2 (2-s)^2 \omega_s^2} - (1-s)p \frac{-\tau^2 \omega_r}{1+\tau^2 \omega_r^2} \right] \right\} e^{-\frac{t}{\tau_r}}$$

$$i_{vr} = \frac{V_r}{\sigma L_r} \left[\frac{\tau_r}{1+\tau_r^2 \omega_r^2} \cos(s\omega_s t + \beta) + \frac{\tau_r^2 \omega_r}{1+\tau_r^2 \omega_r^2} \sin(s\omega_s t + \beta) \right] \tag{2.40}$$

$$i_{vr1} = -\frac{V_s}{\sigma L_r} \frac{L_m}{L_s} s\left(1-\frac{p}{2}\right) \times \left[\frac{\tau_r}{1+\tau_r^2 (s\omega_s)^2} \cos(s\omega_s t) + \frac{\tau_r^2 s\omega_s}{1+\tau_r^2 (s\omega_s)^2} \sin(s\omega_s t) \right] \tag{2.41}$$

$$i_{vr2} = -\frac{1}{\sigma L_r} V_s \frac{L_m}{L_s} (s-2)\frac{p}{2} \times \left[\frac{\tau_r}{1+\tau_r^2 (2-s)^2 \omega_s^2} \cos((2-s)\omega_s t) + \frac{\tau_r^2 (2-s)\omega_s}{1+\tau_r^2 (2-s)^2 \omega_s^2} \sin((2-s)\omega_s t) \right] \tag{2.42}$$

$$i_{vrn} = \frac{1}{\sigma L_r} V_s \frac{L_m}{L_s} (1-s)p \times \left[\frac{-\tau^2 \omega_r}{1+\tau^2 \omega_r^2} \cos(\omega_r t) + \frac{\tau}{1+\tau^2 \omega_r^2} \sin(\omega_r t) \right] e^{-\frac{t}{\tau_s}}. \tag{2.43}$$

The components are listed in Table 2.2 with the frequency and time constants.

Table 2.2: Asymmetrical Fault Rotor Current Components

Component	Frequency	Decaying time constant
i_{DC}	DC	τ_r
i_{vr}	$s\omega_s$	-
i_{vr1}	$s\omega_s$	-
i_{vr2}	$(2–s)\ \omega_s$	-
i_{vrn}	ω_r	τ_s

The rotor currents during the fault are simulated in PSCAD/EMTDC to compare with the analysis, as shown in Figure 2.2. The induction generator parameters are shown in Table 2.3, and the rotor-side converter is controlled using a voltage-regulating vector controller. The simulations have the rotor-side converter connected when faults occur.

Table 2.3: Induction Generator Parameters [2.3]

Parameter	Value	Parameter	Value
Rated power P_n	2 MW	Ratio N_s/N_r	0.63
Rated stator voltage V_{sn}	690 V	Inertia constant H	3.5 s
Rated frequency f_s	50 Hz	Pole pair no. P_p	2
Stator leakage inductance L_{ls}	0.105 p.u.	Stator resistance R_s	0.0050 p.u.
Rotor leakage inductance L_{lr}	0.100 p.u.	Rotor resistance R_r	0.0055 p.u.
Magnetizing inductance L_m	3.953 p.u.		

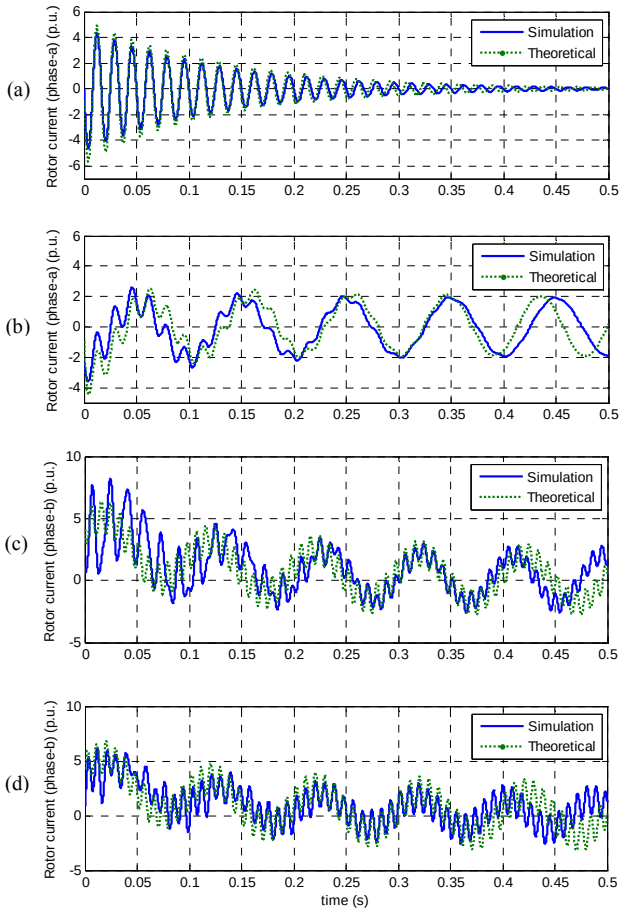

Figure 2.2: Comparison of simulation and theoretical rotor currents during fault conditions (for 0.5 s): (a) three-phase 1.0 p.u. voltage dip; (b) three-phase 0.6 p.u. voltage dip; (c) single-phase (phase *a*) voltage dip of 1.0 p.u.; (d) phase-to-phase (phase *b* to *c*) short circuit.

Each fault displays different frequency components and characteristics. The three-phase short-circuit fault causes an abrupt change at the moment the fault with highest peak values [Figure 2.3(a)] but with relatively short duration [see Figure 2.2(a) and Figure 2.3(a)]. However, for the less serious voltage dip and asymmetrical

faults [see Figure 2.2(b)–(d)], the high magnitude, high-frequency oscillation makes it is impossible to switch off the crowbar protection. To protect the system, the converter has to be inhibited and then the DFIG absorbs reactive power from the grid, which adversely affects grid recovery.

The comparisons show that the analysis is in accordance with theory and is valid for the study of the fault conditions. Therefore it will contribute to the converter protection scheme design in Section 2.4. All three-phase rotor currents are shown in Figure 2.3. The same simulation system will also be used for the protection scheme verification that follows.

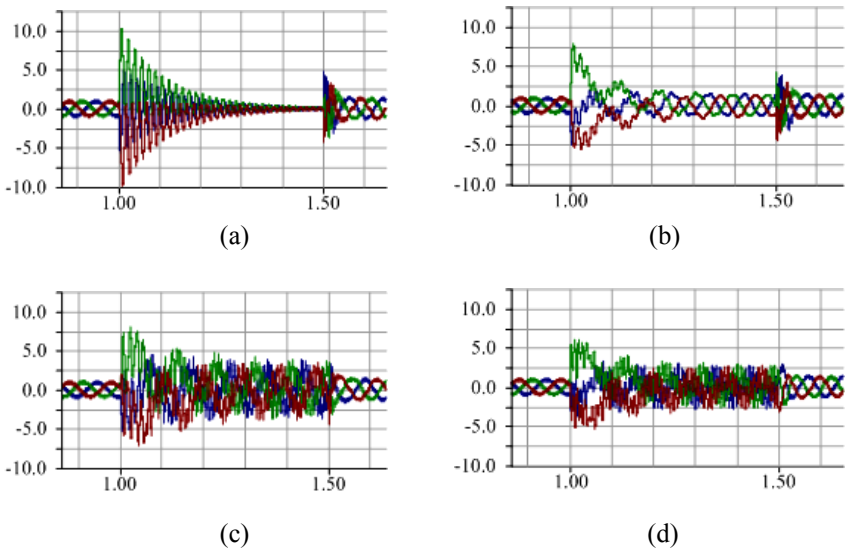

Figure 2.3: Three-phase rotor currents during different fault conditions (for 0.5 s): (a) three-phase 1.0 p.u. voltage dip; (b) three-phase 0.6 p.u. voltage dip; (c) single-phase (phase *a*) 1.0 p.u. voltage dip; (d) phase-to-phase (phase *b* to *c*) short circuit.

2.4 Protection Scheme Based on Series Dynamic Resistor

The above rotor fault current analysis and simulation highlights a major difference between symmetrical and asymmetrical fault currents. For symmetrical faults, the rotor currents increase abruptly both at the beginning and the end of the fault. The crowbar need only switch on for a short time. For asymmetrical dips, the crowbar does not solve the problem because it needs to be active throughout the duration of

the dip, requiring the generator to be disconnected from the grid. This can be explained by the difference in flux components for different faults [2.13].

In this section, a new protection scheme based on a series dynamic resistor is proposed which also combines and coordinates the existing crowbar and DC-chopper protection. A series dynamic resistor is used as the primary protection, with the crowbar circuit used if the series dynamic resistor cannot protect because of a deteriorating situation. The crowbar is engaged only at the beginning or the end of the fault, if required. The DC-chopper is used for DC-link overvoltage limitation.

2.4.1 Switching Strategy

It is observed in the previous section that asymmetrical faults are more hazardous than symmetrical faults for the DFIG because of the continuous overcurrent in the rotor. From the above overcurrent analysis a switching strategy is devised to determine when to engage the protection measures using current thresholds.

1) Protection Engaged: The voltage change is not as abrupt as the current and can be shared by the series dynamic resistor. For the DC-link voltage, its change can be further reduced by the DC-chopper. Therefore, only rotor currents are monitored for series dynamic resistor and crowbar protections.

2) Protection Disengaged: The protections themselves can be seen as disturbances. To avoid the protections switching frequently because of the high-frequency component of rotor current, the switch off is delayed for a period of the high frequency component, i.e. $t\_delay = 2\pi/(1-s)\omega_s \approx 2\pi/\omega_s$ after all the three-phase currents decrease below the threshold value.

The final switching strategy is shown in Figure 2.4.

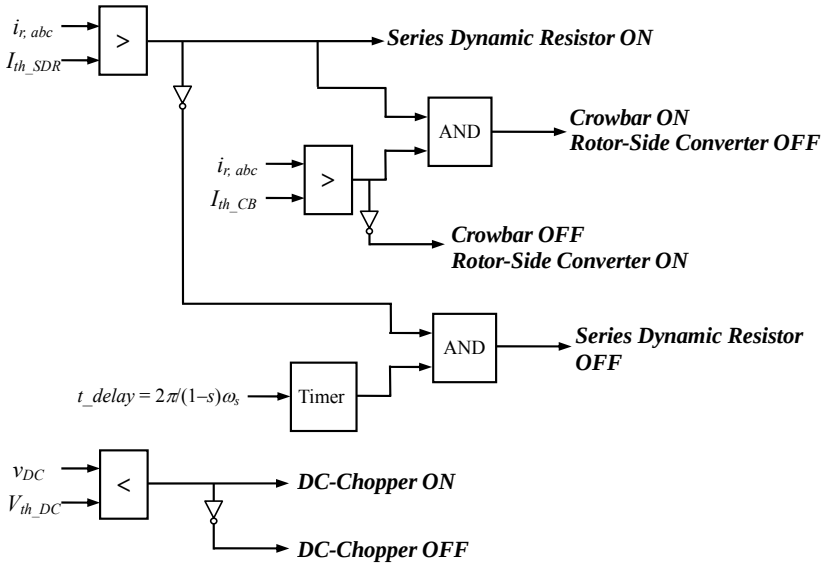

Figure 2.4: Combined converter protection switching strategy (for subscripts: *th* – threshold values; *CB* – Crowbar; *SDR* – Series Dynamic Resistor).

2.4.2 Series Dynamic Resistance Calculations

Resistance values are calculated for the most serious condition (with the highest peak current value): symmetrical voltage dip up to 1.0 p.u. The rotor current expressions are (2.15) – (2.19). Due to the small stator resistance, the following approximations are made: $e^{-t/\tau_s} \approx 1$; $\tau \approx \tau_r$.

Then, the current components are expressed as a single trigonometric function as

$$i_{DC} = \left\{ i_{ra}(t_0^-) - \frac{1}{\sigma L_r} \frac{\tau_r}{1+\tau_r^2 (s\omega_s)^2} V_r \cos\beta - \frac{1}{\sigma L_r} V_s \frac{L_m}{L_s} (1-s) \frac{\tau}{1+\tau^2 \omega_r^2} \right\} e^{-\frac{t}{\tau_r}} \tag{2.44}$$

$$i_{vr} = \frac{V_r}{\sigma L_r} \frac{\tau_r}{\sqrt{1+\tau_r^2 \omega_r^2}} \sin(s\omega_s t + \beta + \varphi) \tag{2.45}$$

$$i_{vrf} = 0 \tag{2.46}$$

$$i_{vrn} = \frac{1}{\sigma L_r} V_s \frac{L_m}{L_s} (1-s) \frac{\tau_r}{\sqrt{1+\tau_r^2 \omega_r^2}} \sin(\omega_r t + \varphi) \tag{2.47}$$

where $\varphi = \tan^{-1}\left(\frac{1}{\tau_r \omega_r}\right)$.

Considering the amplitude of each component at the maximum current value

$$i_{ra,\max} = i_{ra}(t_0^-) - \frac{1}{\sigma L_r} V_s \frac{L_m}{L_s}(1-s)\frac{\tau_r}{1+\tau_r^2\omega_r^2} + \frac{V_r}{\sigma L_r}\frac{\tau_r}{\sqrt{1+\tau_r^2\omega_r^2}} + \frac{1}{\sigma L_r} V_s \frac{L_m}{L_s}(1-s)\frac{\tau_r}{\sqrt{1+\tau_r^2\omega_r^2}}. \quad (2.48)$$

Also, the boundary conditions are

$$i_{ra,\max} \le I_{th\_SDR},\ V_r \le V_{th\_RSC}. \quad (2.49)$$

Therefore, (2.48) and (2.49) are equations where τ_r can be solved. With the protection schemes

$$\tau_r = \frac{\sigma L_r}{R_r + R_{protection}}. \quad (2.50)$$

Then, the critical resistance value $R_{protection}$ can be calculated. If the rotor fault currents still cannot be limited effectively, the crowbar can be used as further protection. The total resistance is $R_{protection}$, includes R_{SDR} and R_{CB}. The current-limiting function is provided by the series dynamic resistor, hence the critical criterion of crowbar resistance is the voltage across it must be within the rotor voltage limit, for its shunt connection: $R_{CB} \times i_{r,\max} \le V_{r,\max}$. Therefore, the crowbar resistance is a small contribution to the total $R_{protection}$. This is simpler than using crowbar protection alone, where the resistance has a lower and upper limit. The minimum value of resistance is restricted by the rotor winding current limit, while the maximum is set by the voltage limit at the converter terminals [2.5].

2.5 Simulation Results

The proposed converter protection method is verified by PSCAD/EMTDC simulations. The generator parameters are listed in Table 2.3. The faults simulated are:

1) a three-phase voltage dip of 0.95 p.u. for 0.2 s;

2) a single-phase (phase *a*) grounding for 0.2 s;

3) a two-phase short-circuit (phase *b* to *c*) for 0.2 s; and

4) a three-phase voltage dip of 0.6 p.u. for 1.0 s.

The threshold values for calculating R_{SDR} and R_{CB} are set as I_{th_SDR} = 1.5 p.u., I_{th_CB} = 1.8 p.u. Rotor slip is s = –0.2 p.u. preceding the faults.

From (2.48) and (2.49), τ_r = 0.65 ms, $R_{protection}$ = 0.987 p.u. = 0.59 Ω. Then, the selected resistance values are R_{SDR} = 0.5 Ω, R_{CB} = 0.09 Ω. The value of DC-chopper resistance is not so critical as it is only related to the DC-link voltage, so here choose R_{DCC} = 0.5 Ω.

2.5.1 Symmetrical Fault Condition

Figures 2.5 and 2.6 show the system response to a 0.95 p.u. voltage dip for 0.2 s with and without protection respectively. In the simulation without protection, the rotor-side converter is blocked during the fault. The rotor currents reach around 10.0p.u. for the most serious phase. DC-link voltage and rotor speed both increase until the fault is cleared. Large electrical torque fluctuations occur.

In Figure 2.6, series dynamic resistor is switched in ten times in total to limit the rotor current. During the recovery of the fault, crowbar is switched in for five times with the series dynamic resistor connected as the rotor current increases beyond the crowbar threshold. The simulation results show that with series dynamic resistor protection, the first torque peak is safely avoided, while crowbar is helpful for protection during fault recovery. The rotor current amplitude is limited within 1.5 p.u., as required. This also restricts the DC-link voltage increase (less than 0.05 p.u. in Figure 2.6). The DC-chopper function is not required. The rotor speed increase is effectively restrained from 1.2 p.u. to 1.207 p.u. compared to 1.22 p.u. without protection.

The large 5.0 p.u. torque fluctuation at the start of the fault is avoided; compare Figure 2.5 to Figure 2.6 with the series dynamic resistor. However, a 7.0 p.u. torque fluctuation occurs during the fault recovery phase in Figure 2.6. This is due to the crowbar protection switching in as a further protection measure. The individual crowbar and SDR torque performances will be compared in Section 2.5.3 which

shows that all of the 7.0 p.u. torque pulsation that occurs at fault recovery is due to the crowbar circuit [see Figure 2.10 (d) and (e)]. Note that in Figure 2.5, T_m is in blue and T_e is in green and that in Figure 2.6, T_m is in green while T_e is in blue.

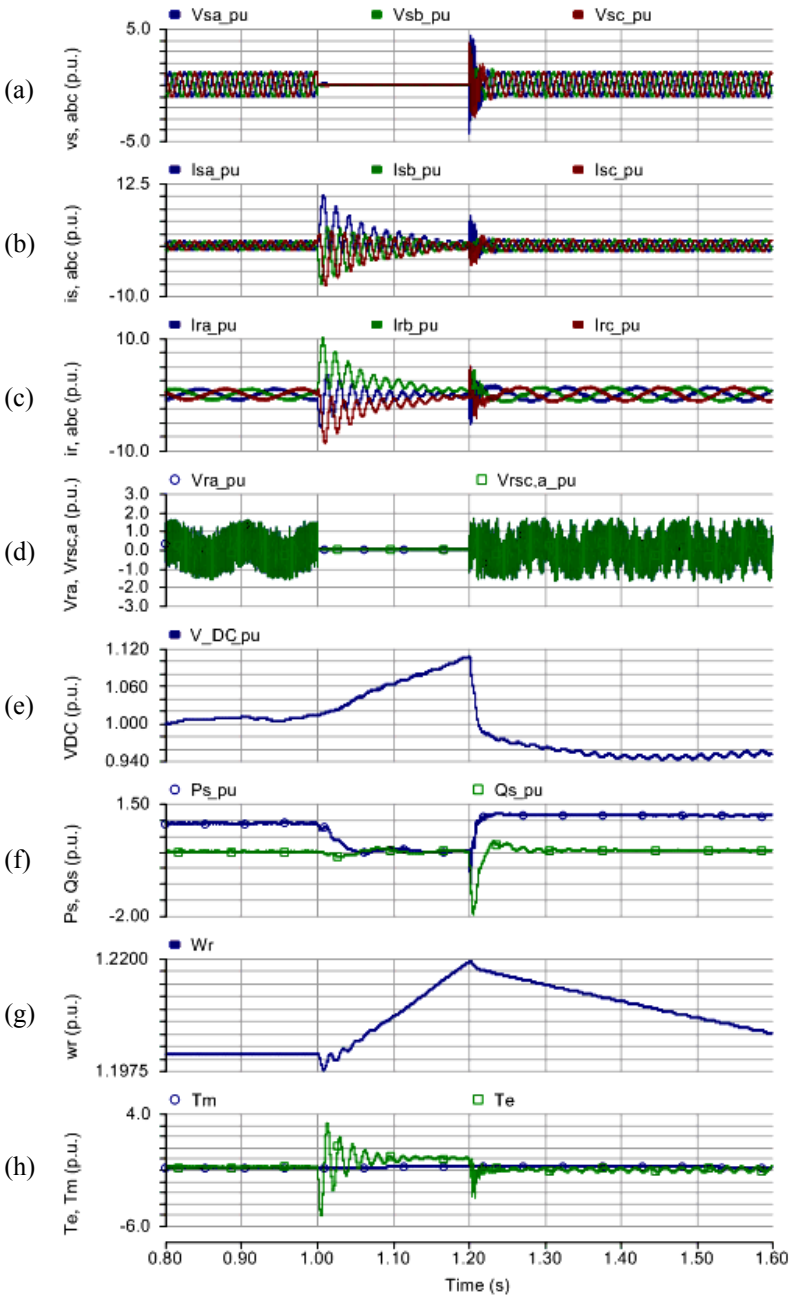

Figure 2.5: Three-phase 0.95 p.u. voltage dip for 0.2 s without protection: (a) three-phase stator voltages $v_{s\,a,b,c}$ [in per unit (p.u.)]; (b) three-phase stator currents $i_{s\,a,b,c}$ (p.u.); (c) three-phase rotor currents $i_{r\,a,b,c}$ (p.u.); (d) phase-*a* rotor voltage v_{ra} (p.u.) and phase-*a* RSC voltage $v_{rsc,a}$ (p.u.); (e) DC-link voltage v_{DC} (p.u.); (f) stator side active power P_s (p.u.) and reactive power Q_s (p.u.); (g) rotor speed ω_r (p.u.); (h) electrical torque T_e (p.u.) and mechanical torque T_m (p.u.).

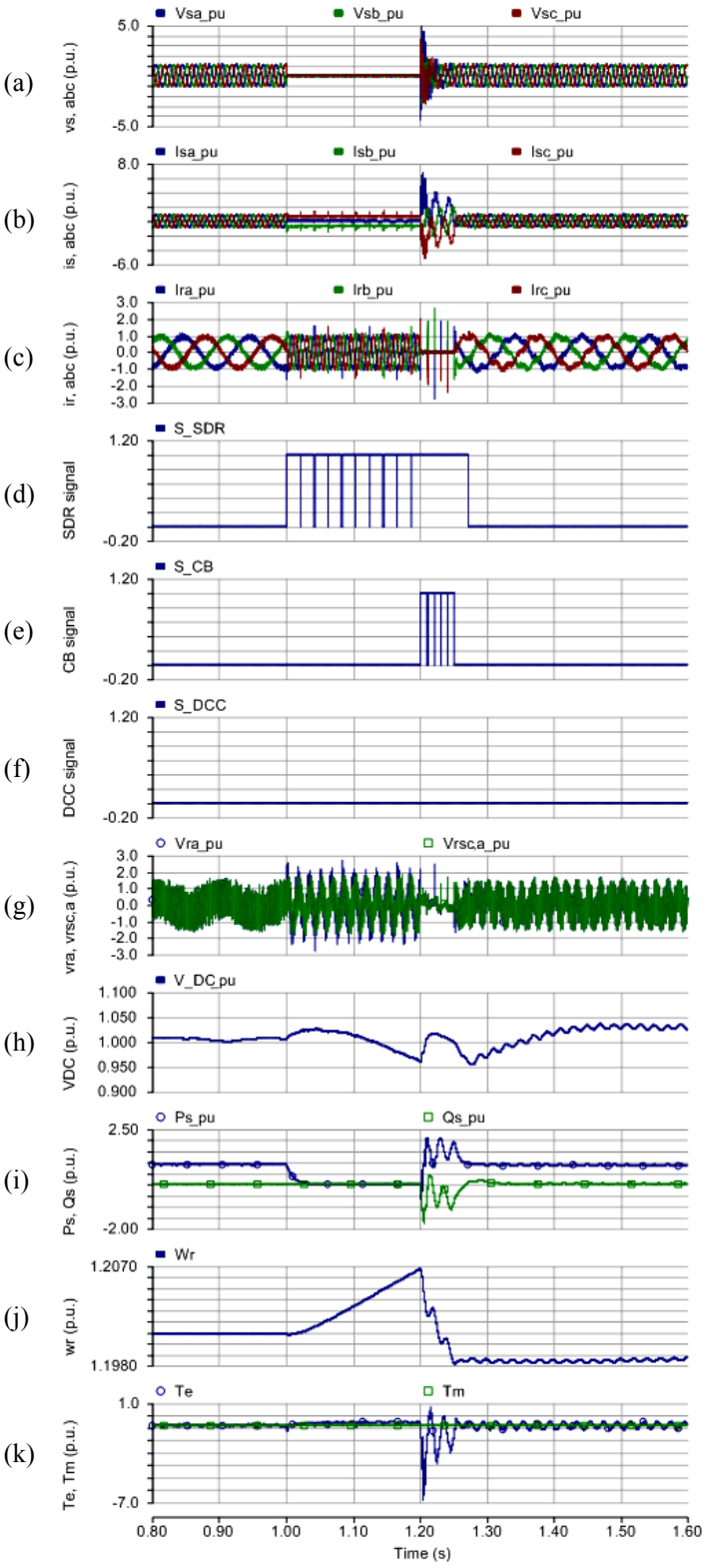

Figure 2.6: Three-phase 0.95 p.u. voltage dip for 0.2 s with converter protection: (a) three-phase stator voltages $v_{s\,a,b,c}$ [in per unit (p.u.)]; (b) three-phase stator currents $i_{s\,a,b,c}$ (p.u.); (c) three-phase rotor currents $i_{r\,a,b,c}$ (p.u.); (d) SDR switching signal S_{SDR}; (e) crowbar switching signal S_{CB}; (f) DC-chopper switching signal S_{DCC}; (g) phase-*a* rotor voltage v_{ra} (p.u.) and phase-*a* RSC voltage $v_{RSC,a}$ (p.u.); (h) DC-link voltage v_{DC} (p.u.); (i) stator side active power P_s (p.u.) and reactive power Q_s (p.u.); (j) rotor speed ω_r (p.u.); (k) electrical torque T_e (p.u.) and mechanical torque T_m (p.u.).

Although there is no rotor voltage monitoring in the switching strategy, it is still limited effectively to the value before the fault because of the voltage sharing ability of the series dynamic resistor. The rotor voltages display switching frequency components due to the pulse-width modulation of the rotor-side converter. The high voltage is shared across the series resistor and the converter which results in a lower converter side voltage ($v_{RSC,a}$ in Figure 2.7).

Large transients occur during the fault clearing mainly due to the impact of crowbar protection switching, but together with series dynamic resistor protection, the disturbances are clamped after about 0.05 s. It should be noted that whilst the crowbar is used in this particular case, it is not necessary under all faults.

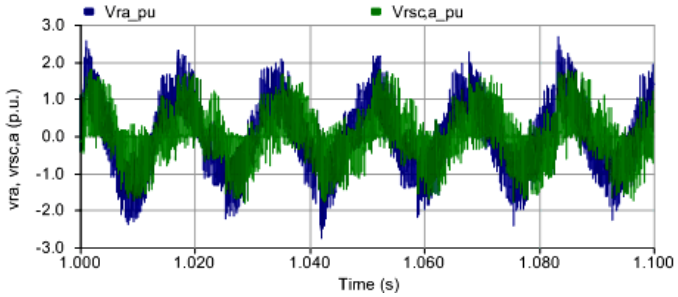

Figure 2.7: The rotor voltage v_{ra} [in per unit (p.u.)] and rotor-side converter voltage $v_{RSC,a}$ (p.u.) comparison (zoomed from 1 s to 1.1 s).

2.5.2 Asymmetrical Fault Conditions

Figures 2.8 and 2.9 show the system responses during asymmetrical fault conditions. The rotor currents are also limited within 1.5 p.u. For the phase-*a* fault in Figure 2.8, the series dynamic resistor and crowbar protection switching events are similar to the symmetrical fault conditions. However, there is one period of DC-chopper switching because of the gradual increase of DC-link voltage to 1.1 p.u. Instead of increasing, the rotor speed decreases because the DFIG is still under control with active power supplied to the grid. An overspeed condition is avoided as the electrical torque balances the mechanical torque from the wind turbine's blade system.

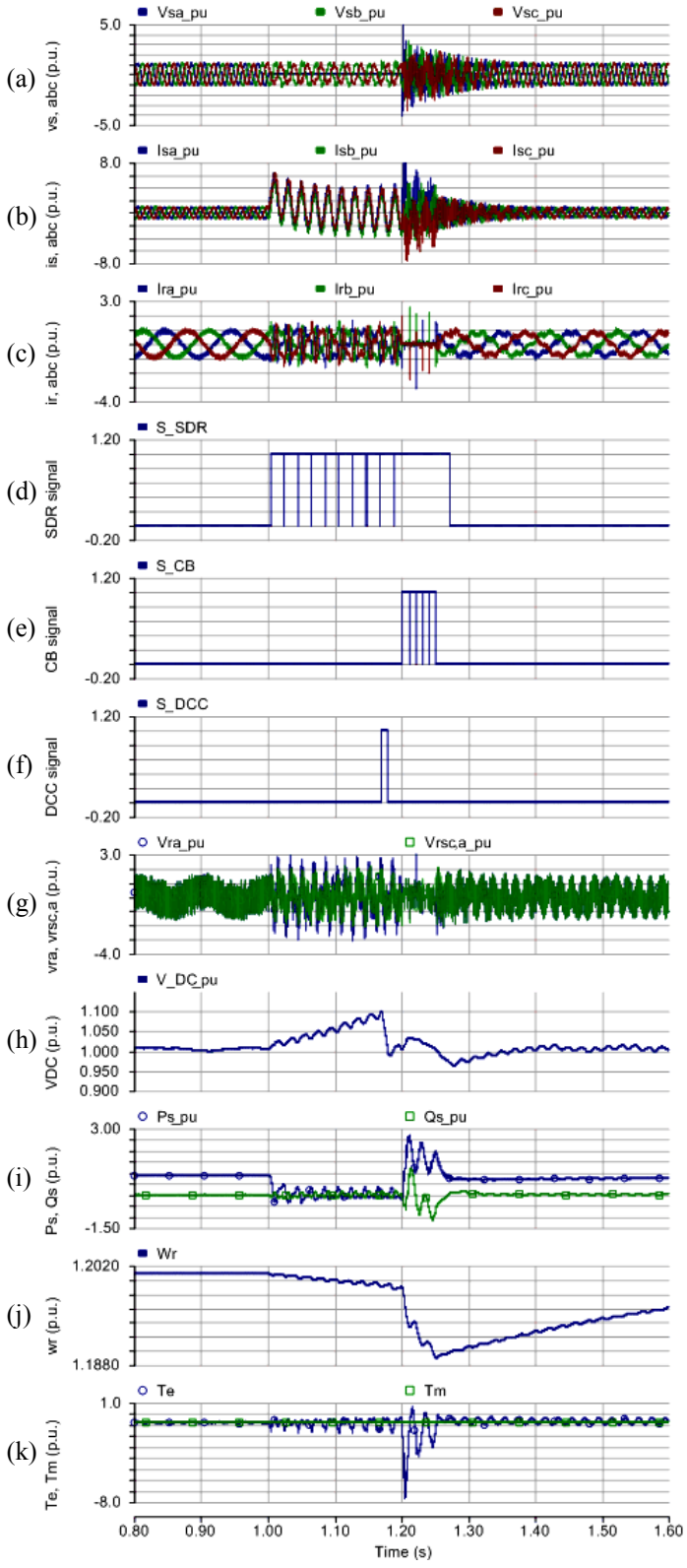

Figure 2.8: Phase-*a* 1.0 p.u. voltage dip for 0.2 s with converter protection: (a) three-phase stator voltages $v_{s\ a,b,c}$ [in per unit (p.u.)]; (b) three-phase stator currents $i_{s\ a,b,c}$ (p.u.); (c) three-phase rotor currents $i_{r\ a,b,c}$ (p.u.); (d) SDR switching signal S_{SDR}; (e) crowbar switching signal S_{CB}; (f) DC-chopper switching signal S_{DCC}; (g) phase-*a* rotor voltage v_{ra} (p.u.) and phase-*a* RSC voltage $v_{RSC,a}$ (p.u.); (h) DC-link voltage v_{DC} (p.u.); (i) stator side active power P_s (p.u.) and reactive power Q_s (p.u.); (j) rotor speed ω_r (p.u.); (k) electrical torque T_e (p.u.) and mechanical torque T_m (p.u.).

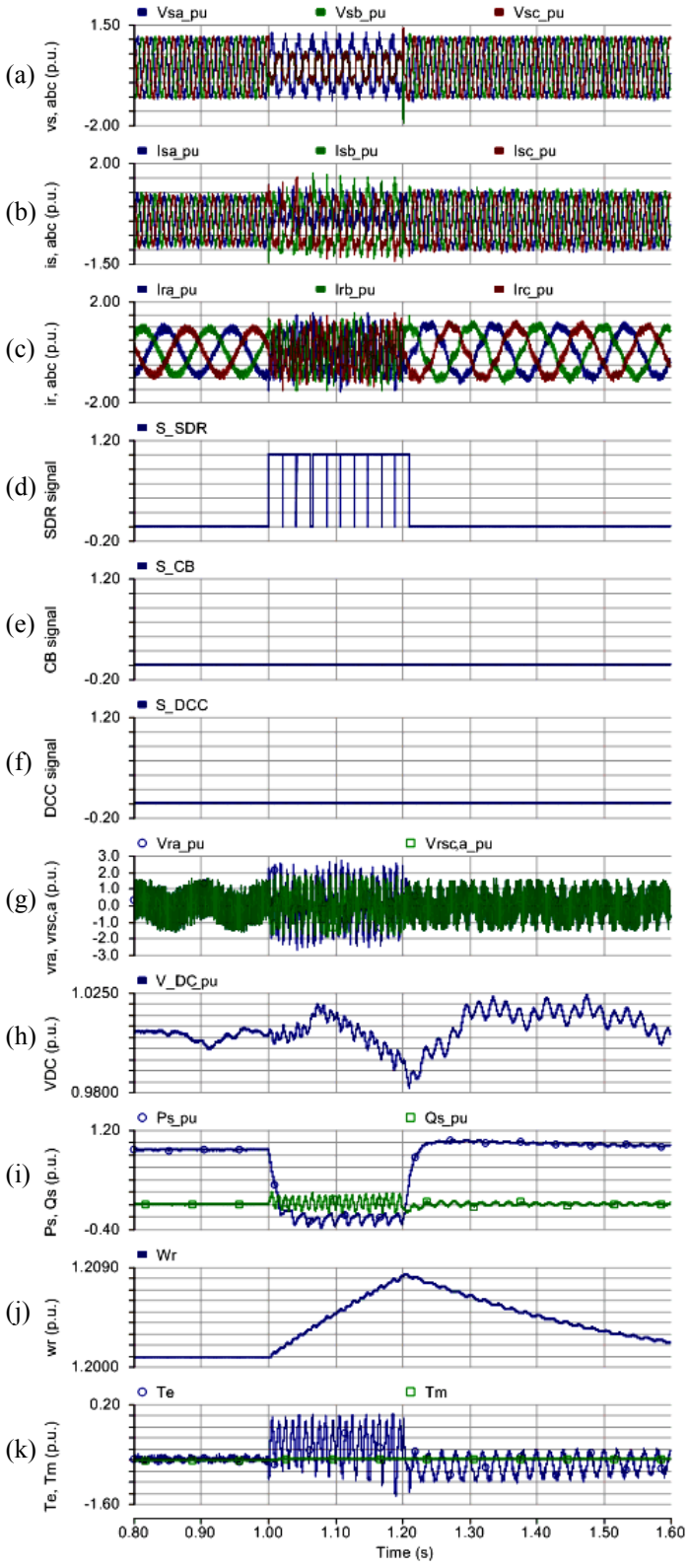

Figure 2.9: Phase *b* to *c* short circuit for 0.2 s with converter protection: (a) three-phase stator voltages $v_{s\ a,b,c}$ [in per unit (p.u.)]; (b) three-phase stator currents $i_{s\ a,b,c}$ (p.u.); (c) three-phase rotor currents $i_{r\ a,b,c}$ (p.u.); (d) SDR switching signal S_{SDR}; (e) crowbar switching signal S_{CB}; (f) DC-chopper switching signal S_{DCC}; (g) phase-*a* rotor voltage v_{ra} (p.u.) and phase-*a* RSC voltage $v_{RSC,a}$ (p.u.); (h) DC-link voltage v_{DC} (p.u.); (i) stator side active power P_s (p.u.) and reactive power Q_s (p.u.); (j) rotor speed ω_r (p.u.); (k) electrical torque T_e (p.u.) and mechanical torque T_m (p.u.).

The phase *b* to *c* short-circuit in Figure 2.9, in terms of fault current, is less serious than in the single-phase case. There is no need for both crowbar and DC-chopper operation. The series dynamic resistor is effective in this condition. But in terms of stator voltage, this is more serious than for a single-phase fault. There are much larger power and electrical torque fluctuations during the fault. This results in gradual increase of rotor speed, from 1.20 p.u. to 1.21 p.u. but this is not serious.

The two asymmetrical conditions result in fluctuations after stator voltage recovery. Although most of the variables are under control, these fluctuations should be studied in more detail.

2.5.3 Performance Comparison Between Crowbar and SDR

The performance of the crowbar and the series dynamic resistor protection schemes are compared. The reactive power, electrical torque and rotor speed of the DFIG system are simulated and compared in Figure 2.10.

Both of the two strategies experience reactive power and electrical torque fluctuations during the fault. However, for crowbar protection, they are much larger. Figure 2.10(b) is expanded to show the reactive power. It can be seen that with the rotor-side converter connected with the series dynamic resistor protection scheme, no reactive power is absorbed. However, for crowbar protection, the asynchronous machine absorbs reactive power, up to 0.2 p.u. Therefore, in terms of grid voltage recovery, the series dynamic resistor protection has a significant advantage, as it doest not further contribute to voltage drop in the network due to reactive power.

The reactive power and electrical torque ripples are larger with series dynamic resistor protection compared to crowbar protection. This is due to the higher resistance in the rotor winding and DFIG control system performance during faults, which needs further exploration. However, it is clear that the peak torque that occurs at crowbar turn-on and turn-off is significantly higher than that for the series dynamic resistor. This leads to the large torque fluctuation seen in Figure 2.6 when the crowbar is engaged. For rotor speed changes they are about 0.02 p.u. different at the peak prior to recovery. The series dynamic resistor reduces the rotor overspeed more effectively than the crowbar circuit.

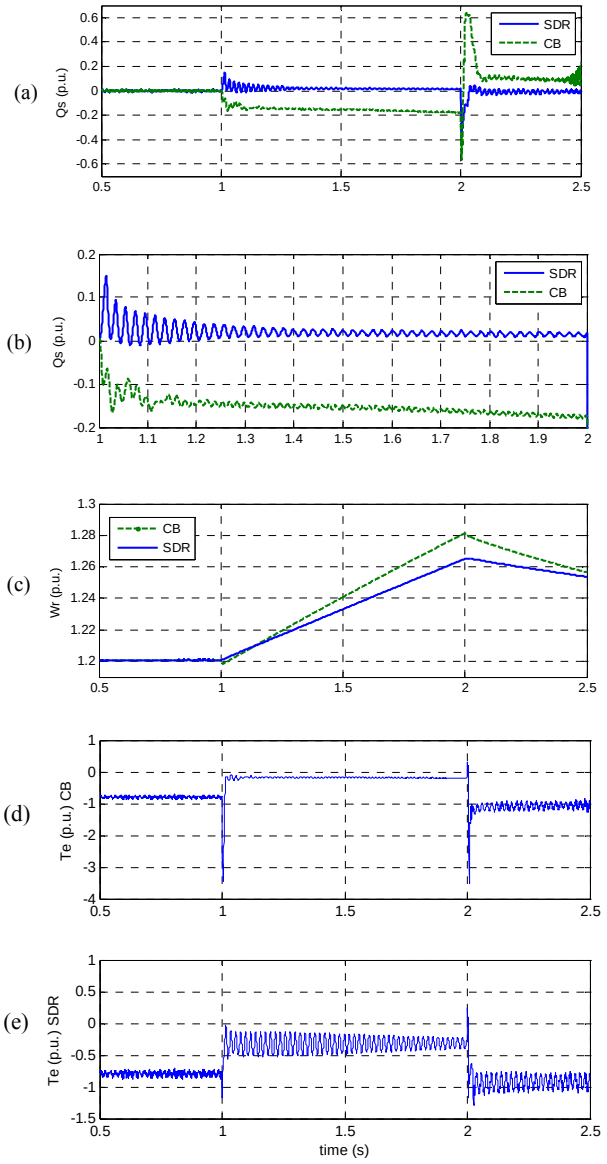

Figure 2.10: System response comparison between crowbar and series dynamic resistor protections, voltage dip of 0.6 p.u. for 2 s: (a) stator-side reactive power Q_s [in per unit (p.u.)]; (b) zoomed reactive power Q_s (p.u.); (c) rotor speed ω_r (p.u.); (d) electrical torque T_e (p.u.) with CB protection; (e) electrical torque T_e (p.u.) with SDR protection.

More importantly, the series dynamic resistor has a much smaller impact than the crowbar, especially during switching off. Improper crowbar switch-off strategy (without the coordination of controller reference setting [2.1]) can cause frequent switching which affects fault recovery. This can also be seen from the comparison of voltage recovery in Figures 2.8 and 2.9. Without crowbar switching, the voltage recovery for the two-phase short-circuit shows minimal fluctuation.

2.6 Application Discussions

2.6.1 Switch Time of the Bypass Switch

In practical applications, the switch time may be an issue, especially for serious fault protection and recovery when fast switching response is required, e.g., some crowbar thyristor switches cannot interrupt the current before zero-crossing [2.2]. This will influence the protection performance. In the above simulations, switching times of the crowbar and series-dynamic-resistor power electronic switches are considered by disabling the interpolation in PSCAD/EMTDC. This solves the conflict between immediate switching operation with simulation time step. The simulation time step is set as 20 μs, so the actual switch time for IGBT is 20 μs, which is enough for the IGBTs in applications (commonly several microseconds [2.14]).

2.6.2 Switch Normal Operation Losses

The series dynamic resistor is here realised by a power electronic switch. However, the bypass switch that is closed during normal operation will produce additional losses, specifically device *ON*-state losses. But compared to the stator side braking resistor bypass-switches [2.10], this is far lower due to the lower power rating on the rotor side.

2.7 Conclusion

Converter protection is necessary for DFIG wind power generation systems during fault conditions. In this chapter, various resistor protection schemes are reviewed. The purposes of a series dynamic resistor are: 1) to avoid the frequent use of crowbar short-circuit, 2) to maximise the operation time of the rotor-side converter, and 3) to reduce torque fluctuations during protection operation. The rotor currents during various fault conditions are discussed and current expressions are given to instruct the design of the protection scheme. Resistance calculations for the series dynamic resistor and crowbar using the expression of maximum rotor current are described.

The series dynamic resistor can operate with the rotor-side converter control functioning. For the control of the grid-side converter to DC-link bus voltage, the resumption time can be shorter than for a system with normal active crowbar protection. This is helpful for resuming normal control and provides reactive power for grid voltage support. During this process, inspection of the reactive power, electrical torque, and rotor speed fluctuations shows that the proposed method enhances DFIG fault ride-through capability. In the next chapter, the protection for another popular wind power generation system based on PMSG is investigated.

2.8 References

[2.1] J. Morren, and S.W.H. de Haan, "Ridethrough of wind turbines with doubly-fed induction generator during a voltage dip," *IEEE Trans. Energy Convers.*, vol. 20, no. 2, pp. 435-441, Jun. 2005.

[2.2] I. Erlich, J. Kretschmann, J. Fortmann, S. Mueller-Engelhardt, and H. Wrede, "Modeling of wind turbines based on doubly-fed induction generators for power system stability studies," *IEEE Trans. Power Syst.*, vol. 22, no. 3, pp. 909-919, Aug. 2007.

[2.3] D. Xiang, R. Li, P. J. Tavner, and S. Yang, "Control of a doubly fed induction generator in a wind turbine during grid fault ride-through," *IEEE Trans. Energy Convers.*, vol. 21, no. 3, pp. 652-662, Sep. 2006.

[2.4] P. S. Flannery and G. Venkataramanan, "A fault tolerant doubly fed induction generator wind turbine using a parallel grid side rectifier and series grid side converter," *IEEE Trans. Power Electron.*, vol. 23, no. 3, pp. 1126-1135, May 2008.

[2.5] J. Morren and S. W. H. de Haan, "Short-circuit current of wind turbines with doubly fed induction generator," *IEEE Trans. Energy Convers.*, vol. 22, no. 1, pp. 174-180, Mar. 2007.

[2.6] P. Zhou and Y. He, "Control strategy of an active crowbar for DFIG based wind turbine under grid voltage dips," in *Proc. Int. Conf. Electrical Machines and System. 2007*, Seoul, Korea, Oct. 8-11, 2007.

[2.7] M. Rodríguez, G. Abad, I. Sarasola, and A. Gilabert, "Crowbar control algorithms for doubly fed induction generator during voltage dips," in *Proc. 11th Eur. Conf. Power Electron. Appl.*, Dresden, Germany, Sep. 11-14, 2005.

[2.8] I. Erlich, H. Wrede, and C. Feltes, "Dynamic behavior of DFIG-based wind turbines during grid faults," in *Proc. Power Convers. Conf.*, Nagoya, Japan, Apr. 2-5, 2007.

[2.9] J. F. Conroy and R. Watson, "Low-voltage ride-through of a full converter wind turbine with permanent magnet generator," *IET Renew. Power Gener.*, vol. 1, no. 3, pp. 182-189, 2007.

[2.10] A. Causebrook, D. J. Atkinson, and A. G. Jack, "Fault ride-through of large wind farms using series dynamic braking resistors (March 2007)," *IEEE Trans. Power Syst.*, vol. 22, no. 3, pp. 966-975, Aug. 2007.

[2.11] J. López, P. Sanchis, X. Roboam, and L. Marroyo, "Dynamic behavior of the doubly fed induction generator during three-phase voltage dips," *IEEE Trans. Energy Convers.*, vol. 22, no. 3, pp. 709-717, Sep. 2007.

[2.12] M. S. Vicatos and J. A. Tegopoulos, "Transient state analysis of a doubly-fed

induction generator under three phase short circuit," *IEEE Trans. Energy Convers.*, vol. 6, no. 1, pp. 62-68, Mar. 1991.

[2.13] J. López, E. Gubía, P. Sanchis, X. Roboam, and L. Marroyo, "Wind turbines based on doubly fed induction generator under asymmetrical voltage dips," *IEEE Trans. Energy Convers.*, vol. 23, no. 1, pp. 321-330, Mar. 2008.

[2.14] S. Castagno, R. D. Curry, and E. Loree, "Analysis and comparison of a fast turn-on series IGBT stack and high-voltage-rated commercial IGBTs," *IEEE Trans. Plasma Science*, vol. 34, no. 5, pp 1692-1696, Oct. 2006.

Chapter 3

Permanent Magnet Synchronous Generator Fault Protection Schemes

3.1 Introduction

Although the doubly-fed induction generator (DFIG) is a popular wind turbine generation system due to the balance between cost and performance, as discussed in Chapter 2, a significant disadvantage of DFIG is its vulnerability to grid disturbances and fluctuations. This is especially true of its mechanically vulnerable gearbox. According to statistics of wind farm operation, 19.4% of wind turbine downtime is due to the gearbox and bearing system [3.1]. Recently, the development of larger-scale wind power generation systems has considered topologies with direct-driven permanent magnet synchronous generators (PMSGs), which do not use a gearbox, hence may be more reliable.

PMSG energy conversion systems can be classified into two categories: 1) connected to two back-to-back voltage-source converters (VSCs); 2) connected to a diode rectifier with DC/DC boost converter and a voltage-source inverter (VSI). The former is commonly considered as the technically ultimate option but is more expensive and complex. The latter is usually used in stand-alone or small-scale wind farms or micro-grids because of its simple topology and control, and most importantly, low cost. In this chapter, both topologies are considered.

Currently, PMSG system studies consider normal operation and the realisation of variable-speed maximum power point tracking. Research into system protection is limited at this stage [3.2], [3.3]. However, as fault ride-through (FRT) requirements have been proposed and there are increasing requirements for operation under harsh offshore environments, protection schemes are gradually being proposed and applied

for many wind power generation systems. The protection of wind farm devices, particularly the power electronic devices, is initially more important than staying connected to the grid.

Hence this chapter analyses the protection issues of PMSG systems and is organised as follows. In Section 3.2, the two PMSG power conversion systems and their control strategies are described. Section 3.3 introduces the options of protection schemes. PSCAD/EMTDC simulation results are provided in Section 3.4 to verify the proposed protection schemes.

The DC wind farm considered in this chapter assumes parallel-connected wind turbine generator systems. After collection from the generation systems, DC power is transmitted to the grid through DC transmission cables, a vector-controlled voltage-source inverter and a step-up transformer. The wind farm collection and transmission network protection issues will be analysed in Chapters 4 and 5. Different wind turbine converter topologies have different fault characteristics; hence only typical fault conditions are analysed for each topology.

3.2 Direct-Driven PMSG Wind Power Generation Systems

3.2.1 PMSG Power Conversion Topologies

The PMSG is used for direct-driven applications because of its simple winding structure, ease of control, and the ease of which multi-pole machines can be realised. The studied systems are: a three-phase diode rectifier with a DC/DC boost converter, and; a six-IGBT/diode bridge voltage-source converter. The basic topologies are shown in Chapter 1, Figures 1.3 and 1.4.

These generation systems have multi-pole PMSGs and fully rated power converters connecting the system to the grid. As mentioned, a direct-driven multi-pole PMSG is more reliable as it eliminates the gearbox. The fully rated power converter gives potentially improved technical performance but produces more losses in the power conversion process. Three-phase diode-rectifier and a DC/DC boost converter configuration is mainly based on low cost and simple topology [3.2], [3.3]. The diode

rectifier converts generator AC power into DC in an uncontrolled manner; therefore, power control has to be performed by the VSC connected to the grid. When the generator speed varies, the DC voltage after the diode rectifier will change. A boost converter is used to provide a smooth DC-link voltage to the inverter. The control of generator torque and speed is realised by controlling the inductor current in the boost converter. It is cheaper and the generator is decoupled from the grid by the DC-link which supplies the pulse-width modulated inverter. The aim of the grid-side VSI is to provide connection to the onshore grid with a steady DC-link voltage and adjustment of the coupling point power factor or reactive power using standard techniques.

The two topologies can be seen as a current source (boost) and a voltage source, respectively. Hence the current source converter is vulnerable to open-circuit faults and the voltage source converter is vulnerable to short-circuit faults. The system protection will be designed to cope with these most serious conditions.

The generator equations under DC short-circuit fault conditions are in terms of the stator currents in *dq* reference frame and per unit value. State variables are stator currents i_{sd}, i_{sq} and rotor speed ω_r.

$$(R_s+R)i_{sd} + (L_s + L)\frac{di_{sd}}{dt} - (L_s + L)\omega_r i_{sq} = 0 \tag{3.1}$$

$$(R_s+R)i_{sq} + (L_s + L)\frac{di_{sq}}{dt} + (L_s + L)\omega_r i_{sd} - \omega_r \Psi = 0 \tag{3.2}$$

$$\frac{d\omega_r}{dt} = \frac{1}{J}(1.5p\Psi\, i_{sq} - F\omega_r - P_m\omega_r) \tag{3.3}$$

$$P_m = C_p(\lambda, \beta)v_{wind}^3 \tag{3.4}$$

where R_s, L_s, R, and L are the generator stator winding resistance and inductance, fault point equivalent resistance and inductance, respectively. J = 2.0 p.u. is the shaft rotating inertia. p is the pole pair. Ψ = 1.0 p.u. is the constant magnet flux. F = 0.002 is the shaft friction damping factor. Wind turbine power P_m is calculated from equation (3.4). Detailed equations are referred to Chapter 1 – equation (1.3). Base values are the ratings of the generators; base wind speed is 12 ms^{-1}.

It is difficult to get an analytical solution with the complex wind turbine power expression (3.4). Hence in the following section, numerical simulation is used to demonstrate the protection schemes and their performances.

3.2.2 Control Strategy

The focus of this research is the protection scheme design and analysis. Hence a common control strategy is applied. For a large-scale system, a voltage-source converter is used for maximum power point tracking. The large-scale wind turbine has pitch-control function to reduce turbine shaft overspeed. For a small-scale system, the boost IGBT switching signal is a duty ratio, which is obtained from a PI controller that eliminates the difference between the rectified DC power and reference turbine power [3.4]. The grid-side voltage-source inverter is vector-controlled. In the synchronous speed rotating reference frame under grid voltage vector, the angle of *dq* transformation θ_e is used for decoupling control [3.5]. All the inverters in the PSCAD/EMTDC simulation use sinusoidal PWM vector control.

3.3 PMSG System Protection

The study of the HVDC transmitted wind farm protection during the grid fault has been reported [3.6]. The main protection is connecting a DC-link damping resistor to limit the DC-link overvoltage through energy dissipation. This is also analysed for a PMSG stand-alone system for protection [3.7].

Because there is no induced rotor overcurrent to limit during fault conditions, the major issue is to protect the system through DC-link energy transmission. The DC-link damping resistor method can be used in this case. One particular solution for this method in PMSG system is using one more DC/DC boost converter [3.8]. The detailed protection circuit topologies for DC-links are shown in [3.9]-[3.11]. There are mainly two types, either with a resistor to dissipate the redundant energy or incorporating an energy storage system (ESS).

In [3.12], all possible fault points have been listed for a motor system. But the consequences of these faults may be related to both generator rotor overspeed and overcurrents/overvoltages over semiconductor devices. The essence of fault ride-through of the systems is to solve the almost unchanged input energy from the turbine system during interruptions to the energy dissipation path due to faults. So it is clear to analyse the system in terms of energy transfer path.

3.3.1 Large-Scale System Protection

For large-scale systems based on voltage-source converters, the serious short-circuit fault consequences are: 1) the overcurrent along DC cable due to capacitor discharge; 2) undelivered energy resulting in wind turbine overspeed. Therefore, fast DC circuit breaker (CB) / fuse is required along with other electrical overspeed limiting methods. Basically, a dumping resistor is used to dissipate excess power during power transmission disruptions. The excess power can be dissipated in different forms of dump-load resistors, with a possible DC-chopper control to maintain the DC-link voltage; or allocated three-phase AC-side dynamic resistors. The following options are considered, shown in Figure 3.1.

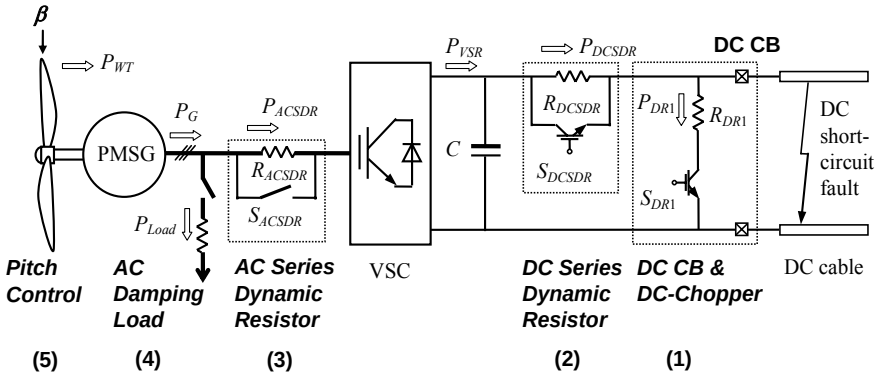

Figure 3.1: Large-scale PMSG power conversion system fault protection scheme.

1) DC CB and DC-Chopper

A DC CB is used to rapidly interrupt the DC overcurrent from the capacitor discharge. However, this will result in DC-link voltage increase. In [3.13], a braking resistor was inserted into the DC-link between the converters of DFIG; this acts as a dump load to restrain the DC-link voltage. A similar resistor was proposed in [3.14]

to enhance fault ride-through capability of PMSG. This is also used in high voltage direct current (HVDC) transmission system DC-link, called the DC-link damping resistor [3.6].

2) DC Series Dynamic Resistor

As proposed in Chapter 2 for DFIG rotor-side converter protection, a DC series dynamic resistor can also be allocated as overcurrent limiter in the DC cable or DC-link circuit to help limit the abrupt DC overcurrent. A fast solid-sate switch is used to bypass or engage the resistor during normal operation and fault conditions.

3) AC Series Dynamic Resistor

For the whole AC wind farm, a power-electronic-controlled external resistor, which is connected to the stator windings of the generator, is used to limit the rotor acceleration during a fault. This is the three-phase series resistor – called a braking resistor [3.15]. The purpose of a braking resistor is to balance the active power then improve generator stability during a fault. The advantages of a series dynamic braking resistor, when connected to the generation circuit, were studied by [3.16]. It was used to enhance the fault ride-through of a fixed speed wind turbine.

4) AC Damping Load

A three-phase AC damping load is connected at the generator terminal to help dump the redundant energy generated by the wind turbine. This is also used in traditional turbine-generator systems as an electrical braking system [3.17], [3.18].

5) Wind Turbine Pitch Control

Pitch control is widely used in large-scale wind turbines to cope with the incident wind overspeed [3.19], [3.20]. Pitch control can also be used as a method to reduce the rotor overspeed if power damping is not adequate. If the power recovery is not required to be immediate, the turbine blades can be pitched to reduce the aerodynamic torque [3.21]. Mechanical braking is usually used to hold the turbine standstill and will be used after and as a backup of the pitch-controller.

The resistance calculation is based on analysis of the redundant energy dissipation. The energy from the wind turbine should be dissipated by the protection scheme. Taking all the normal parameters as 1.0 per unit value, the resistance value should also be 1.0 p.u. in the steady-state operation of the protection circuit. For example, if the rating power of the generator is 5 MW, with a rectifier voltage of 1 kV, the resistance value is 0.8 Ω.

3.3.2 Small-Scale System Protection

For small-scale systems, there is usually no pitch control system in each wind turbine's blade. Therefore it is not included in the protection scheme below. The AC series dynamic resistor is also not included as from the above large-scale system analysis, it is similar to DC ones.

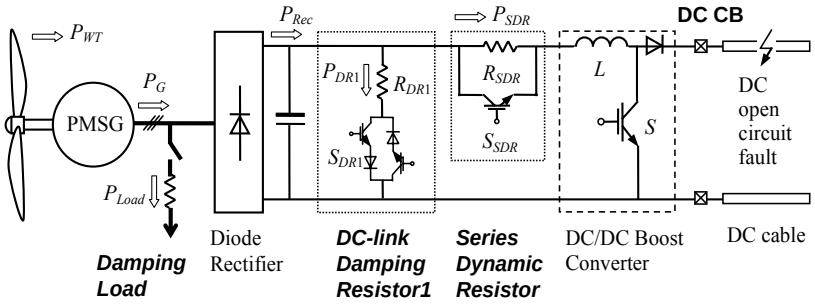

Figure 3.2: Small-scale PMSG power conversion system fault protection scheme.

1) Redundant Energy Dissipation or Storage

As in the Section 3.3.1, protection devices can be used at different links of the system [3.7], [3.9]-[3.11], [3.20]. Each DC-link connection point in the generation system can be seen as an energy balance point to analyse appropriate protection schemes. The protection options for small-scale systems are shown in Figure 3.2. The dotted blocks are the positions of the main protection schemes which can also be replaced by other specific circuit, e.g. energy storage devices.

Figure 3.3 shows the systems with VSI DC-link protection. The excess energy can be dissipated through the two DC-link damping resistors, with power of P_{DR1} and P_{DR2}, depending on the fault location. The switching signals for the two switches S_{DR1} and S_{DR2} depend on the detection of DC-link overvoltages in correspondence with a

preset threshold value. The series connected dynamic resistor R_{SDR} can be used for inductor overcurrent and sharing overvoltage for the IGBT switch *S*.

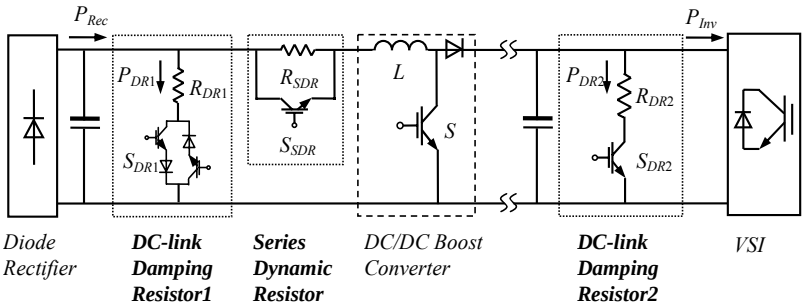

Figure 3.3: PMSG converter protection schemes.

2) Converter Protection Scheme for Open-Circuit Fault

The DC-link damping resistor across the grid-side VSI mainly copes with grid fault conditions, in which the energy cannot be transmitted through the inverter so causing DC-link overvoltage. Also, the other two resistors located in the generation system are mainly dealing with the wind farm inner fault generally resulting in the loss of connection to the collection grid and DC cables. The energy flows are discussed as follows for the two protection schemes respectively.

After disconnection from the collection grid, the energy that needs to be dissipated are from the rectifier P_{Rec} and that already stored in the inductor P_L. For the power P_{Rec}, the protection is also important to restrain the rotor overspeed. The abrupt change of real power from the generator is in relation to the generator electrical torque output. While the relatively slow mechanical dynamics of the rotor mean the mechanical torque cannot be balanced with the reduced electrical torque which results in rotor overspeed. The power P_L is mainly related to the overcurrent of the IGBT switch *S*.

If the DC-link Damping Resistor1 is engaged, there will be two power flow paths as shown in Figure 3.4. Therefore, a bi-directional switch S_{DR1} is required. Although theoretically this protection will work at the same way with a connection across the inverter DC-link capacitor, the major difference is that a small capacitor C_f is only for remedying rectifier voltage ripple instead of energy storage as is the case with capacitor *C*.

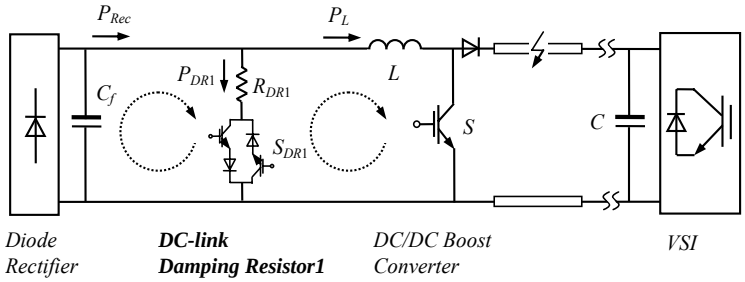

Figure 3.4: Shunt-connected damping resistor protection for cable fault condition.

The topology of the DC wind farm with parallel-connected boost converters means that all the generation systems are regarded as current sources, which means another way to dissipate excessive energy is from series connected resistors or energy storage devices. Figure 3.5 shows the power flow for a series connected resistor scheme during fault conditions. The series connection also means that not only can the inductor current be limited, the possible overvoltages across the IGBT switch *S* and the rectifier filter capacitor C_f can be shared by the resistor R_{SDR}. The energy dissipation is the same as for parallel damping, although the switch states are different.

The switch is realised by power electronic devices. With series connection, the switch needs to be connected in normal operation, the loss of which will reduce the system efficiency. Therefore it is not considered in the following simulations – only a parallel-connected damping resistor is considered.

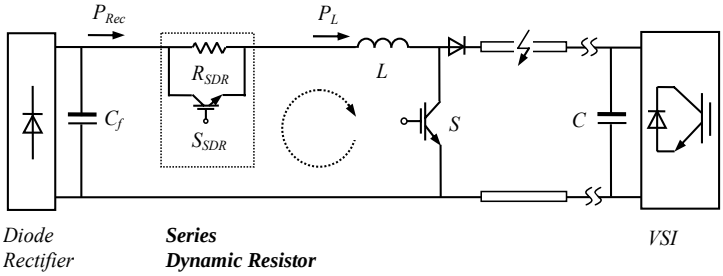

Figure 3.5: Series damping resistor protection for inner fault condition.

The resistance calculation is also based on the redundant energy dissipation. The energy from the wind turbine should be dissipated by the protection scheme. Also, the energy stored in the inductor needs to be absorbed. If the rated power of the

generator is 25 kW, with rectifier voltage of 800V, the resistance value is 25.6 Ω. There is no maximum limit for the resistance value, but a too large resistor means a big switching impact to the system when resuming normal operation after the fault clearance.

From the overcurrent analysis a switch-timing strategy is devised. For the activation of the protection resistor, there are two states:

1) Boost Switch ON State: At this stage, the inductor is being charged by the rectifier. The energy from the rectifier and that already stored in the inductor can be dissipated via the resistor and boost switch.

2) Boost Switch OFF State: The energy from the rectifier and the inductor cannot be released from the diode to the inverter. So it is mainly the power from rectifier being absorbed by the damping resistor.

Hysteresis control is used to control the rectifier voltage within a preset hysteresis band. In the following simulation, the band is set at 0.1 p.u, as will be shown in Figure 3.10(d). The inverter DC-link damping resistor switching is also included.

3.4 Simulation Results

The proposed protection method of the specific DC wind farm system are analysed by PSCAD/EMTDC simulations. The simulation DC wind farm system includes two equivalent parallel-connected wind turbine generation systems. The generator and cable parameters are listed in Tables 3.1 and 3.2, respectively.

Table 3.1: PMSG Parameters

Parameter	Value	Parameter	Value
Rated power P_n	25 kW (small-scale)	Rated power P_n	5 MW (large-scale)
Rated stator voltage V_{sn}	450 V (small-scale)	Phase resistance	0.068 p.u. (both large- and small-scale)
Rated stator voltage V_{sn}	800 V (large-scale)	Phase inductance	0.427 p.u. (both large- and small-scale)

Table 3.2: Large-Scale System Cable Parameters

Parameter	Value	Parameter	Value
Resistance *r*	0.06 Ω/km	Cable length	100 m
Inductance *l*	0.28 mH/km	DC-link capacitor	10 mF
Rating voltage	2 kV		

3.4.1 Large-Scale System Fault Condition

Figure 3.6 shows the system response to a cable short-circuit fault without and with different electrical braking system protections. The fault simulated is a permanent fault. Without any protection, the cable overcurrent reaches 10 times of the normal value, in Figure 3.6(a). The DC-link voltage falls to around zero rapidly. Generator stator current increases up to 2.0 p.u. Moreover, the rotor speed ramps up to over 1.5 p.u. within 3 s, which is a heavy burden for the mechanical system.

With a fast DC CB to interrupt overcurrent above 1.5 p.u. [in Figure 3.6(b)], the generator energy will store in the DC-link capacitor and hence there is an increase in the DC-link voltage. However, this is not over the 1.1 p.u. limit (2.2 kV) in Figure 3.6(b) until 2.7 s. Then the hystersis control of DC-chopper starts damping energy via the parallel-connected resistor. The rotor overspeed then begins to decrease. Without the DC CB, only using DC series dynamic resistor to limit the stator overcurrent and damping the redundant energy, the rotor overspeed is reduced better in Figure 3.6(c). The AC series dynamic resistor has a similar effect in reducing the overspeed. However, the AC switch is slow (in terms of 10 ms). This will not avoid the first overcurrent wave front of stator current in Figure 3.6(d). A damping load in line with AC CB (also operates in 10 ms) will almost eliminate the overspeed caused by power unbalance, but it has no effect on the overcurrent, as shown in Figure 3.6(e).

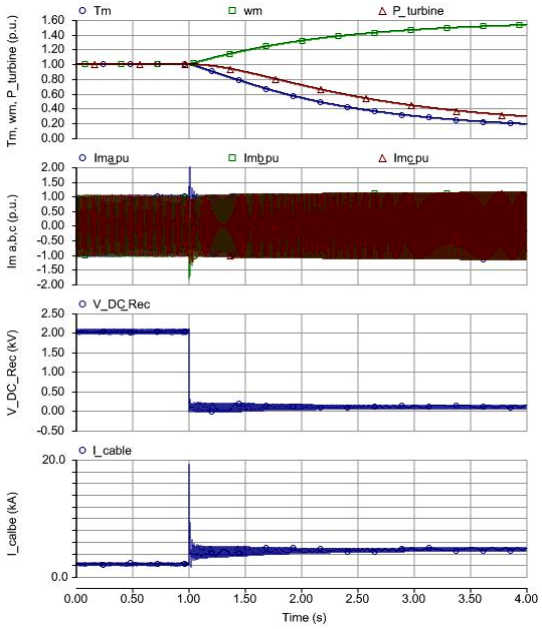
Tm
wm
P_turbine
Tm, wm, P_turbine (p.u.)
Ima.pu
Imb.pu
Imc.pu
Im a,b,c (p.u.)
V_DC_Rec
V_DC_Rec (kV)
I_cable
I_calbe (kA)
Time (s)

(a)

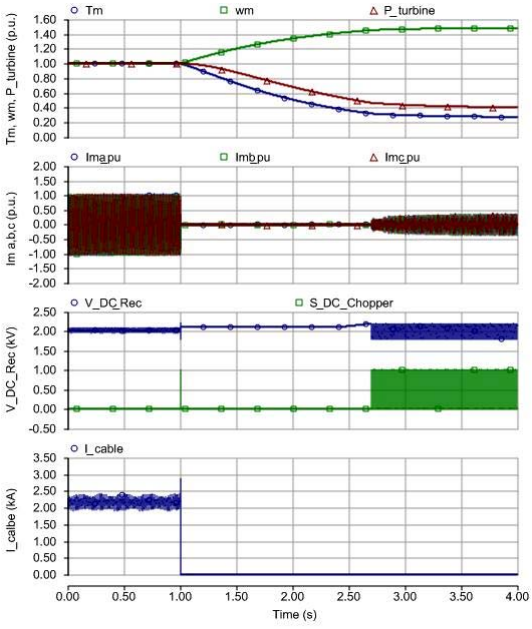
Tm
wm
P_turbine
Tm, wm, P_turbine (p.u.)
Ima.pu
Imb.pu
Imc.pu
Im a,b,c (p.u.)
V_DC_Rec
S_DC_Chopper
V_DC_Rec (kV)
I_cable
I_calbe (kA)
Time (s)

(b)

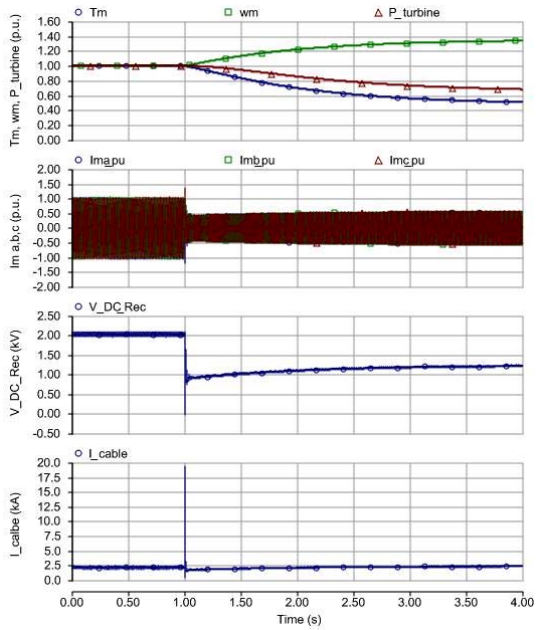
Tm
wm
P_turbine
Tm, wm, P_turbine (p.u.)
Ima.pu
Imb.pu
Imc.pu
Im a,b,c (p.u.)
V_DC_Rec
V_DC_Rec (kV)
I_cable
I_calbe (kA)
Time (s)

(c)

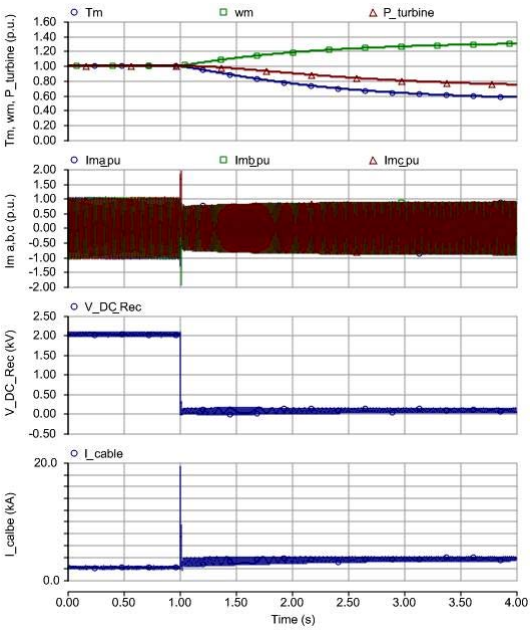
Tm
wm
P_turbine
Tm, wm, P_turbine (p.u.)
Ima.pu
Imb.pu
Imc.pu
Im a,b,c (p.u.)
V_DC_Rec
V_DC_Rec (kV)
I_cable
I_calbe (kA)
Time (s)

(d)

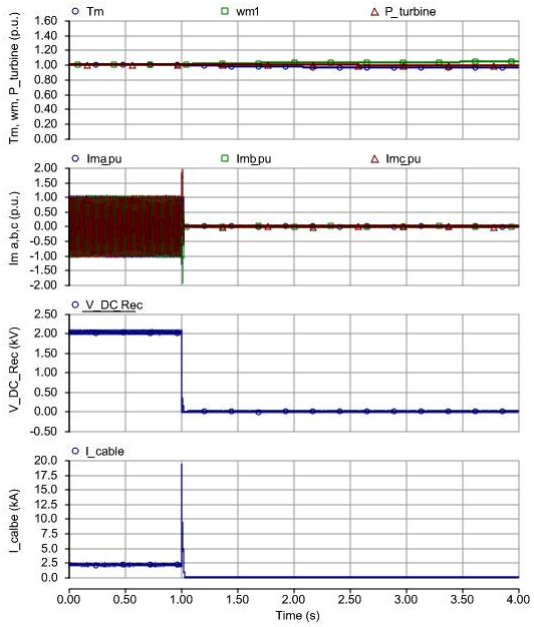

(e)

Figure 3.6: Comparison of electrical protection methods during fault conditions (occurring at 1.0 s): (a) without protection; (b) with DC CB and DC-chopper protection; (c) with DC series dynamic resistor; (d) with three-phase AC series dynamic resistor; (e) with AC damping load.

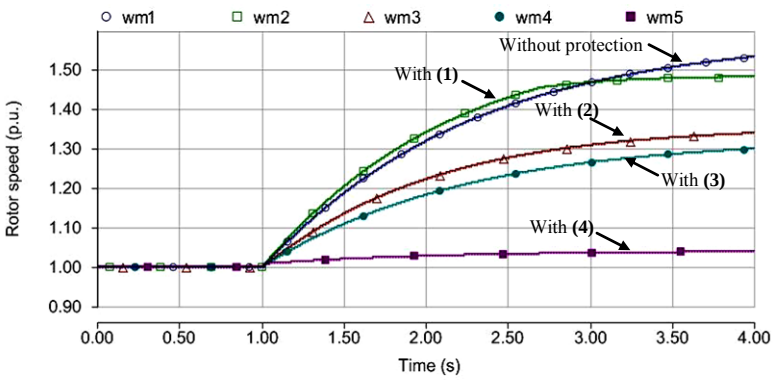

Figure 3.7: Comparison of rotor speed limiting effect with different protections shown in Figure 3.1.

The effect of overspeed limiting under different protections is compared in Figure 3.7. From the simulation results, it is noted that all the damping resistor methods are good at reducing rotor overspeed to be around or below the 1.3 p.u. limit [with protections of (2), (3), and (4) in Figure 3.7]. However, DC CB with DC-chopper protection is required in reducing the cable overcurrent like that in Figure 3.6(a).

In summary, the DC CB and chopper with DC series dynamic resistor, and wind turbine pitch control are chosen to be used for the final system protection, with simulation results shown in Figure 3.8. The PI-based pitch control [3.20] is engaged when the rotor speed is above 1.2 p.u. and then reduces it to be around 1.2 p.u. This shows that the overcurrent/overvoltage and overspeed phenomenon are effectively controlled.

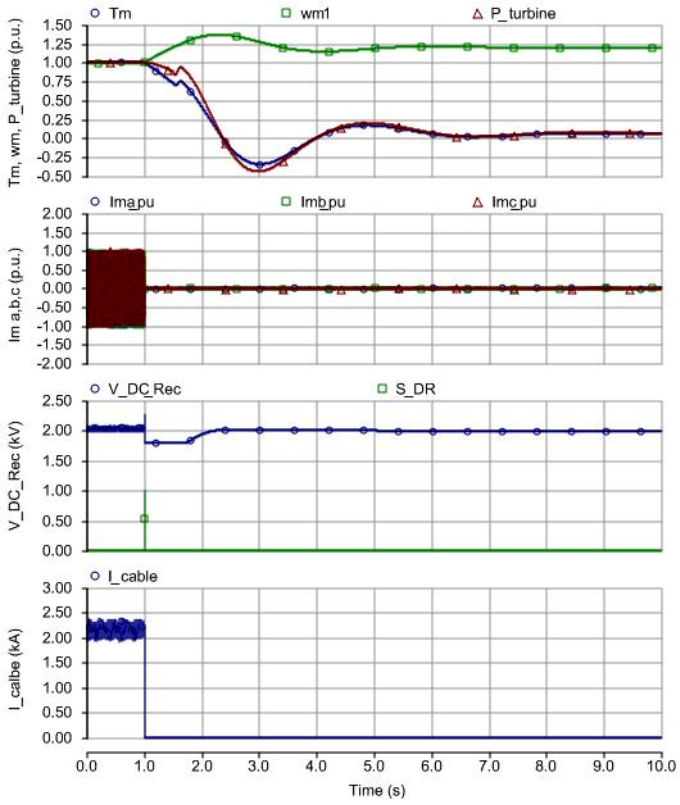

Figure 3.8: System response under DC CB, DC-chopper, and pitch control protections.

3.4.2 Small-Scale System Fault Condition

The inner open-circuit fault simulated is a loss of one connected wind turbine generation system for 1.0 s. As described above, the rectifier-boost damping resistor and inverter DC-link damping resistor are used for system protection. The system performances including the interested variables of the two parallel generation systems: rotor speeds, electrical torques, wind farm total active and reactive power, rectifier and inverter voltages, boost DC currents, duty ratios, without and with protection are shown in Figures 3.9 and 3.10 respectively.

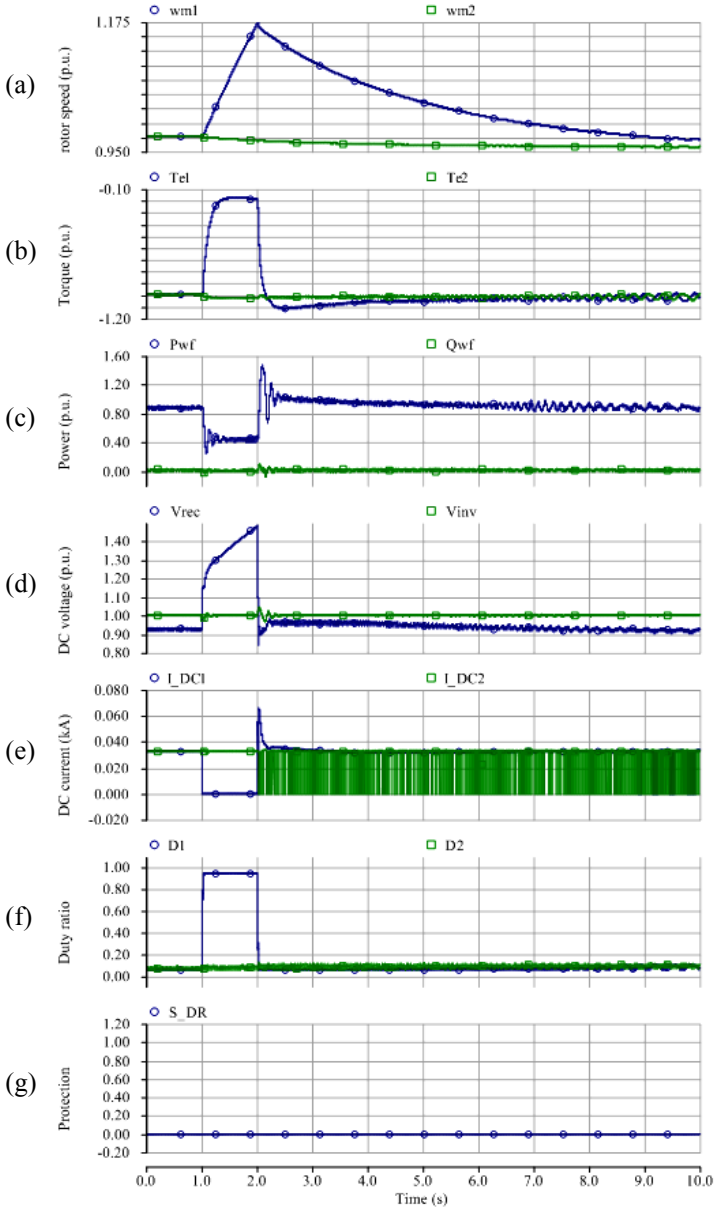

Figure 3.9: Without protection, one wind turbine generation system connection loss for 1.0 s: (a) rotor speed (p.u.); (b) generator torque (p.u.); (c) wind farm active and reactive power (p.u.); (d) rectifier and inverter DC voltages (p.u.); (e) DC currents (p.u.); (f) boost duty cycle; (g) DC-chopper signal.

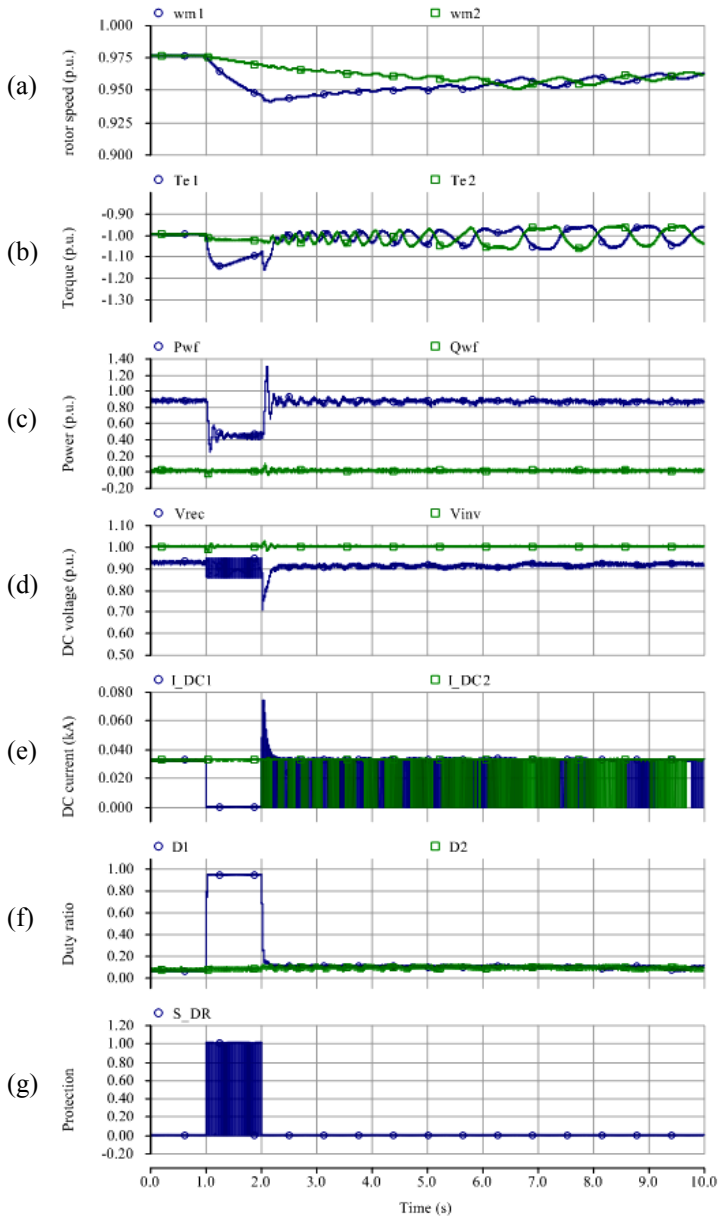

Figure 3.10: With protection, one wind turbine generation system connection loss for 1.0 s: (a) rotor speed (p.u.); (b) generator torque (p.u.); (c) wind farm active and reactive power (p.u.); (d) rectifier and inverter DC voltages (p.u.); (e) DC currents (p.u.); (f) boost duty cycle; (g) DC-chopper signal.

Without protection, the rotor speed of the first generator will accelerate rapidly as shown in Figure 3.9(a), up to 1.175 p.u. at the end of the fault. The torque of the faulted generator drops rapidly. Hence the total power from the wind farm decreases to a half of its original value, with overshoot of over 1.5 p.u. at the clearance point of the fault. Another big impact is the rectifier overvoltage, up to 1.5 p.u., during the

fault duration, which could damage the rectifier diodes. The recovery of the whole system displays an oscillation whose amplitude rises slightly with a reducing frequency. The influence of the fault on the inverter DC-link voltage is marginal, within a band of 0.1 p.u. Therefore there is no need to switch in the inverter DC-link damping resistor for protection which is why its switching signal is not shown.

With protection, the most critical values of system rotor speed and rectifier overvoltage are effectively restrained. The active power overshoot at the fault clearance point decreases to 1.3 p.u. The power absorbed by the damping resistor can balance the input wind turbine power and hence limit the faulted generator rotor speed around the value before fault, about 1.0 p.u. Rectifier voltage fluctuates within the given hysteresis band. The whole system also experiences oscillations during the recovery with a lower frequency than without protection. However, long term simulations show that with protection, this oscillation is attenuated faster than the system without protection, although with lower frequency shown in Figure 3.10 (with protection) than in Figure 3.9 (without protection).

The fluctuations are characterised by rotor speeds of the two generation systems. When their speeds converge, the fluctuation reaches its heaviest point with biggest amplitude. That means with protection, the process of fluctuation damping will be faster, because the rotor speed difference is reduced by the protection scheme, from 0.175 p.u. to less than 0.05 p.u.

The oscillations during fault recovery are an interaction between the two boost-based generation systems. Further work should be performed to understand this problem. However it is predicted that the fluctuation is not serious, with total power fluctuation of only about 0.05 to 0.1 p.u. If there are more paralleled-connected systems, the situation may or may not be more complex, but may not be as a serious influence compared to the impact of the fault on the wind farm.

The system performance and related protection schemes for other DC fault conditions should also be analysed. The work reported in this chapter can be combined with other protection devices such as mechanical braking devices. However, the need to absorb excess energy cannot be avoided in this system during

fault conditions when the major problem is the interruption of the energy flow paths. The proposed open-circuit fault protection scheme can also be used for ground faults or short-circuit faults. With the operations of switchgear, these common faults will result in the open-circuit status.

3.5 Conclusion

The proposed protection schemes for the direct-driven PMSG-based systems are aimed at protecting wind farm devices and enhancing the fault ride-through capability for grid connection. The proposed series and shunt damping resistors (AC or DC), in the back-to-back voltage-source converter-based systems for large-scale wind farms, and the current-source converter based systems (diode rectifier – boost circuits) for small-scale or stand-alone wind farms are used for DC fault protection. Both the large-scale and small-scale PMSG system protection schemes are investigated with PSCAD/EMTDC simulations. Wind turbine blade-pitch control is included in the large-scale system simulations for the purpose of limiting rotor overspeed. For the small-scale parallel-connected wind farm, the normal voltage-source inverter DC-link chopper protection is also included. The proposed protection schemes can increase the protective flexibility and effectively protect the system, especially for inner wind farm electrical fault conditions.

3.6 References

[3.1] J. Ribrant and L. M. Bertling, "Survey of failures in wind power systems with focus on Swedish wind power plants during 1997–2005," *IEEE Trans. on Energy Convers.*, vol. 22, no. 1, pp. 167-173, Mar. 2007.

[3.2] J. M. Carrasco, E. Galván, R. Portillo, L.G. Franquelo, and J.T. Bialasiewicz, "Power electronic systems for the grid integration of wind turbines," in *Proc. 32nd Annual Conf. IEEE Industrial Electronics – IECON 2006*, pp. 4182-4188, Nov. 2006.

[3.3] J. A. Baroudi, V. Dinavahi, and A. M. Knight, "A review of power converter topologies for wind generators," *Renewable Energy*, published online in Wiley Interscience, Jan. 19, 2007.

[3.4] S. M. Muyeen, R. Takahashi, T. Murata, and J. Tamura, "Transient stability enhancement of variable speed wind turbine driven PMSG with rectifier-boost converter-inverter," in *Proc. 18th International Conf. on Electrical Machines*, 6-9 Sep. 2008.

[3.5] M. G. Molina and P. E. Mercado, "A new control strategy of variable speed wind turbine generator for three-phase grid-connected applications," *Proc. IEEE/PES Transmission and Distribution Conf. and Exposition*, 13-15 Aug. 2008.

[3.6] L. Xu, L. Yao, M. Bazargan, and A. Yan, "Fault ride through of large offshore wind farms using HVDC transmission," in *Proc. IEEE Power Tech Conf.*, 28 Jun – 2 Jul, 2009, Bucharest, Romania.

[3.7] M. E. Haque, M. Negnevitsky, and K. M. Muttaqi, "A novel control strategy for a variable speed wind turbine with a permanent magnet synchronous generator," *Proc. Industry Applications Society Annual Meeting*, 5-9 Oct. 2008.

[3.8] N. P. W. Strachan and D. Jovcic, "Dynamic modelling, simulation and analysis of an offshore variable-speed directly-driven permanent-magnet Wind Energy Conversion and Storage System (WECSS)," *Europe OCEANS*, June 18-21, 2007.

[3.9] C. Abbey, W. Li, L. Owatta, and G. Joós, "Power electronic converter control techniques for improved low voltage ride through performance in WTGs," *Proc. 37th IEEE Power Electronics Specialists Conference*, June 18-22, 2006.

[3.10] C. Abbey and G. Joós, "Effect of low voltage ride through (LVRT) characteristic on voltage stability," *Proc. of IEEE Power Engineering Society* General *Meeting*, Jun. 12-16, 2005, 1901-1907.

[3.11] J. Morneau, C. Abbey and G. Joós, "Effect of low voltage ride through technologies on wind farm," *IEEE Canada Electrical Power Conference*, Oct. 25-26, 2007, 56-61.

[3.12] D. Kastha and B. K. Bose, "Investigation of fault modes of voltage-fed inverter

system for induction motor drive," *IEEE Trans. Industrial Appl.,* vol. 30, no. 4, pp. 1028-1038, July/August 1994.

[3.13] I. Erlich, J. Kretschmann, J. Fortmann, S. Mueller-Engelhardt, and H. Wrede, "Modeling of wind turbines based on doubly-fed induction generators for power system stability studies," *IEEE Trans. Power Syst.*, vol. 22, no. 3, pp. 909-919, Aug. 2007.

[3.14] J. F. Conroy and R. Watson, "Low-voltage ride-through of a full converter wind turbine with permanent magnet generator," *IET Renew. Power Gener.*, vol. 1, no. 3, pp. 182-189, 2007.

[3.15] W. Freitas, A. Morelato, and W. Xu, "Improvement of induction generator stability using braking resistors," *IEEE Trans. Power Syst.*, vol. 19, no. 2, pp. 1247-1249, May 2004.

[3.16] A. Causebrook, D. J. Atkinson, and A. G. Jack, "Fault ride-through of large wind farms using series dynamic braking resistors (March 2007)," *IEEE Trans. Power Syst*., vol. 22, no. 3, pp. 966-975, Aug. 2007.

[3.17] K. Rajambal, B. Umamaheswari, and C. Chellamuthu, "Electrical braking of large wind turbines," *Renewable Energy*, vol. 30, pp. 2235-2245, 2005.

[3.18] L. M. Craig, Z. Saad-Saoud, and N. Jenkins, "Electrodyamic braking of wind turbines," *IEE Proc.-Electr. Power Appl.*, vol. 145, no. 2, pp. 140-146, Mar. 1998.

[3.19] E. Muljadi and C. P. Butterfield, "Pitch-controlled variable-speed wind turbine generation," *IEEE Trans. Ind. Appl.*, vol. 37, no. 1, pp. 240-246, Jan./Feb. 2001.

[3.20] H. Geng and G. Yang, "Output power control for variable-speed variable-pitch wind generation systems," *IEEE Trans. Energy Convers.*, vol. 25, no. 2, pp. 494-503, Jun. 2010.

[3.21] R. Ottersten, A. Petersson, and K. Pietilainen, "Voltage sag response of PWM rectifiers for variable-speed wind turbines," *Nordic Workshop on Power and Industrial Electronics*, 2004.

Chapter 4

Internal Fault Analysis and Protection of Multi-terminal DC Wind Farm Collection Grids

4.1 Introduction

Multi-terminal DC wind farm topologies are attracting increasing research effort. For grid connection of wind farms, the topology uses high-voltage direct-current transmission based on voltage-source converters (VSC-HVDC) [4.1]. With AC/DC converters on the generator side, this topology can be developed into a multi-terminal DC network for wind power collection, which is especially suitable for large-scale offshore wind farms due to advantages such as no requirement for generator synchronisation, fully rated VSCs being capable of tracking wind turbine maximum power point, DC transmission to avoid the AC transmission distance limitations for distant offshore wind farms, and system efficiency enhancement [4.2]–[4.4].

Traditional HVDC systems are robust to DC short circuits as they are current regulated with a large smoothing reactance connected in series with cables. Therefore, they do not suffer from overcurrents due to DC cable faults and there is no overcurrent to react to. Hence, HVDC protection mainly relies on DC voltage change detection [4.5]. Research on HVDC system protection is mainly focused on specific cable fault-locating approaches [4.6], [4.7], including the application of travelling-wave detection methods [4.8]. However, the HVDC protection method is not applicable for VSC-based multi-terminal DC systems.

Voltage-source conversion techniques are commonly used for AC/DC or DC/AC power conversion. Ideally, in a DC wind farm, each conversion element can be a voltage source, because of its flexible control of both active power and reactive

power. VSC controllability can cope with grid-side AC disturbances, during which appropriate control and protection methods can be used to protect its power electronic devices [4.9], [4.10]. But due to the overcurrents flowing through freewheel diodes, it is defenceless against DC-side faults, for example, DC-link short circuits, DC cable short circuits, and DC cable ground faults. Among them, the DC-side short-circuit fault is the most serious and special protections are required to tackle this critical situation. Therefore, the DC switchgear configuration and VSC protection systems need to be properly designed and allocated.

There have been discussions about the influence of DC faults on DC distribution systems and possible protection solutions. The methods include switchgear allocation, a metal-oxide varistor (MOV) connected across diodes to protect them from overvoltage, or replacing diodes with controllable gate power electronic devices [4.11], [4.12]. DC-link capacitor overcurrent protection is also analysed [4.13]. Generally, the most serious DC short-circuit fault occurs at the DC rails. However, no research about the DC cable-connected VSCs has been reported, in which a cable short-circuit fault is potentially more common than a DC rail fault and the impact of a DC fault on the freewheel diodes in the VSC can be worse than that of a direct DC rail short circuit due to the inductive component in the discharge path. Although the underground cables are seldom short-circuited compared to overhead lines, it is a critical condition and needs to be analysed, particularly for switchgear relay and protection design. The method of transmission-level meshed VSC-HVDC system fault detection and location is discussed in [4.14] and [4.15]. An economic solution using AC-side circuit breakers (CBs) coordinating with DC fast switches (which are only used for physical isolation instead of arc extinguishing) is proposed with a "hand-shaking" coordination approach. No detailed fault overcurrent is analysed. Moreover, AC-side switchgear is apparently not fast enough to cope with the rapid rise of fault current characteristic of freewheel diode conduction which can damage power electronic devices in several milliseconds. The basic "cut-and-try" method is not enough for system reliability enhancement.

In this chapter, DC cable faults, with the cable connected to a VSC, are discussed to assess the challenges and help solve this problem. Radial collection and transmission system for a wind farm is considered. A method without switchgear configuration is

proposed for small-scale DC wind farms to provide an economic option. However, for large-scale offshore DC wind farms with HVDC power transmission, the DC switchgear configuration is indispensable.

The chapter is organised as follows. In Section 4.2, the multi-terminal DC wind farm topology background is introduced with potential options. Then, possible internal DC faults are analysed according to type and characteristic. Fault overcurrent expressions are given in detail. Under this characteristic analysis, fault detection and detailed protection methods are proposed in Section 4.4. Theoretical analysis and PSCAD/EMTDC simulations are provided in Sections 4.3–4.5.

4.2 Multi-terminal DC Wind Farm

4.2.1 Multi-terminal DC Wind Farm Topology

The multi-terminal DC wind farm topology is still a matter of research and discussion. Current limitations of DC transmission include the lack of operational experience, the high cost of DC CBs and the lag in development of DC devices for high-power applications. However, DC transmission is still an economic technique for distant (e.g., hundreds of kilometres) large-scale offshore wind farms. Traditional solutions of AC wind farm collection grids use either AC or DC transmission cables [4.1]. AC distribution and transmission are a commonly used topology, with mature technologies. These days, favoured DC wind farm topologies can be classified in terms of the number and positions of voltage-level transform (step-up DC/DC, or AC/DC) and detailed converter topologies. No discussions about two other aspects are evident: 1) whether radial or loop connected; 2) whether each DC cluster is in star or string connection as in the traditional AC wind farm scenario. In this chapter, star and string connections are considered. The meshed connection could be promising for HVDC transmission level in the future, which will be discussed in the next chapter.

The illustration of star- or string-connected DC wind farms is shown in Figure 4.1. Each wind turbine-generator unit is connected with an AC/DC converter and

connected to the DC system through cables. Thereafter, power is transferred to the onshore grid through a voltage-source inverter (VSI) and step-up transformer. The DC voltage level is stepped-up with a centralised DC/DC transfer converter, which is discussed in [4.2] to be the optimal option for DC wind farms. DC cable grounding capacitances are only considered for long transmission cables where they can be incorporated into the DC-link capacitors at either end. DC collection cable grounding capacitances are omitted because of the low collection voltage level. Therefore, the cables are represented by series *RL* impedance. Figure 4.1 shows the possible DC switchgear configuration as well.

4.2.2 DC Distribution System Fault Protection

DC distribution fault protection issues of a stand-alone Navy shipboard power system were discussed in [4.12]. The system characteristic is different than that of the wind farm collection grid, mainly in the power sources and power-flow direction. Traditional DC distribution can have generators of its own but is generally a load on the network. A DC wind farm is a power source; however, under DC fault conditions, it will absorb power from the grid. References [4.14] and [4.15] study a fault locating and isolation method for a general multi-VSC-based DC system; this is mainly based on AC-side CBs, and no DC switchgear configuration is discussed due to cost considerations.

For star connection, each turbine-generator-converter unit has its own collection cable and switchgear that connect to a DC bus. Whereas for string connection, the turbine-generator sets are connected together with similar cable lengths. In this case, the collection cable rating can change along the string as transmitted power increases. The sectionalised switchgear shown in Figure 4.1(b) is usually not used in reality. Normally, each string has only one switchgear: the whole string has to be tripped if a fault occurs. To enhance the reliability, sectionalised switchgear positions are shown here. They are not only for fault isolation, but also for maintenance to enhance the wind farm availability even under maintenance.

In this case, the connection can be seen as each individual wind turbine-generator-cable sections (collection grid unit, shown in Figure 4.1 (a) and (b)

in the dotted areas), DC bus and transmission system with VSI, as shown in Figure 4.2. Hence the analysis can be used for both connections as different combinations of these standard components.

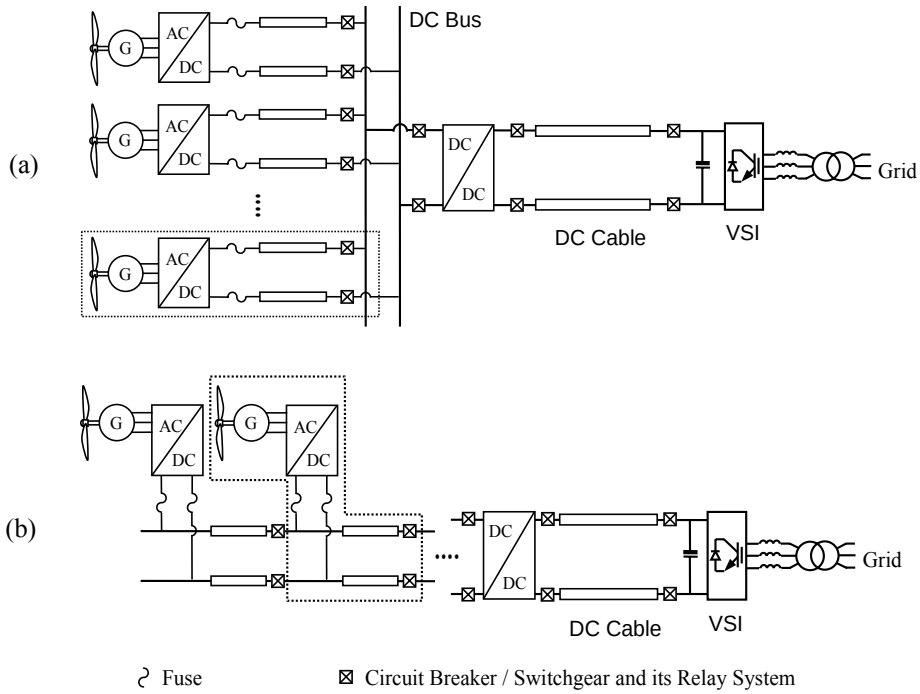

Figure 4.1: DC wind farm topology with switchgear configuration: (a) star collection; (b) string collection.

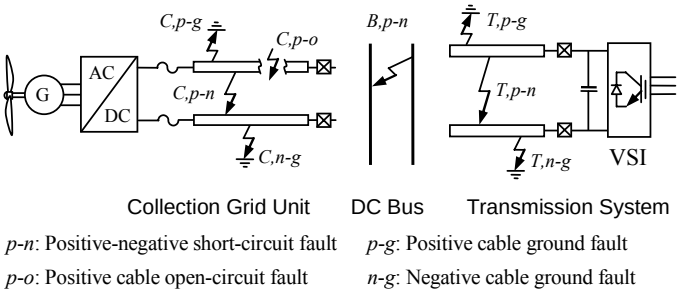

Figure 4.2: Locations and types of DC wind farm internal faults.

4.3 DC Fault Types and Characteristics

The DC faults that may occur with wind farms can be classified into different levels: 1) the wind turbine generation system level, 2) the connection grid level, and 3) the transmission level. For different devices, they can also be sorted as: inner-converter faults, DC cable faults, and junction faults (i.e., at the DC bus).

Wind power generation systems may have different topologies and the power-electronic-building-block has its own protections, such as detailed doubly-fed induction generator (DFIG) protection [4.16], [4.17] and permanent magnet synchronous generator (PMSG) protection [4.18], [4.19]. Internal faults inside the converter, such as insulated-gate bipolar transistor (IGBT) shoot-through and short-circuit across the DC rails, are typically managed by the VSC control system [4.12] and are less frequent than external faults on the cables or terminals that are exposed to the environment. Hence, the protection of VSC internal faults is not included in this chapter, which can also be solved using the traditional differential protection method [4.5] or that of HVDC systems [4.20]. Therefore, this chapter will focus on the collection grid and transmission system faults, which are shown in Figure 4.2. Cable faults occur frequently because of the insulation deterioration and breakdown. The causes include: physical damage, environmental dampness, electrical stresses, cable aging, etc [4.21]. Here, the characteristics of the DC fault current are analysed for a number of faults on the DC cables that connect the power sources to the VSI.

4.3.1 VSI DC Short-Circuit Fault Overcurrent

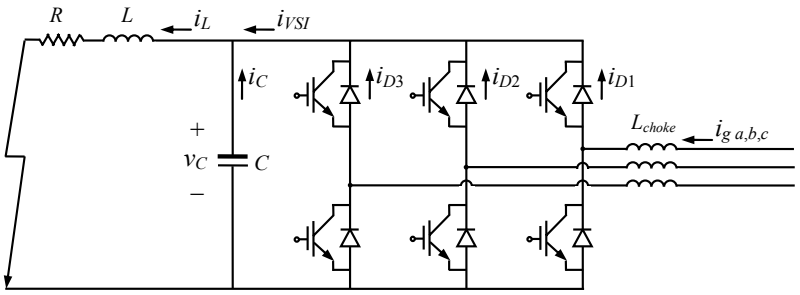

Figure 4.3: VSI with a cable short-circuit fault condition.

A DC short-circuit fault is the most serious condition for the VSI. The IGBTs can be blocked for self-protection during faults, leaving reverse diodes exposed to overcurrent. For the fault shown in Figure 4.2, regardless of where the DC short circuit fault occurs, it can be represented by an equivalent circuit shown in Figure 4.3, where R and L are the equivalent resistance and inductance of the cable from the VSI to the cable short-circuit point. To solve the complete response of this nonlinear

circuit, different time periods are analysed individually. Expressions for the DC-link voltage and diode overcurrent are derived.

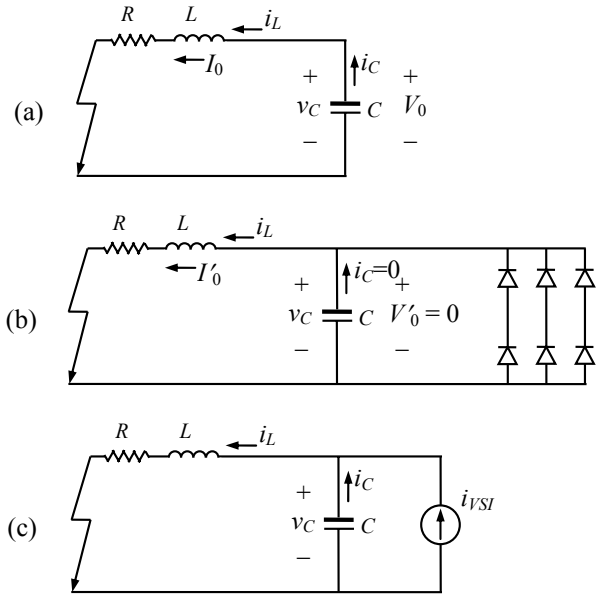

Figure 4.4: Equivalent circuit with VSI as a current source during cable short-circuit fault: (a) immediately after the fault (capacitor discharging phase); (b) diode freewheel phase; (c) grid current-fed phase.

1) Immediately After the Fault (Natural Response):

This is the DC-link capacitor discharging phase as shown in Figure 4.4(a). Under the condition of $R < 2\sqrt{L/C}$, the solution of the second-order circuit natural response gives an oscillation. Assume the fault occurs at time t_0, the natural response (without inverter-side current i_{VSI}) under the initial conditions of $v_C(t_0) = V_0$, $i_L(t_0) = I_0$ is

$$v_C = \frac{V_0\omega_0}{\omega} e^{-\delta t} \sin(\omega t + \beta) - \frac{I_0}{\omega C} e^{-\delta t} \sin \omega t \tag{4.1}$$

$$i_L = C\frac{dv_C}{dt} = -\frac{I_0\omega_0}{\omega} e^{-\delta t} \sin(\omega t - \beta) + \frac{V_0}{\omega L} e^{-\delta t} \sin \omega t \tag{4.2}$$

where $\delta = \frac{R}{2L}$, $\omega^2 = \frac{1}{LC} - \left(\frac{R}{2L}\right)^2$, $\omega_0 = \sqrt{\delta^2 + \omega^2}$, and $\beta = \arctan\frac{\omega}{\delta}$.

The time when the capacitor voltage drops to zero is

$$t_1 = t_0 + (\pi - \gamma)/\omega \tag{4.3}$$

where $\gamma = \arctan\left[(V_0\omega_0 C\sin\beta)/(V_0\omega_0 C\cos\beta - I_0)\right]$.

2) Diode Freewheel Stage (After $v_C = 0$, Natural Response):

This is the cable inductor discharging phase which is solved using the first-order equivalent circuit [Figure 4.4(b)], where the inductor current circulates in the VSI freewheel diodes. The inductor current has an initial value $i_L(t_1) = I'_0$. The expression of inductor discharge current, where each phase-leg freewheel diode current carries a third of the current, is

$$i_L = I'_0\, e^{-(R/L)t},\ i_{D1} = i_L / 3. \tag{4.4}$$

This is the most challenging phase for VSI freewheel diodes, because the freewheel overcurrent is very abrupt with a high initial value, which can immediately damage the diodes.

3) Grid-Side Current Feeding Stage (Forced Response):

This is the DC-link capacitor and cable inductor under a forced current source response (with i_{VSI} when the VSI control blocked, v_C is not necessarily zero) [Figure 4.4(c)]. To calculate the fault current contribution from the inverter, a three-phase short-circuit current expression is obtained by three-phase short-circuit analysis. For phase *a*, assume the grid voltage after fault occurs is $v_{ga} = V_g\sin(\omega_s t + \alpha)$, with V_g as the amplitude, ω_s as the synchronous angular frequency, phase-*a* voltage angle α at t_1, the phase current is

$$i_{ga} = I_g\sin(\omega_s t + \alpha - \varphi) + [I_{g|0|}\sin(\alpha - \varphi_0) - I_g\sin(\alpha - \varphi)]e^{-t/\tau} \tag{4.5}$$

where $\varphi = \arctan\left(\omega_s(L_{choke} + L)/R\right)$, $\tau = (L_{choke} + L)/R$, $I_{g|0|}$ and φ_0 are the initial grid current amplitude and phase angle, L_{choke} is the grid-side choke inductance.

The positive i_{ga} current flows from diode D_1 to contribute to the i_{VSI}, with those of i_{gb} and i_{gc}, so the total i_{VSI} is the positive three-phase short-circuit current summation

$$i_{VSI} = i_{D1} + i_{D2} + i_{D3} = i_{ga,(>0)} + i_{gb,(>0)} + i_{gc,(>0)}. \tag{4.6}$$

Here, the phase-*a* part $i_{ga,(>0)}$ response is analysed, which is chosen to be the most serious one (with grid voltage phase angle zero at the fault initiation). Phases *b* and *c* can be superimposed afterwards. The inductor currents are solved as

$$i_L = A\sin(\omega_s t + \gamma) + Be^{-t/\tau} + \frac{C_1\omega_0}{\omega}e^{-\delta t}\sin(\omega t + \beta) + \frac{C_2}{\omega}e^{-\delta t}\sin\omega t \tag{4.7}$$

where $A = I_g\left[(1-\omega_s^2 LC)^2 + (RC\omega_s)^2\right]^{-(1/2)}$, $\gamma = \alpha - \varphi - \theta$, $\theta = \arctan\dfrac{RC\omega_s}{1-\omega_s^2 LC}$,

$B = I_{gn}\dfrac{\tau^2}{\tau^2 - RC\tau + LC}$, $C_1 = -(A\sin\gamma + B)$, $C_2 = B/\tau - \omega_s A\cos\gamma$.

This fault analysis can also be seen from PSCAD/EMTDC simulation (Figures 4.5 and 4.6) with a vector-controlled sinusoidal PWM-VSI and DC cables. The simulation system parameters, initial values, and stage times are listed in Table 4.1. The serious first wave front occurs during the first stage and the freewheel effect happens at the beginning of stage 2, which are shown in Figure 4.6. The most vulnerable component – diodes – suffer during the freewheel stage, in which the current is seventy-three times the normal value (from 36 A to 2619 A); in this case, within 5 ms. The capacitor suffers from a large discharging current, which can be solved by operating the dedicated DC capacitor CB [4.12], or adding capacitor overcurrent protection [4.13], or simply using fuses as for distribution system capacitor banks [4.22].

4) Influence of Fault Resistance:

Usually, the circuit will experience oscillation if $R < 2\sqrt{L/C}$. Sometimes, a small fault resistance exists between the two faulted cables. This will make $R_f + R > 2\sqrt{L/C}$, which results in a first-order damping process. The DC-link voltage will not drop to zero, so no freewheel diode conduction occurs. In cases of short-circuit faults, fault resistances are generally small (e.g. 0.5 Ω). Hence the most

critical phase can sometimes be avoided, only overcurrent protection for the DC-link capacitor and cables are required. The overcurrent protection relay time setting is not that critical as well. The damping-only effect will be shown in cable ground fault, in which the ground resistance is always considerable.

Table 4.1: Simulation Parameters and Calculation Initial Values for Short-Circuit Fault

Simulation system parameters	Initial values	Times
$R = 0.12\ \Omega$	$V_0 = 1.0$ kV (DC)	$t_0 = 0$ s
$L = 0.56$ mH	$I_0 = 0.036$ kA (DC)	$t_1 = 4.44$ ms
$C = 10$ mF	$I'_0 = 2.619$ kA (DC)	
$R = 0.12 < 2\sqrt{L/C} = 0.473$	$V_g = 0.392$ kV (AC)	
	$\|Z\| = \|R+j\omega(L_{choke}+L)\| = 2.691$	
$L_{choke} = 8$ mH	$I_g = 0.392/2.691 = 0.146$ kA	

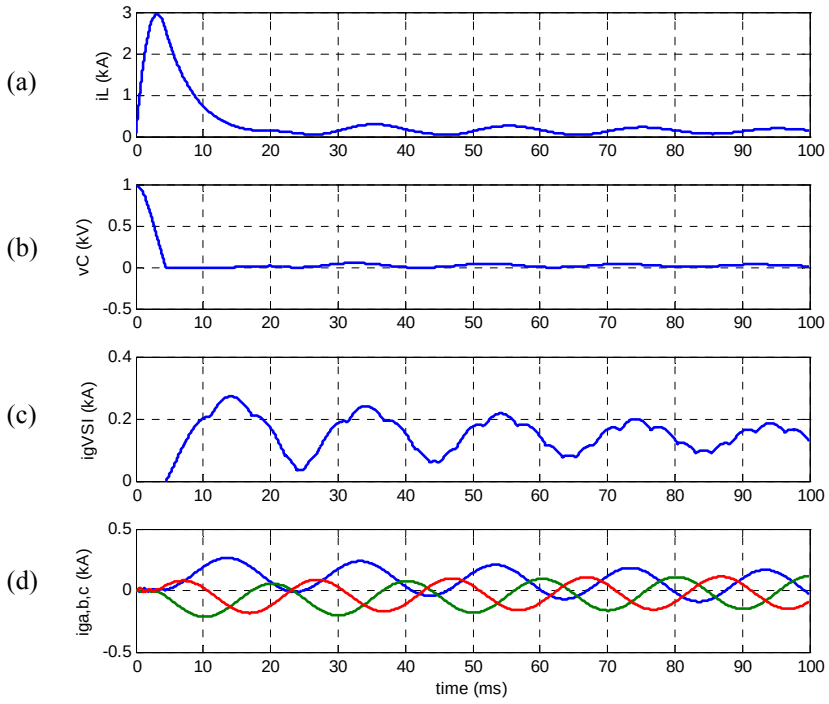

Figure 4.5: VSI with cable short-circuit fault simulation: (a) cable inductor current i_L; (b) DC-link capacitor voltage v_C; (c) current provided by grid VSI i_{gVSI}; (d) grid side three-phase currents $i_{g\,a,b,c}$.

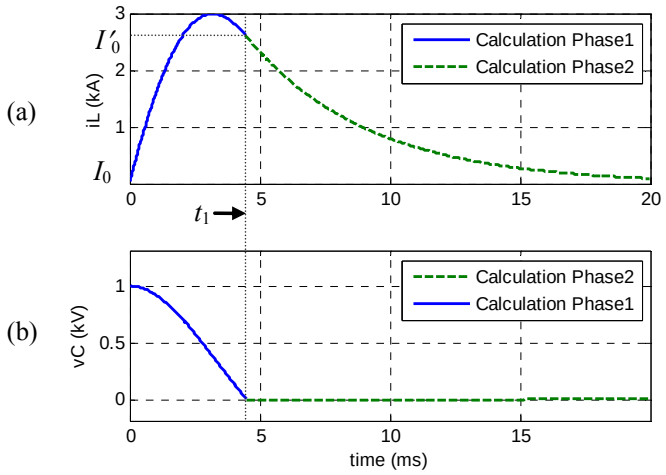

Figure 4.6: Diode freewheel effect and fault time phase illustration: (a) cable inductor current i_L; (b) DC-link capacitor voltage v_C.

4.3.2 VSI DC Cable Ground Fault

The ground fault analysis depends on the grounding system of the DC wind farm. Usually, the grounding points in a DC wind farm include the neutral of the step-up transformer, and the DC-link midpoint [4.11], [4.23], as shown in Figure 4.7. The latter grounding point can improve the imbalance between the positive and negative currents and voltages.

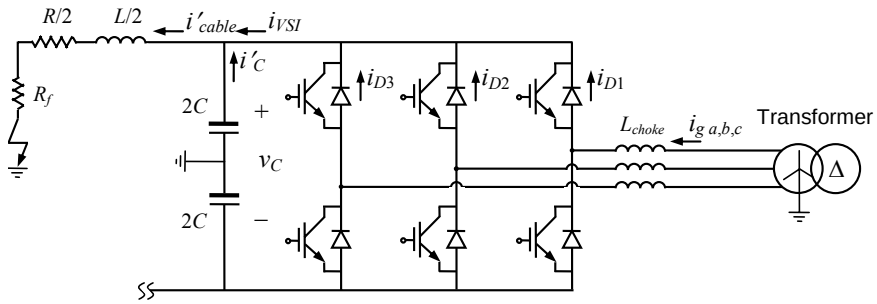

Figure 4.7: VSI with positive cable ground fault condition.

A ground fault will form a ground loop with the aforementioned grounding points. The blocked voltage source will act like an uncontrolled rectifier with DC-link voltage changing to the rectified voltage, so the current will flow through the diodes. This current depends on the impedance between the transformer and the ground fault point. The difference between positive and negative faults is the direction of current

and the bridge diodes that conduct. The fault resistance R_f cannot be ignored in this case, usually ground fault resistance varies from ohms to hundreds of ohms [4.6]. The equivalent circuit is shown in Figure 4.8 for the fault calculation, which is divided into transient and steady phases.

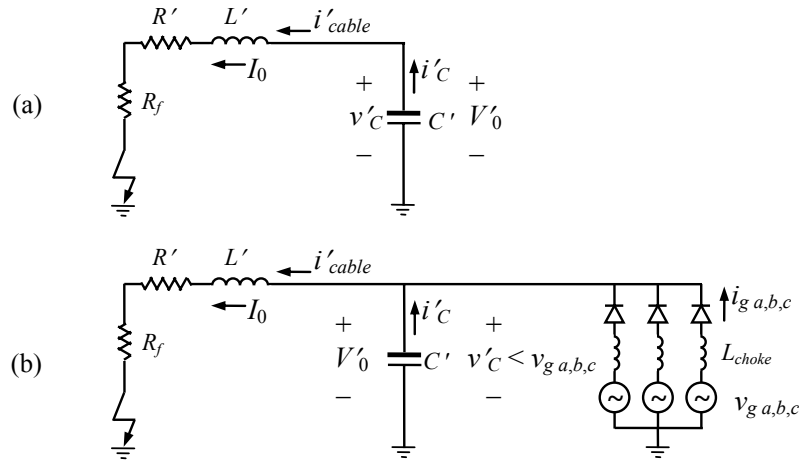

Figure 4.8: Equivalent circuit for the VSI with a cable ground fault calculation: (a) stage 1 – capacitor discharge; (b) stage 2 – grid current feeding.

1) Capacitor Discharge Stage (Natural Response):

This is the DC-link capacitor discharging stage as represented by Figure 4.8(a). Under the condition of $R_f + R' > 2\sqrt{L'/C'}$, the solution of the second-order circuit natural response gives a non-oscillating discharge process. The DC-link voltage will not drop to zero so no freewheel diode conduction occurs. Assume the fault happens at time t_0, the natural response (without inverter side current i_{VSI}) under initial conditions of $v'_C(t_0) = V_0$, $i'_{cable}(t_0) = I_0$ are

$$v'_C = A_1 e^{p_1 t} + A_2 e^{p_2 t} \tag{4.8}$$

$$i'_{cable} = C' \frac{dv'_C}{dt} = A_1 p_1 e^{p_1 t} + A_2 p_2 e^{p_2 t} \tag{4.9}$$

where $p_{1,2} = -\dfrac{R_f + R'}{2L'} \pm \sqrt{\left(\dfrac{R_f + R'}{2L'}\right)^2 - \dfrac{1}{L'C'}}$, $A_1 = \dfrac{1}{p_2 - p_1}\left(p_2 V_0 + \dfrac{I_0}{C'}\right)$,

$A_2 = \dfrac{1}{p_2 - p_1}\left(-p_1 V_0 - \dfrac{I_0}{C'}\right)$.

This stage is an *RLC* circuit until the positive DC voltage drops to below any grid phase voltage. It is difficult to determine an analytical expression for the time t_1 when capacitor voltage drops below any grid phase voltage but numerical methods can be used to find the time solution.

2) Grid Side Current Feeding Stage (Forced Response):

This transient phase can be expressed by third-order state-space equations

$$\begin{pmatrix} \dot{v}'_C \\ \dot{i}'_{cable} \\ \dot{i}_{L_{choke}} \end{pmatrix} = \begin{pmatrix} 0 & -\frac{1}{C'} & \frac{1}{C'} \\ \frac{1}{L'} & -\frac{R_f + R'}{L'} & 0 \\ -\frac{1}{L_{choke}} & 0 & 0 \end{pmatrix} \begin{pmatrix} v'_C \\ i'_{cable} \\ i_{L_{choke}} \end{pmatrix} + \begin{pmatrix} 0 \\ 0 \\ 1/L_{choke} \end{pmatrix} v_{ga,b,c} \tag{4.10}$$

where v'_C, i'_{cable}, and $i_{L_{choke}}$ are the state variables. The choke inductance can also include the transformer and its star-grounding inductance in case of an arc-distinguishing coil connected in low or medium voltage situations. It is difficult to derive analytical expressions for the voltages and currents during the fault so it is numerically simulated. There are no particular effects on the diodes (unlike the freewheel phase during short-circuits). The capacitor voltage drops to a new steady state in 30 milliseconds; meanwhile the inductor current experiences a large transient of 0.8 kA (11 times rated current), Figure 4.9(a).

It cannot be solved continuously because of commutation between diodes. Therefore, for each diode conduction period, the status equations of (4.10) need to be solved using the previous variable as the initial state for the present calculation.

3) Steady State:

The steady-state equations can be determined. The total impedance is

$$Z = (R_f + R + j\omega_s L) \| (1/j\omega_s C) + j\omega_s L_{choke} = |Z| \angle \theta' \tag{4.11}$$

Then the current through diode is

$$i_{D1} = i_{ga,(>0)} = \frac{V_g \angle \alpha}{|Z| \angle \theta'} = \frac{V_g}{|Z|} \angle \alpha - \theta' \,. \tag{4.12}$$

Simulation results are shown in Figure 4.9. System parameters and calculation results are shown in Table 4.2. In simulation, it is assumed that the DC power source is tripped immediately after the fault to avoid a DC-link capacitor overvoltage on the negative side. Each phase diode conducts when the DC voltage drops below its phase voltage, shown as an "×" along the DC voltage in Figure 4.9. The diode current during the transient state peaks at 0.185 kA, Figure 4.9, about twice rated current magnitude. The steady-state amplitude is 0.1661 kA, which is slightly lower than the maximum.

For the fault analysis, other components in practical application should be considered in the analysis. For example, the capacitor protection itself – such as a snubber acting as a current limiter [4.11] can be included. Although this will influence the transient pattern, the analysis of the oscillation and damping calculation from the analysis is still effective.

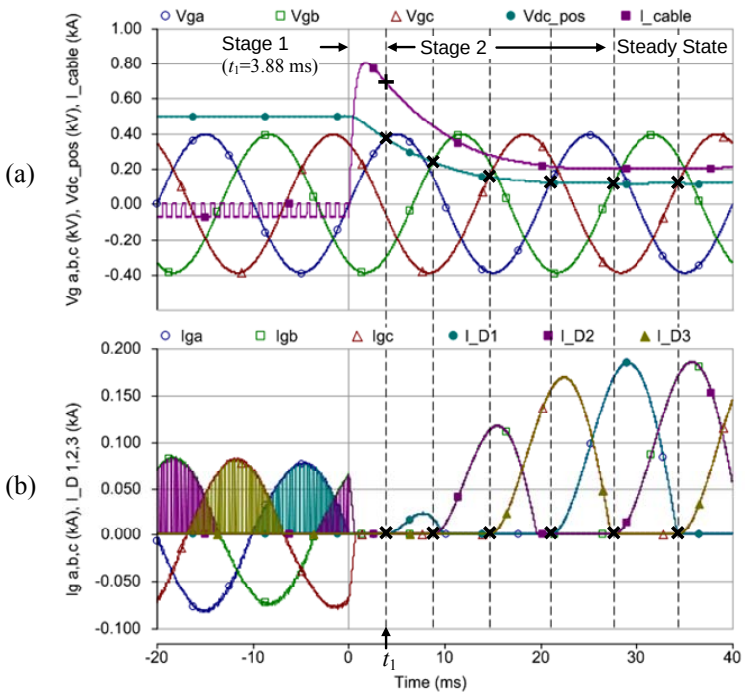

Figure 4.9: VSC cable ground fault and stage definition: (a) grid three-phase voltages $v_{g\,a,b,c}$ (kV), DC-link positive voltage v_{dc_pos} (kV), cable current i_{cable} (kA); (b) grid three-phase currents $i_{g\,a,b,c}$ (kA), three-phase diode current $i_{D\,1,2,3}$ (kA).

Table 4.2: Simulation Parameters and Calculation for Ground Fault

Simulation system parameters	Initial / Calculation values	Times
$R' = R/2 = 0.06\ \Omega$, $R_f = 0.5\ \Omega$	$V_0 = 0.5$ kV (DC)	$t_0 = 0$ s
$L' = L/2 = 0.28$ mH	$I_0 = -0.063$ kA (DC)	$t_1 = 3.88$ ms
$C' = 2C = 20$ mF	$V_g = 0.392$ kV (AC)	
$R_f + R' = 0.56 > 2\sqrt{L'/C'} = 0.237$	$Z = 2.36\angle 88.96°$	
$L_{choke} = 8$ mH	$I_g = 0.1661$ kA (AC)	

4.3.3 DC Cable Open-Circuit Fault

Open-circuit faults will only influence generator-side converters but not grid-side converters, although this can influence the online AC grid system because of the abrupt generation loss. The disruption of energy transmission path means that redundant energy generated by the turbine-generator system will cause overvoltage behind the rectifier and generator acceleration and overspeed. This can be solved by applying the dump load at the generator AC side or a DC-chopper after the rectifier to limit the rectified DC overvoltage. Energy storage systems (ESS) could also be used at the rectifier DC-link [4.24].

4.3.4 Multi-level Voltage-Source Converters

The fault analysis is applied to the common multi-level converters. Three-level diode neutral-point-clamp (3L-NPC) converter and five-level flying capacitor (5L-FC) converter are illustrated for cable ground fault and short-circuit fault, respectively (Figure 4.10). From the topology, the above two-level analysis remains effective for them as the main characteristics remain: a closed loop for capacitance discharge via freewheel diodes.

The diodes share short-circuit fault current, in Figure 4.10(a), except that during the first stage D_1 carries more current due to the discharge of capacitor C_2. The ground fault with clamping diodes form a freewheel loop when v'_C drops to zero, shown as dashed line in Figure 4.10(b), just like the second stage of the above short-circuit fault. Hence the short-circuit fault analysis can be applied to this situation. For

cascaded modular multi-level converters, each cell has its own capacitor. There is no large capacitance across the DC-link, therefore, no discharge current under a DC short-circuit fault. Protection control and fast switching within each cell make this topology tolerant to short-circuit faults. However, during the DC network development with all kinds of VSCs, it is not possible to build a system with these fault-tolerant converters only. Hence it is still necessary to analyse and provide system protection as a whole.

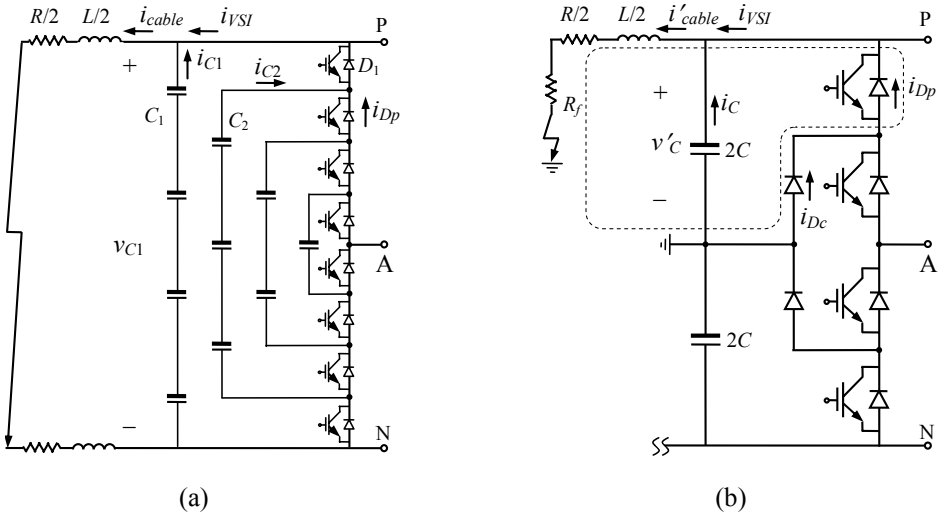

Figure 4.10: Multi-level VSC fault condition illustration: (a) five-level flying-capacitor converter under cable short-circuit fault; (b) three-level diode neutral-point-clamp converter under cable ground fault.

4.3.5 Fault Characteristic Summary

The DC-link voltage change can be used to separate AC faults from DC faults. For AC faults, the redundant energy that cannot be transferred to grid is stored in DC-link capacitor and results in the increase of DC-link voltage. But for inner DC faults, the DC-link voltage will collapse. In Table 4.3, fault overcurrent is characterised in three aspects: 1) initial current change, 2) first wave rise-time, and 3) oscillation pattern, which can all be used for identification and detection of fault type.

Table 4.3: Fault Characteristic Summary

Fault type		AC faults	Short-circuit	Ground-fault	Open-circuit
Direction of DC-link voltage change		↑	↓	↓	↓
DC side fault current	Initial current change	—	Up to 73 times of rating	Up to 11 times of rating	—
	Rise-time of first wave front	—	< 5 ms	> 0.25(1/f_s) = 5 ms	—
	Oscillation pattern	—	*RLC* discharging, *RL* diode freewheel	Sinusoidal	—

f_s – the synchronous time frequency.

4.4 DC Fault Protection Methods

The aforementioned DC fault analysis and detection can be applied to the design of the protection system. The main principles are the same with AC distribution system protection: time-response, selectivity, and reliability. There are few published works on DC system protection with a DC CB and relay configuration. Most reported methods avoid using DC CBs, because of the lag in development and cost. Moreover, no relay experience can be gained from the traditional HVDC systems. In most cases, the DC faults discussed here have similar characteristics to the DC-link voltage collapse but with different amplitudes of overcurrent. Hence, overcurrent protection with a directional element can realise fault location without communication between the two switchgears at the terminals of a long cable. The selectivity can be realised by using relay time delay or time coordination curves.

4.4.1 DC Switchgear

There are some options for switchgear: *1) AC CB and DC Switch:* AC-side CBs are used for fault current extinguishing, coordinating with DC fast switches [4.15]; *2) DC CB:* fully-functioned DC CB – the optimal option; *3) fuse:* used for systems that only require fast response for protection and no need to reenergise the system automatically. Fuses could be used at each generator's converter output side as shown in Figure 4.1. Considering the strict time-response requirement, AC CBs will not be suitable.

DC circuit breakers are required for the collection and transmission systems as they require fast response under DC fault conditions. The AC side breaker and DC switch coordination obviously cannot function fast enough; when the fault occurs, the mechanical arc-extinguishing AC side breakers operation time cannot avoid the diode freewheel effect analysed above, hence is not capable of fast fault clearance. Moreover, the allocation of DC breakers can enhance the system reliability, especially for the loop network topology, in which the AC-side breakers and DC switches can only be used for a "cut-and-try" method as proposed in [4.15]. Detailed design of DC CBs and appropriate fuse selection is required to satisfy issues such as effective arc-extinguishing and fault clearance. This is a significant challenge for DC switchgear design.

4.4.2 Measurement and Relaying Configuration

The main protection should operate as fast as possible, with one backup protection, operating after a time delay in case the main protection malfunctions. However, the backup protection still needs to be fast enough to avoid the freewheel effect, which is less than 5 ms in the aforementioned example. Therefore, the protection time response should be at the millisecond level, depending on the protection coordination (selection) method. Distance protection is usually applied. The main principle is to estimate the impedance between the relay point and the fault point. If this falls within a given distance, the relay system waits for a corresponding time delay before activation to realise selection.

1) Communication Solution:

If each cable section is not too long, the relay detecting opposite current flow will communicate with its former relay. If their current directions are the same, then the fault has occurred outside this section. The relay will wait for a delay time. If the correct directions are different, the fault is between the relays and this relay operates immediately. Since there is no further CB at the terminal of a string or star, the CB at this relay point will trip instantly. If all the relay delay times are exceeded and there is still overcurrent, the circuit breaker will trip as backup protection.

2) Distance Evaluation Solution:

Traditional AC system distance protection uses impedance to represent the distance from fault point to the relay point. The distance judgement is made with *mho* characteristic or an impedance circle. But for DC systems and during fault transients, the frequency changes abruptly, so no grid fundamental frequency impedance can be defined for distance protection. In three-phase AC systems, distance protection uses symmetrical component analysis to avoid the influence of fault resistance [4.6]. However, in DC systems, this is not possible. A new distance evaluation solution is proposed.

For a fast time-response protection system, if the main protection and backup coordination are capable of securely protecting the system, at the protection stage, there is no need to use time-consuming methods to accurately locate the distance to the fault point. Rough distance evaluation is enough for a relay decision. This relies on the distance characteristics of overcurrent value and critical time for the freewheel effect. The DC-link voltage and cable inductor current variation to different fault distances are shown in Figure 4.11, where *D* is the cable length of one section. As the distance increases, the fault overcurrent reduces and the time-to-peak current increases.

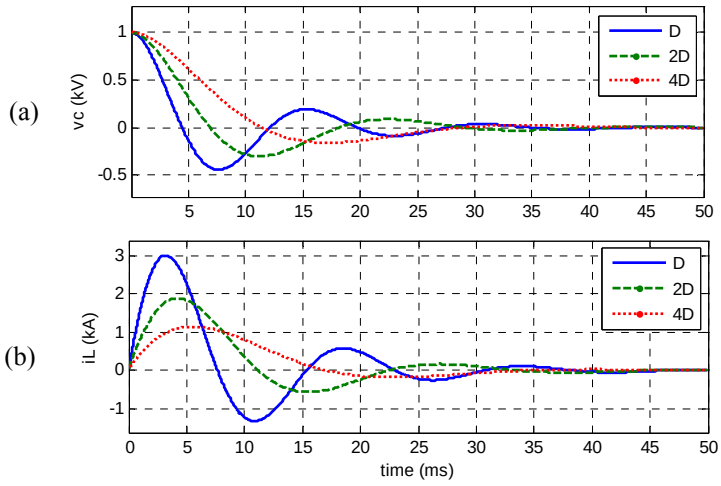

Figure 4.11: Influence of fault distance on the system performance: (a) DC-link capacitor voltages of difference distances; (b) cable inductor currents of different distances.

The critical time limit is when the DC-link voltage drops to zero as in Figure 4.11(a). At this time, the freewheel diodes conduct. With respect to the distance x, the critical time is

$$t_1 - t_0 = \left[\pi - \arctan\left(V_0 C\omega' / (V_0 C\delta - I_0)\right)\right]/\omega' \tag{4.13}$$

where

$$\omega' = \sqrt{\omega_0^2 / x - \delta^2}\ . \tag{4.14}$$

The freewheel overcurrent is the cable inductor current at the critical time. The critical freewheel current and time with respect to distance is shown in Figure 4.12. The critical time is the strict upper limit for the total switchgear operation time. The current-distance curve in Figure 4.12(a) can be used for relay configuration. Examples are shown in Figure 4.13. $t(n)$ is the relay time delay curve at point (n). Here, the critical time is used to coordinate the delay time of the relays, shown in Figure 4.13(a), which is easier to apply than the Figure 4.13(b) method.

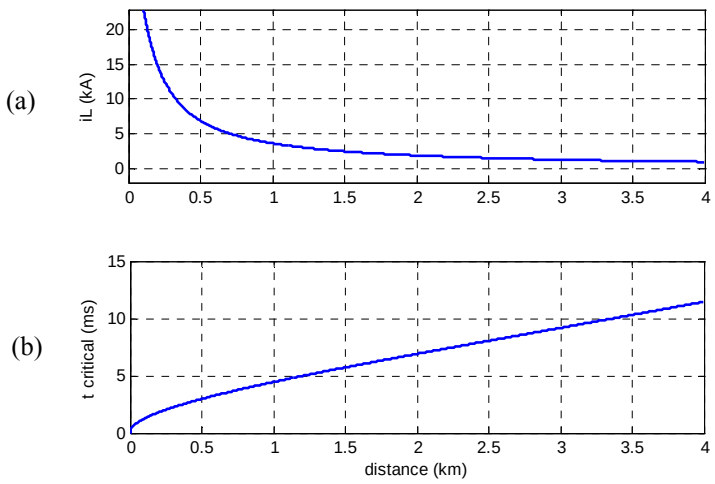

Figure 4.12: Influence of fault distance on the system performance: (a) initial freewheel current according to the fault distance; (b) DC-link capacitor voltage collapse time change with distance. (Each cable section can be 1 km long.)

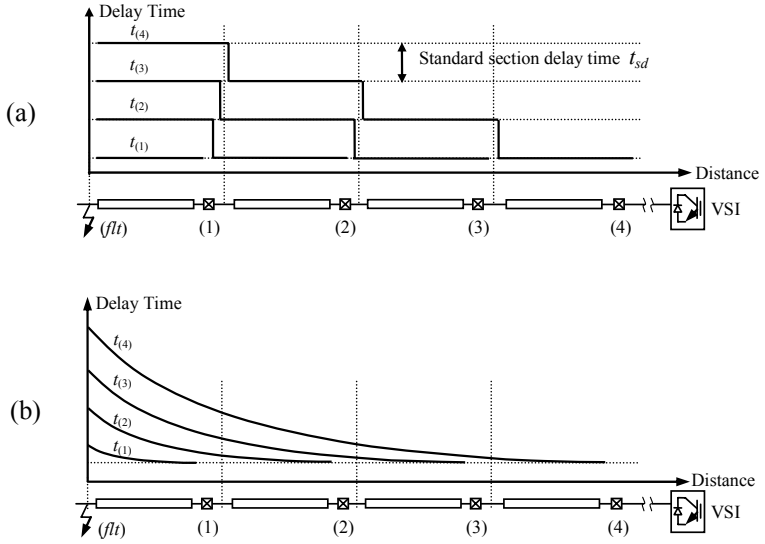

Figure 4.13: Relay delay time coordination configuration: (a) with constant delay time distance relays; (b) with overcurrent-distance setting relays.

For DC cables, assume per kilometre resistance and inductance are r and l, respectively. The grounding capacitor is omitted here due to the relatively low voltage level and short-length collection cable between turbines. Even for the high-power case where grounding capacitors are considerable, the capacitors can be considered into each side of the cable's DC-link capacitor. Suppose each section has the same length D and ignore the possible different r and l values for different sections due to cable rating optimisation. (The closer the cable is to the collection platform, the higher the current rating of the power cable.) Even though each section may have a different length, if the r–l ratio is constant, this will not influence distance selection performance.

Here, DC voltage dividers are used for distance measurement and representation. The fault distance is evaluated by using two voltage dividers instead of a pair of voltage and current measurements. Due to a switched-mode DC system, the DC voltages and currents are rapidly changing (with on and off periods) and the division of voltage by current causes calculation problems and false decisions. Moreover, the abrupt change of current may cause measurement error, while moderate voltage changes along the cable should be easy to deal with. This discontinuous DC current feature will not influence the overcurrent detection unit; the relay only operates on overcurrent.

The measurements and distance relationship are illustrated in Figure 4.14. The fault voltage at switchgear relay point (n) is

$$v_{(n)} = v_{(flt)} + x^* r i_{(n)} + x^* l \frac{di_{(n)}}{dt} = R_f i_{(flt)} + x^* \left(r i_{(n)} + l \frac{di_{(n)}}{dt} \right) \tag{4.15}$$

where x^* is the real fault distance and R_f is the fault resistance.

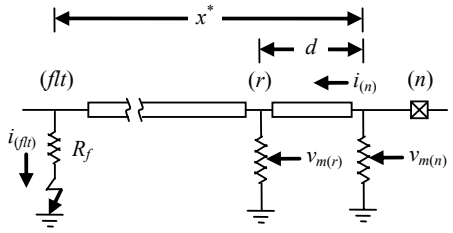

Figure 4.14: Distance evaluation with two voltage divider measurements.

Another relay voltage sensor unit (r) is used as a reference for the relative voltage calculation; it is located close to the main relay point on the same section of cable, as shown in Figure 4.14 to avoid long-distance communication issues. The measured values using voltage dividers are $v_{m(n)} = k_v v_{(n)}$ and $v_{m(r)} = k_v v_{(r)}$, where k_v is the voltage divider ratio. The distance between them is known d, so the fault distance measured from this reference is

$$x = \frac{v_{(n)}}{v_{(n)} - v_{(r)}} d = \frac{v_{m(n)}}{v_{m(n)} - v_{m(r)}} d \tag{4.16}$$

where

$$v_{(n)} - v_{(r)} = d \left(r i_{(n)} + l \frac{di_{(n)}}{dt} \right). \tag{4.17}$$

For metallic grounding or a short-circuit fault, $v_{(flt)} = R_f \, i_{(flt)} = 0$, so the cable impedance is proportional to the distance. Measured distance $x = x^*$ can be used for the distance relay configuration. If the distance calculation is within a given section, the relay will operate with a corresponding time delay to realise selection as shown in Figure 4.13(a). The delay time of all the sections should be less than the critical time to avoid freewheel diode overcurrent.

For high resistance faults, which are more common in ground faults, the existence of R_f and the difference between $i_{(flt)}$ and $i_{(n)}$ make the evaluation of x^* difficult. Usually, this kind of fault is not as serious as the metallic grounding or short circuit, so it may not require fast time-response protection, hence it can be fulfilled by the overcurrent setting. Considering the backup configuration and the critical time limit shown in Figure 4.12(b), a method to estimate the fault distance is proposed by estimating the cable distance and equivalent fault resistance.

The distance measured in (4.16) in this case is not accurate because of the influence of fault resistance, but this is the only information that can be used for time delay decision. Equation (4.17) presents the real voltage drop between the two relay points, which reflects the real voltage drop excluding the influence of $R_f\ i_{(flt)}$. But R_f still cannot be exactly obtained even with the source side tripped (i.e. $i_{(flt)} = i_{(n)}$). One solution is to measure the reactance to exclude the resistance influence, but this is hard to achieve. Under the assumption that the DC power source side is immediately tripped, the voltage measurement is

$$v_{(n)} = R_f i_{(n)} + x^*\left(ri_{(n)} + l\frac{di_{(n)}}{dt}\right) = R_f i_{(n)} + x^* ri_{(n)}\left(1+K\right) \tag{4.18}$$

where

$$K = \left(l\frac{di_{(n)}}{dt}\right) \Big/ \left(ri_{(n)}\right) \tag{4.19}$$

is the equivalent ratio of reactance to resistance voltage drops. Then defining

$$R_D = D\left(ri_{(n)} + l\frac{di_{(n)}}{dt}\right) \Big/ i_{(n)} = Dr(1+K) \tag{4.20}$$

as the equivalent resistance per section. Hence, the measured distance

$$x = \frac{v_{(n)}}{v_{(n)} - v_{(r)}} d = \frac{R_f i_{(n)} + x^* ri_{(n)}\left(1+K\right)}{\left(ri_{(n)} + l\dfrac{di_{(n)}}{dt}\right)} = \frac{R_f}{R_D} D + x^*. \tag{4.21}$$

In practical applications, it is not economical to allocate CBs at each collection unit end in a collection string. For a string with ten turbines, the total number of CBs can

be 3 or 4, so the delay time will be about 4.44/4 ms in the aforementioned case. This requires the DC CBs to operate at a 1-ms level, which is achievable. The evaluation decision procedure is shown in the distance estimation table (Table 4.4), used for coordination, to allocate main protection and backup protection. The standard section delay time t_{sd} for coordination is calculated according to the critical time divided by the corresponding section number.

Table 4.4: Distance Protection Relay Time Coordination for a 3-Section Example

Relay	Fault distance	Fault region	Fault resistance	Confidence in Discrimination	Switch Delay
(1)	$x \le D$	(1)-(0)	--	Yes	0
	$x > D$	(1)-(0)	$R_f > 0$	Yes	0
(2)	$x \le D$	(2)-(1)	--	Yes	0
	$D < x \le 2D$	(2)-(1)	$R_f \ge R_D$	No	t_{sd}
		(1)-(0)	$0 \le R_f < R_D$		
	$x > 2D$	(2)-(1)	$R_f \ge 2R_D$	No	$2t_{sd}$
		(1)-(0)	$0 \le R_f < R_D$		
(3)	$x < D$	(3)-(2)	--	Yes	0
	$D < x \le 2D$	(3)-(2)	$R_f \ge R_D$	No	t_{sd}
		(2)-(1)	$0 \le R_f < R_D$		
	$2D < x \le 3D$	(3)-(2)	$R_f \ge 3R_D$	No	$2t_{sd}$
		(2)-(1)	$R_D \le R_f < 2R_D$		
		(1)-(0)	$0 \le R_f < R_D$		
	$x > 3D$	(3)-(2)	$R_f \ge 3R_D$	No	$3t_{sd}$
		(2)-(1)	$R_D \le R_f < 2R_D$		
		(1)-(0)	$0 \le R_f < R_D$		

A three-section example is shown in Table 4.4. For the relay (1) at the far end of a string cable, the measured distance only falls into two conditions. Regardless of what is the measured x value is, the CB will immediately operate when overcurrent is detected. For relay (2), if $x \le D$, it is certain that the fault occurred inside the cable between (2) and (1), so the delay time is also 0. But if $x > D$, whether it is smaller than $2D$, it is hard to decide whether cable (2)-(1) or (1)-(0) is faulted. But the bigger the evaluated distance x is, the less serious the fault is, so the time delay is set as a backup standard, with one t_{sd} delay or $2t_{sd}$ delay when $x > 2D$. The closer the relay is to the inverter, the greater the possibilities are to assess, and the longer the time is available, for distance measurement. The evaluation procedure using different

distance calculation values to set relay delay times is to distinguish the main and backup protections. This ensures that the fault is cleared by at least the backup protection.

4.4.3 Small-Scale System Protection Option

A simple method is proposed for small-scale, low-power scenarios. Reverse diodes can be used to restrain the fault current from flowing into the DC cable system. The VSI diodes clamp the voltage after the DC-link capacitor, another pair of diodes can be used before the DC-link to block the fault current flowing in the other direction. In this way, the DC-link voltage will not change abruptly. The DC-chopper circuit is used in case of DC-link overvoltage. The reverse diode positions and current flows are shown in Figure 4.15.

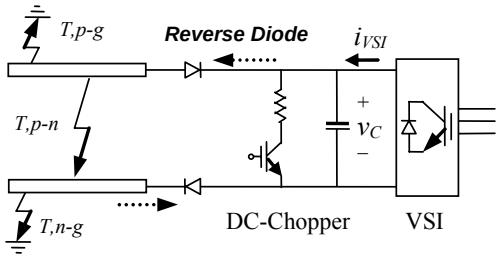

Figure 4.15: Reverse-diode protection method and current flow directions.

PSCAD/EMTDC simulations are carried out. The simulated system topology is a DC wind farm collection grid with diode-rectifier and DC/DC boost conversion in parallel with the grid-side VSI. This is economical and practical for small-scale systems. The simulated DC wind farm system includes two equivalent parallel-connected wind turbine generation systems. The faults simulated are: 1) a short-circuit fault for 1.0 s and 2) a cable ground fault for 1.0 s. Both occur on the cable of one generation system. Zero fault resistance is considered to give the most serious condition.

The DC-link capacitor voltage and inverter-side reverse currents are shown in Figure 4.16. For a short-circuit fault, the DC-link voltage is clamped to be around the pre-fault value and no current flows through the diodes to charge the capacitor [i.e., the inverter current is almost zero in Figure 4.16(b)], compared with that of up to

2.50 kA in Figure 4.16(a). The overvoltage after the recovery of fault will be reduced by the DC-chopper. For a ground-fault condition, no DC-chopper is needed. There is an inverter overcurrent, but this is limited to twice of the normal value, which is tolerable for devices.

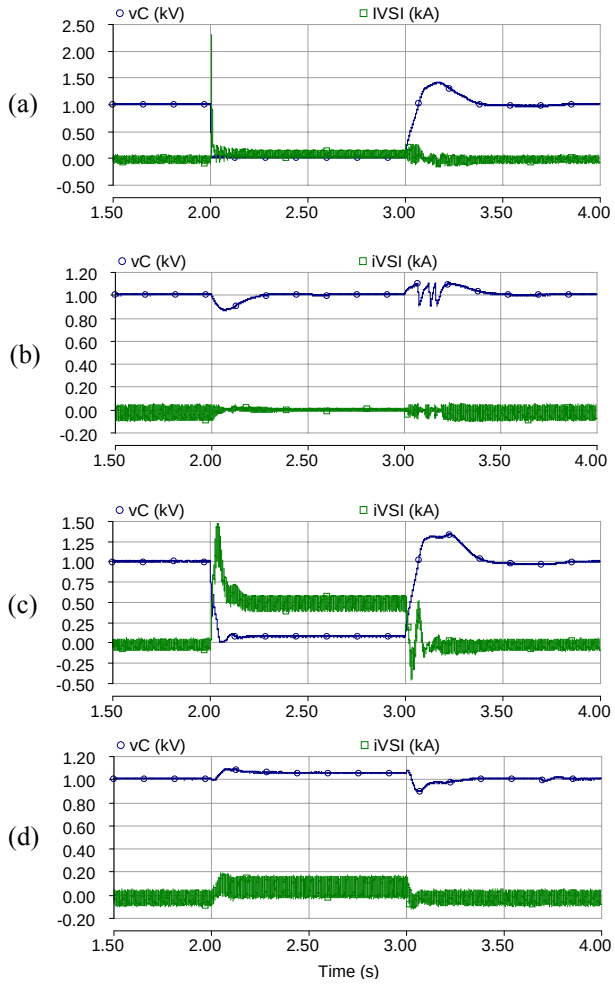

Figure 4.16: Reverse-diode and DC-chopper protection method performance (DC-link capacitor voltage v_C and VSI current i_{VSI}) simulation: (a) short-circuit fault without protection; (b) short-circuit fault with protection; (c) cable ground fault without protection; (d) cable ground fault with protection.

4.5 DC Wind Farm Protection Simulation Results

The proposed protection method is applied to specific DC wind farm systems and verified by PSCAD/EMTDC simulations. The topologies investigated are small-scale DC wind farm collection grids with star and string connections, respectively. The generators are PMSGs. The generator-side AC/DC converters are three-phase

diode-rectifiers connected to boost DC/DC converters for energy conversion and maximum power point tracking. The simulated DC wind farm system includes two equivalent wind turbine generation systems, parallel-connected, to the DC-link and grid-side inverter. The faults simulated are: 1) for the star connection, a short-circuit fault on the cable of one collection unit; 2) for the string connection, a grounding fault on the collection cable of one unit is close to the inverter side. The generator and DC cable parameters are provided in Table 4.5 and 4.6.

Table 4.5: PMSG Parameters

Parameter	Value	Parameter	Value
Rated power P_n	25 kW	Pole pair no. P_p	12
Rated stator voltage V_{sn}	450 V	Phase resistance	0.068 p.u.
Rated frequency f_g	30 Hz	Phase inductance	0.427 p.u.

Table 4.6: DC Cable Parameters

Parameter	Value	Parameter	Value
Resistance r	0.06 Ω/km	Collection cable (1)-(0)	0.5 km
Inductance l	0.28 mH/km	Collection cable (2)-(0) for star / (2)-(1) for string	0.5 km
Rating voltage	1 kV	Transmission cable (3)-(2)	1.0 km

4.5.1 Short-Circuit Fault Condition

Figure 4.17 shows the system performance under a short-circuit fault at t = 3.0 s at the midpoint of one collection cable of a generation system. To show the selection validity, this fault is applied to the star connected system and the fault point is on one collection unit cable. The selectivity should make sure this fault will not influence the power transferred to the inverter from the other turbine system. The protection opens the faulted side CB immediately. The total power transmitted to the onshore grid drops to 0.5 p.u. The VSI control maintains the DC-link voltage constant with a slight transient, Figure 4.17(a). In Figure 4.18, the currents at the two relay points show that under voltage control, the current at the grid switchgear relay point (3) $i_{(3)}$ drops to a half due to the trip of CB (1) ($i_{(1)}$ = 0); hence, the total power decreases by half.

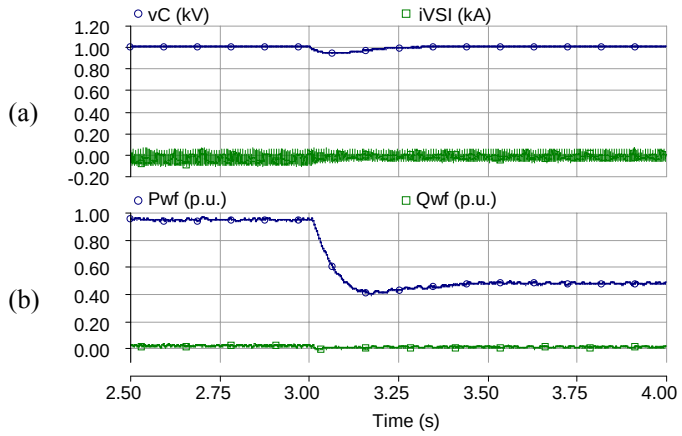

Figure 4.17: Wind farm performance under short-circuit fault at one turbine-generator collection unit cable in star connection: (a) DC-link capacitor voltage v_C (kV) and VSI current i_{VSI} (kA); (b) wind farm total active and reactive power P_{wf} (p.u.), Q_{wf} (p.u.).

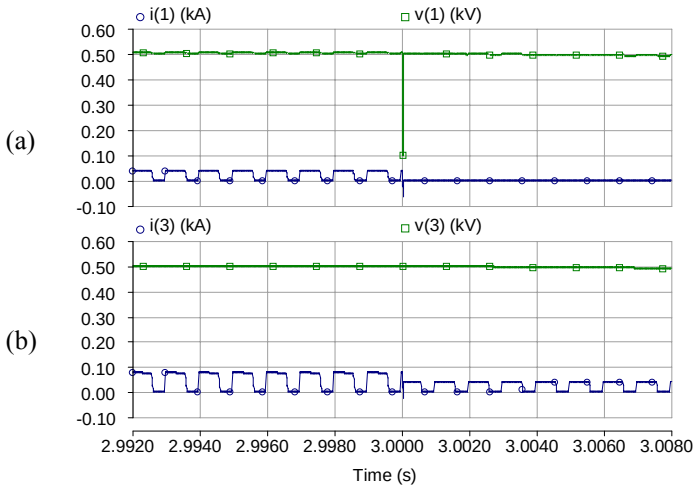

Figure 4.18: Relay measurements under short-circuit fault at the first wind turbine collection unit, star connection: (a) current and voltage measurements at relay point (1) of the faulted cable, $i_{(1)}$ (kA) and $v_{(1)}$ (kV); (b) current and voltage measurements at relay point (3) of the transmission cable, $i_{(3)}$ (kA) and $v_{(3)}$ (kV).

In Figure 4.19, currents and voltages are scaled to show the time response of the protection system. The overcurrent relay threshold is set to be 1.5 p.u. (60 A). It takes about 70 μs to reach that value and then immediate switching is carried out. The DC CB simulated is a self-defined PSCAD model of a bi-directional IGBT/diode switch, with gate control from the relay system. The actual minimum extinction time for the IGBT is set as 10 μs in this case, which is adequate for IGBTs (commonly several microseconds [4.25]). Hence, in total, it takes 80 μs to actually extinguish the fault

current, much less than the freewheel effect time, 5.1 ms for the fault distance of 1.25 km [calculated from (4.13) and shown in Figure 4.12(b)].

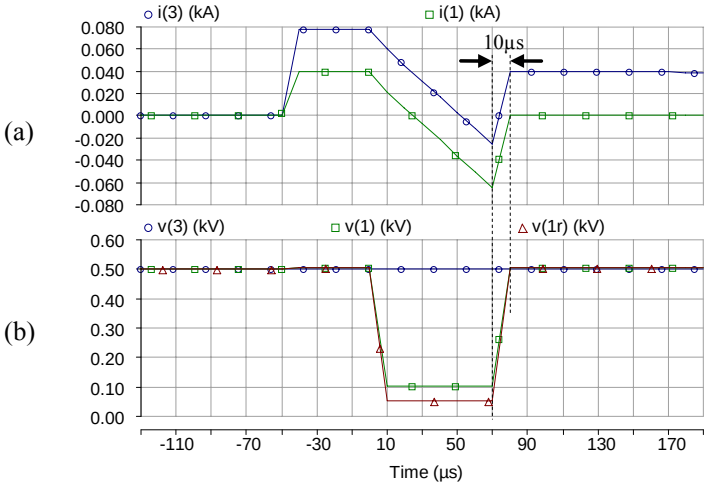

Figure 4.19: Zoomed relay measurements under short-circuit fault condition: (a) current measurements; (b) voltage measurements including relay (1) reference voltage $v_{(1r)}$ (kV).

The voltage measurements used for distance evaluation are shown in Figure 4.19(b). After the fault occurs, the relay point (1) voltage $v_{(1)}$ drops to about 100V, with a reference measurement (1r) voltage $v_{(1r)}$ at about 50V. According to the distance evaluation (4.16), $x = 0.1d$ / (0.1–0.05) = 0.25 km, where d is known as 0.125 km. This is less than the cable length of 0.5 km, which means the overcurrent relay should operate without time delay as long as it detects reverse overcurrent exceeding the 1.5-p.u. threshold value. Moreover, the evaluated distance is accurate (at the midpoint of the 0.5-km collection cable), because the short-circuit resistance is zero in this case. Here, it is assumed that the measurements and calculation can be completed within the time in which the overcurrent is reached – about 60 μs in Figure 4.19(b).

4.5.2 Cable Ground Fault Condition

The performance of the cable ground fault protection is shown in Figure 4.20. The ground fault with a resistance of 5 Ω occurs on the second collection cable in a collection string (also the midpoint), so the switchgear trip means there will be no power flow to the grid, as shown in Figure 4.20(b). Figure 4.21 shows the collection cable (2)-(1) DC CB relay (2) current and voltage measurements. At the instant of the

fault, t = 3.0 s, the current direction is opposite; it feeds current into the fault. Although the direction element can detect the fault current direction change, the overcurrent threshold 1.5 p.u. is not reached, so no trip occurs until the delay time has passed. The evaluated fault distance includes the influence of fault resistance, hence it is possible to misjudge the fault location. The fault resistance can restrict the overcurrent so it is not as severe as metallic fault conditions. The time delay is set as calculated from the fault distance and delay time concept. The evaluated distance value of relay (2) x is intolerable now (an unreasonably large value, much larger than the total collection length – 1 km) because of the high fault resistance. So the time delay of (2) is set to be that for 1 km – 4.44 ms in Figure 4.21, and that of (3) is the total value of critical time for the entire 2-km cable – 6.89 ms. Figure 4.22 shows the CB switch timing at relay point (2).

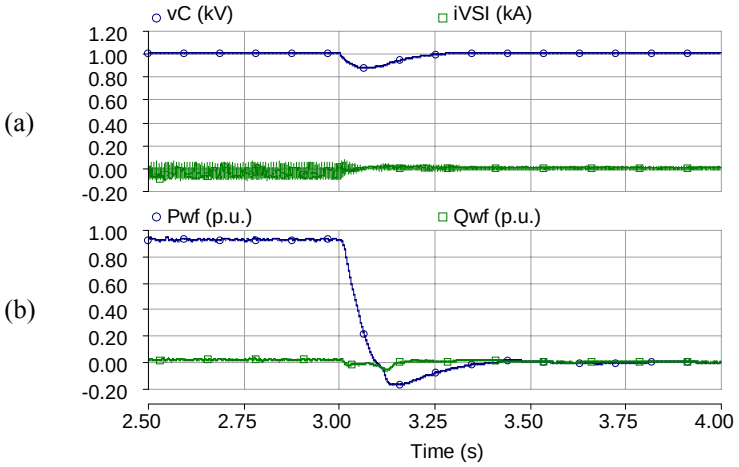

Figure 4.20: Wind farm performance under cable ground fault at the second turbine-generator collection unit cable in string connection: (a) DC-link capacitor voltage v_C (kV) and VSI current i_{VSI} (kA); (b) wind farm total active and reactive power P_{wf} (p.u.), Q_{wf} (p.u.).

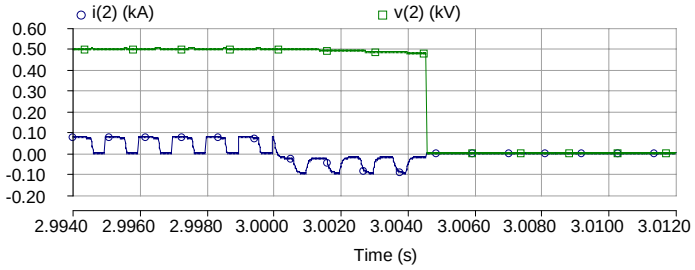

Figure 4.21: Relay measurements under cable ground fault condition, at the relay point (2), current $i_{(2)}$ (kA) and voltage $v_{(2)}$ (kV).

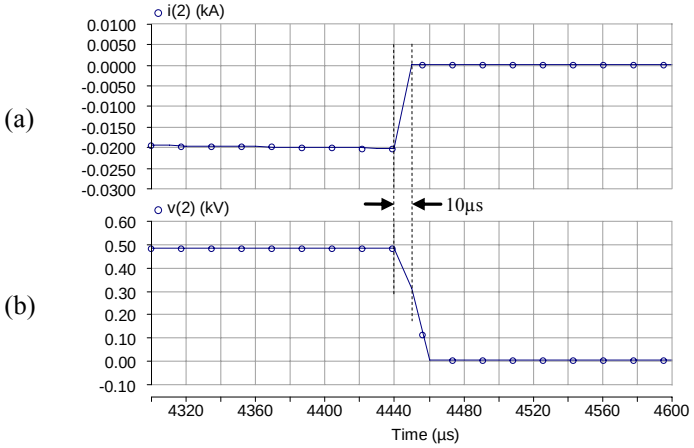

Figure 4.22: Zoomed relay measurements under ground fault condition: (a) relay current measurement; (b) relay voltage measurement.

4.6 Ground Fault Location and Resistance Evaluation

In three-phase ac systems, distance protection uses symmetrical component analysis to avoid the influence of fault resistance [4.5]. However, in DC systems this is not available. Ground faults are not as serious as short-circuit condition as the grounding is always with a large fault resistance; however, they occur more frequently. Moreover, the large fault resistance results in inaccurate evaluation of distance for protection coordination. To show the influence of fault resistance and distances on the system performance, from numerical calculation of (4.10), the time at the end of stage 1 t_1, DC-link voltage v_{C1}, and cable current i_{cable1} variations to different fault resistances and distances are shown in Figures 4.23, 4.24, and 4.25, respectively. Generally, as resistance and distance increases the fault overcurrent reduces and the time the diodes start conducting increases.

Based on the above analysis, a new fault location approach for distance and ground resistance evaluation is proposed here for online applications. The results can also be used for offline maintenance and fault location without injecting signals into a faulty cable, or a prediction before the application of the time-consuming tracing location methods. With the measurement values of $v'_{C,mea}$ and $i_{cable,mea}$, and the time when $v'_{C,mea}$ drops to below any phase value of the grid voltages $v_{g\,a,b,c}$ - $t_{1,mea}$, the fault loop total resistance and inductance can be solved from

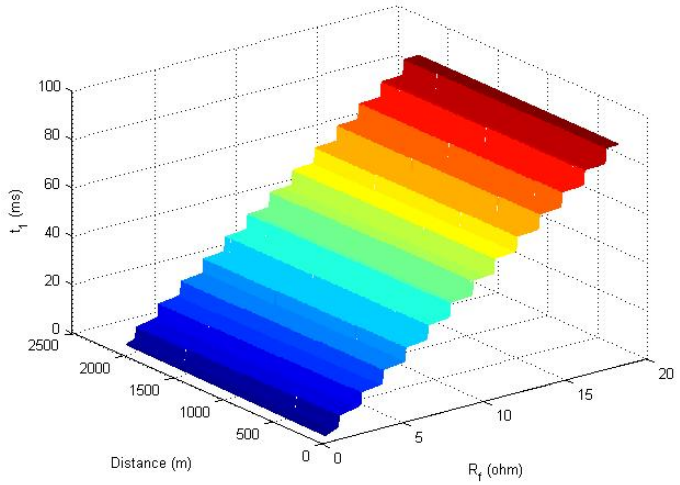

Figure 4.23: Influence of fault resistance R_f and distance x on the stage 1 time t_1 (ms).

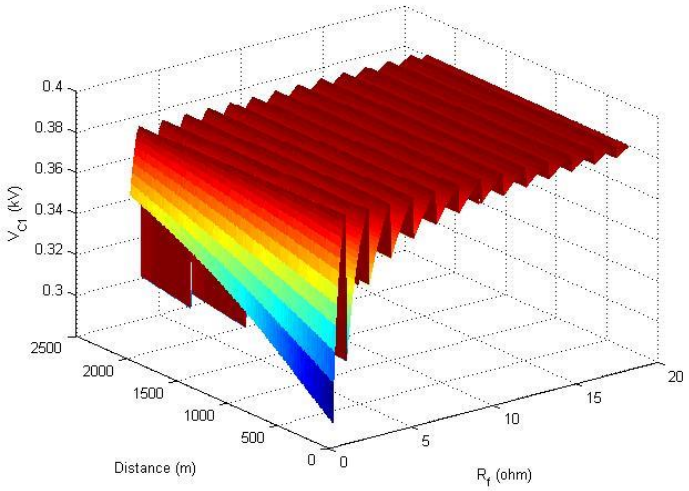

Figure 4.24: Influence of fault resistance R_f and distance x on the stage 1 DC-link capacitor positive voltage at $t_1 - v_{C1}$ (kV).

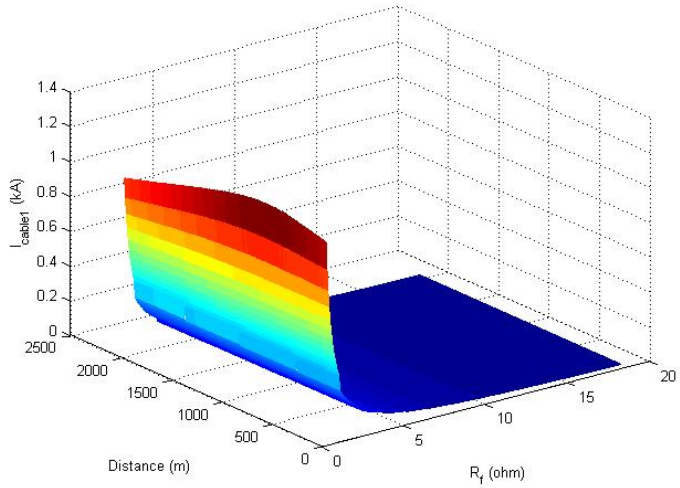

Figure 4.25: Influence of fault resistance R_f and distance x on the stage 1 cable current at $t_1 - i_{cable1}$ (kA).

$$\begin{cases} v'_{C,mea} = A_1 e^{p_1 t_{1,mea}} + A_2 e^{p_2 t_{1,mea}} \\ i_{cable,mea} = A_1 p_1 e^{p_1 t_{1,mea}} + A_2 p_2 e^{p_2 t_{1,mea}} \\ t_{1,mea} \quad (when \quad v'_{C,mea} \le v_{g\,a,b,c}) \end{cases} \Rightarrow \begin{cases} R_{total} = R_f + r \cdot x \\ L_{total} = l \cdot x \end{cases} \Rightarrow \begin{cases} R_f \\ x \end{cases} \tag{4.22}$$

For DC cables, assume per meter resistance and inductance are r and l respectively. With a given r-l ratio of the cable, the grounding resistance R_f and distance x can be found, if the resistance and inductance of other parts of the circuit can be neglected, such as those of IGBTs and diodes.

The calculation to find the location of the cable ground fault (4.22) is assessed using relative errors under different conditions: various ground resistances and fault distances, different operating conditions including system protection operation.

1) Distance Estimation under Various Ground Resistances and Fault Distances:

The simulated ground resistances are 0.1, 0.2, 0.5, 1, 5, and 10Ω. VSI and cable π-model parameters are the same as before. The rectifier side is tripped immediately at the occurrence of the fault, with the IGBTs blocked instantly at the same time. This gives the best stage 1 calculation to test the accuracy of the location estimate. Fault distance ranges from 500m to 3000m.

The calculated distance and ground resistance from (4.22) are expressed as relative errors (Tables 4.7 and 4.8). Due to the small inductance compared with large ground resistances, the calculation errors for distances increase when ground resistance dominates the system response. That is also why the resistance evaluation has much lower errors in Table 4.8.

Table 4.7: Estimation Relative Error (%) of Ground Fault Distance

Distance	R_f=0.1Ω	R_f=0.2Ω	R_f=0.5Ω	R_f=1Ω	R_f=5Ω	R_f=10Ω
500 m	-1.172	-1.558	-6.258	-21.642	99.998	99.999
1000 m	1.329	1.611	4.264	15.114	288.04	685.714
1500 m	2.7693	3.1307	5.7093	17.086	257.14	614.29
2000 m	0.3395	0.3695	0.5715	1.4695	20.6695	51.4305
2500 m	1.5072	1.5072	1.6644	2.6916	21.15	42.8572
3000 m	-3.8013	-3.6320	-3.3653	-3.4583	6.6917	42.857

Table 4.8: Estimation Relative Error (%) of Ground Fault Resistance

Distance	R_f=0.1Ω	R_f=0.2Ω	R_f=0.5Ω	R_f=1Ω	R_f=5Ω	R_f=10Ω
500 m	1.2	0.4	0.32	0.55	0.79	0.4
1000 m	-1.6	-0.5	-0.22	-0.66	-2.61	-4.014
1500 m	-6.0	-2.4	-0.72	-1.15	-4.404	-5.367
2000 m	-0.6	-0.2	-0.04	-0.09	-0.464	-0.586
2500 m	-4.4	-1.8	-0.44	-0.26	-0.596	-0.614
3000 m	13.5	5.55	1.40	0.54	-0.22	-0.746

The measurement time t_1 used for calculation is listed in Table 4.9, which also shows that the dominant influence of a large resistance on the system time-response. With large ground resistance, the time response requirement for the DC switchgear system is not critical (in milliseconds even for the smallest ground resistance condition). This is plenty time for DC solid-state CB (SSCB) to operate.

Table 4.9: Time Point Used for Calculation with Fault Resistance Variation (ms)

Distance	R_f=0.1Ω	R_f=0.2Ω	R_f=0.5Ω	R_f=1Ω	R_f=5Ω	R_f=10Ω
500 m	2.36	2.76	3.68	9.12	24.72	51.14
1000 m	2.84	3.12	3.88	9.70	24.94	51.18
1500 m	3.14	3.36	4.04	9.76	30.62	51.22
2000 m	3.40	3.60	4.20	9.82	30.62	51.24
2500 m	3.64	3.80	4.38	9.88	30.64	51.26
3000 m	3.80	3.98	4.54	9.92	30.66	51.36

In Table 4.7, when increasing R_f, the calculation error for distance increases dramatically, however, most fault resistance errors are still within 5 %. Therefore the evaluated ground resistances are used in a single-iteration to improve the error. From (4.18), considering when the estimated R_f is large, $i_{(flt)} \approx i_{(n)}$, then

$$\hat{x} = \frac{v_{(n)} - R_f i_{(n)}}{v_{(n)} - v_{(r)}} d \tag{4.23}$$

It needs to be noted that the errors in R_f are partially because of the high error in distance. Therefore, by choosing a lower $i_{(n)}$ measurement value in (4.23), the R_f error at distance can be reduced, hence an improved $\hat{x}$ can be obtained. The improved distance results are listed in Table 4.10.

Table 4.10: Improved Ground Distance Estimation Expressed as a Relative Error (%)

Distance	R_f=0.1Ω	R_f=0.2Ω	R_f=0.5Ω	R_f=1Ω	R_f=5Ω	R_f=10Ω
500 m	-0.084	-0.075	-0.131	-0.228	-2.593	-7.823
1000 m	-0.016	-0.020	-0.020	0.010	1.390	7.490
1500 m	-0.013	-0.027	-0.040	0.053	0.520	2.787
2000 m	-0.035	-0.040	-0.040	-0.045	0.125	0.795
2500 m	-0.004	-0.004	-0.008	-0.012	0.076	0.400
3000 m	-0.253	-0.243	-0.230	-0.230	-0.187	0.377

Now the improved errors are almost all within 2% tolerance. If the relay setting uses 10% error tolerance for protection tripping, e.g. for most strict DC bus faults, this is accurate enough. If this is not the case, another iteration can be performed to further improve the estimate. The accuracy of calculation also depends on the initial guess values for solution of (4.22). Operational experience or prior simulation results can then be used to initialise the calculation.

The iteration requires continuous monitoring of system status and data recording equipment. Reliable measurement, monitoring and sensor devices are required for practical application.

2) Distance Estimation under Different Operating Conditions:

The aforementioned analysis is based on ideal operation with immediate blocking of the IGBTs and source side tripping at the instant the fault occurs. The fault resistance and distance estimation is now performed with the IGBT blocking function at a threshold current limit (2.0 p.u.) and with the possibility of slow tripping of the source side. The system performance under different conditions is compared with a fault distance of 1 km and 0.5 Ω fault resistance. The following four cases are considered:

Case I: IGBTs and source side are immediately blocked and tripped, respectively;

Case II: The IGBTs are blocked immediately with source side tripping after an ac CB operation period of 20 ms;

Case III: The source side still trips immediately, IGBTs are blocked once they reach a threshold current limit (2.0 p.u.);

Case IV: IGBTs are blocked once they reach their current limit (2.0 p.u.); source side trips after the 20 ms switchgear period.

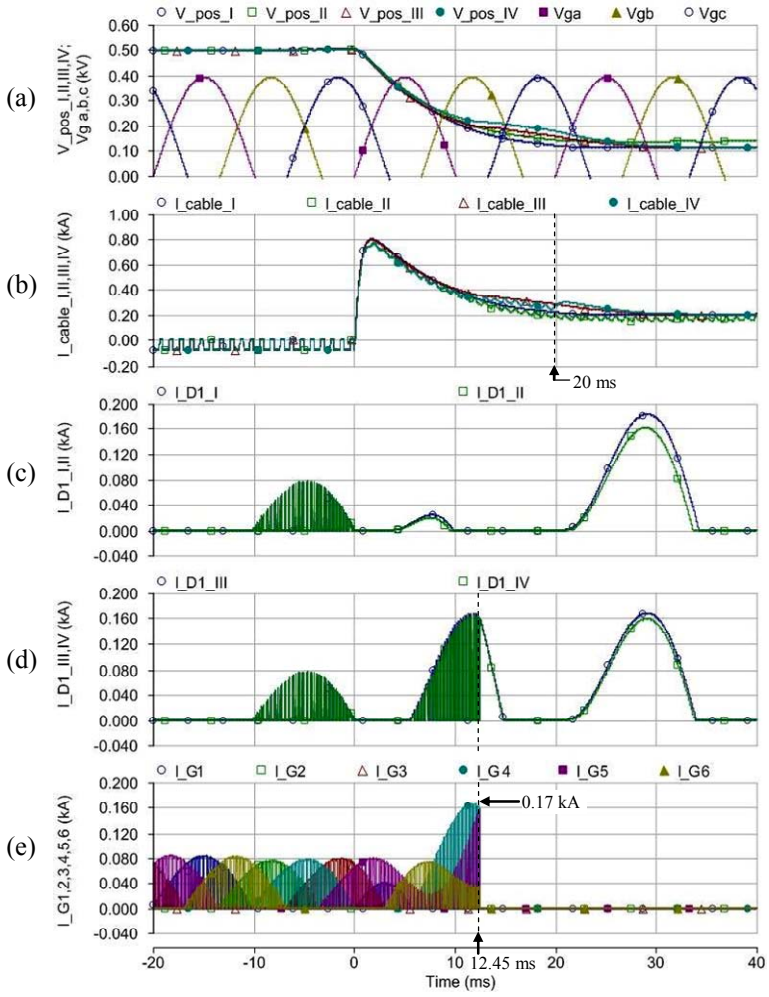

Figure 4.26: Fault location measurement under different operation conditions: (a) DC-link positive voltages for *Case I*, *II*, *III* and *IV* $v_{\_pos\_I,II,III,IV}$ (kV), and grid side three-phase voltages $v_{g\,a,b,c}$ (kV); (b) cable currents $i_{\_cable\_I,II,III,IV}$ (kA); (c) diode current $i_{\_D1\_I,II}$ (kA); (d) diode current $i_{\_D1\_III,IV}$ (kA); (e) IGBT currents $i_{\_G1,2,3,4,5,6}$ (kA).

Simulation results (Figures 4.26 and 4.27) show the difference between the four operating conditions. Without source side tripping, the pulsed DC current still feeds into the negative cable which results in the ripple of cable currents (*Case II* and *IV*).

For *Case III* and *IV*, the VSI-IGBTs are blocked after 12.45 ms at 2 p.u. (0.17 kA). When any IGBT detects an overcurrent higher than 2.0 p.u., all the IGBTs are blocked at the same time. The time instants used for fault location are detailed in Figure 4.27 (indicated with an "×"). The estimated fault resistance and distance under different conditions are listed in Table 4.11, with values obtained through one modifying iteration. Although the results are similar, *Case II*, *III*, and *IV* yield higher percentage errors. This is due to the much smaller inductance relative to the resistance: 0.28×10^{-3} compared to 0.5+0.06. However, using the iterative process can reduce this calculation error to well below 5%.

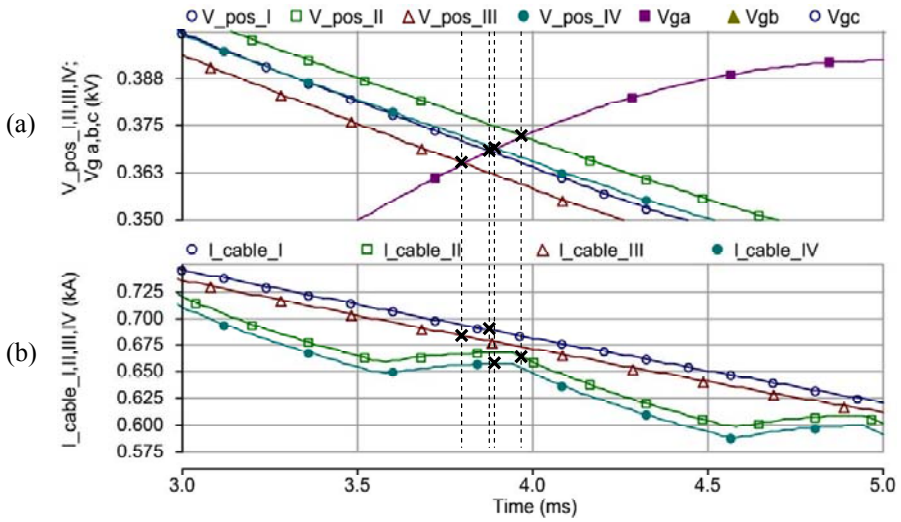

Figure 4.27: Zoomed fault location measurement under different operation conditions: (a) DC-link positive voltages for *Case I*, *II*, *III* and *IV* $v_{\_pos\_I,II,III,IV}$ (kV), and grid side three-phase voltages $v_{g\ a,b,c}$ (kV); (b) cable currents $i_{\_cable\_I,II,III,IV}$ (kA).

Table 4.11: Estimated Fault Resistance and Distance under Various Operating Conditions

Cases	Fault Resistance R_f (Ω)	Fault Distance x (m)	1-Iteration Distance $\hat{x}$ (m)	Fault Resistance Error (%)	Fault Distance Error (%)	1-Iteration Distance Error (%)
Case I	0.4989	1042.64	999.80	-0.22	4.264	-0.020
Case II	0.5203	1175.50	994.18	4.06	17.55	-0.582
Case III	0.5090	751.857	978.06	1.80	-24.8143	-2.194
Case IV	0.5330	846.786	993.56	6.60	-15.3214	-0.644

For fast time-response DC protection devices, if the main protection and backup coordination are capable of securely protecting the system, at the protection stage, there is no need to estimate what the exact distance is to the fault point. The evaluated distance is sufficient for a relay decision to effectively protect the system. Therefore, the accuracy of evaluation can be flexible for different fault protection device requirements. For example, even if the error is larger than 2% for *Case III* after one iteration in Table 4.11, this may still be enough for effective protection judgment. More accurate location can be acquired with iterations of the calculations, or by applying offline approaches.

4.7 Conclusion

DC system protection for wind farms is a new area primed by the potential development of multi-terminal DC wind farms. In this chapter, internal DC faults are listed and analysed in detail, including the most critical short-circuit fault and cable ground faults. The overcurrent and DC voltage drop characteristics can instruct DC switchgear relay design and selection. The study of common VSC and cable circuit fault can be used for most VSC-based DC topologies. A detailed protection design and relay coordination method is proposed, with a diode clamping method for small-scale systems where DC CBs are not economically feasible. Simulation results show that the proposed methods are effective for system protection. It is easier to locate a short-circuit by measuring reference voltages than to locate a ground fault which may have a relatively large impedance. Therefore, a fault location method is proposed for ground faults with analysis and simulation provided under various fault distances, resistances and operating conditions. A method using an additional single-iteration is proposed and is shown to improve the accuracy of the distance and resistance estimate.

The transmission system can be meshed to enhance the reliability but this is a challenge for DC protection and relay design. Although expensive, it is still necessary to have DC CBs for a power transmission system. There has been much research about the design of fully-functioned economical DC CBs. In the future,

this would not be a limitation of DC power system development. The focus of this chapter has been a radial small-scale DC wind farm, while the conclusions may extend, suitably modified, to large-scale DC wind farms. The challenges of protecting meshed large-scale DC wind farm networks will be investigated in Chapter 5.

4.8 References

[4.1] P. Bresesti, W. L. Kling, R. L. Hendriks, and R. Vailati, "HVDC connection of offshore wind farms to the transmission system," *IEEE Trans. Energy Convers.*, vol. 22, no. 1, pp. 37-43, Mar. 2007.

[4.2] C. Meyer, M. Hoing, A. Peterson, and R.W. De Doncker, "Control and design of DC grids for offshore wind farms," *IEEE Trans. Ind. Appl.*, vol. 43, no. 6, pp. 1475-1482, Nov./Dec. 2007.

[4.3] A. Prasai, J. S. Yim, D. Divan, A. Bendre, and S. K. Sul, "A new architecture for offshore wind farms," *IEEE Trans. Power Electron.*, vol. 23, no. 3, pp. 1198-1204, May 2008.

[4.4] D. Jovcic and N. Strachan, "Offshore wind farm with centralised power conversion and DC interconnection," *IET Gener. Transm. & Distrib.*, vol. 3, no. 6, pp. 586-595, Jun. 2009.

[4.5] P. M. Anderson, *Power system protection*. New York: IEEE Press, 1999.

[4.6] X. Yang, M.-S. Choi, S.-J. Lee, C.-W. Ten, and S.-I. Lim, "Fault location for underground power cable using distributed parameter approach," *IEEE Trans. Power Sys.*, vol. 23, no. 4, pp. 1809-1816, Nov. 2008.

[4.7] M.-S. Choi, S.-J. Lee, D.-S. Lee, and B.-G Jin, "A new fault location algorithm using direct circuit analysis for distribution systems," *IEEE Trans. Power Del.*, vol. 19, no. 1, pp. 35-41, Jan. 2004.

[4.8] X. Liu, A. H. Osman, and O. P. Malik, "Hybrid travelling wave/boundary protection for monopolar HVDC line," *IEEE Trans. Power Del.*, vol. 24, no. 2, pp. 569-578, Apr. 2009.

[4.9] L. Xu, B. R. Andersen, and P. Cartwright, "VSC transmission system operating under unbalanced network conditions – analysis and control design", *IEEE Trans. Power Del*, vol. 20, no. 1, pp. 427-434, Jan. 2005.

[4.10] L. Xu, L. Yao, M. Bazargan, and A. Yan, "Fault ride through of large offshore wind farms using HVDC transmission," in *Proc. 2009 IEEE Power Tech Conf.*, Bucharest, Romania, 28 Jun. – 2 Jul., 2009.

[4.11] M. E. Baran and N. R. Mahajan, "DC distribution for industrial systems: opportunities and challenges," *IEEE Trans. Ind. Appl.*, vol. 39, no. 6, pp. 1596-1601, Nov./Dec. 2003.

[4.12] M. E. Baran and N. R. Mahajan, "Overcurrent protection on voltage-source-converter-based multiterminal DC distribution systems," *IEEE Trans. Power Del.*, vol. 22, no. 1, pp. 406-412, Jan. 2007.

[4.13] F. Blaabjerg and J. K. Pederson, "A new low-cost, fully fault-protected PWM-VSI

inverter with true phase-current information," *IEEE Trans. Power Electron.*, vol. 12, no. 1, pp. 187-197, Jan. 1997.

[4.14] L. Tang and B. T. Ooi, "Protection of VSC-multi-terminal HVDC against DC faults," in *Proc. IEEE 33rd Annual Power Electronics Specialists Conf.*, vol. 2, pp. 719-724, Cairns, Queensland, Australia, 23-27 Jun. 2002.

[4.15] L. Tang and B. T. Ooi, "Locating and isolating DC faults in multi-terminal DC systems," *IEEE Trans. Power Del.*, vol. 22, no. 3, pp. 1877-1884, Jul. 2007.

[4.16] D. Xiang, R. Li, P. J. Tavner, and S. Yang, "Control of a doubly fed induction generator in a wind turbine during grid fault ride-through," *IEEE Trans. Energy Convers.*, vol. 21, no. 3, pp. 652-662, Sep. 2006.

[4.17] I. Erlich, J. Kretschmann, J. Fortmann, S. Mueller-Engelhardt, and H. Wrede, "Modeling of wind turbines based on doubly-fed induction generators for power system stability studies," *IEEE Trans. Power Syst.*, vol. 22, no. 3, pp. 909-919, Aug. 2007.

[4.18] M. E. Haque, M. Negnevitsky, and K. M. Muttaqi, "A novel control strategy for a variable speed wind turbine with a permanent magnet synchronous generator," in *Proc. Ind. Appl. Society Annual Meeting*, Hobart, Australia, 5-9 Oct. 2008.

[4.19] A. D. Hansen and G. Michalke, "Multi-pole permanent magnet synchronous generator wind turbines' grid support capability in uninterrupted operation during grid faults," *IET Renewable Power Gener.*, vol. 3, no. 3, pp. 333-348, Sep. 2009.

[4.20] H. A. Darwish, A.-M. I. Taalab, and M.A. Rahman, "Performance of HVDC converter protection during internal faults," in *Proc. IEEE Power Eng. Society General Meeting*, pp. 57-59, Montreal, Quebec, Canada, 18-22 Jun. 2006.

[4.21] M. J. Mousavi and K. L. Butler-Purry, "A novel condition assessment system for underground distribution applications," *IEEE Trans. Power Sys.*, vol. 24, no. 3, pp. 115-1125, Aug. 2009.

[4.22] S. R. Mendis, M. T. Bishop, J. C. McCall, and W. M. Hurst, "Overcurrent protection of capacitors applied on industrial distribution systems," *IEEE Trans Ind. Appl.*, vol. 29, no. 3, pp. 541-547, May/Jun. 1993.

[4.23] K. Xing, F. C. Lee, J. S. Lai, T. Gurjit, and D. Borojevic, "Adjustable speed drive neutral voltage shift and grounding issues in a DC distribution system," in *Proc. IEEE Ind. Appl. Society Annual Meeting*, New Orleans, Louisiana, 5-9 Oct. 1997.

[4.24] C. Abbey, W. Li, L. Owatta, and G. Joós, "Power electronic converter control techniques for improved low voltage ride through performance in WTGs," in *Proc. 37th IEEE Power Electronics Specialists Conference*, vol. 1, pp. 422-427, Jeju, Korea, 18-22 Jun. 2006.

[4.25] S. Castagno, R. D. Curry, and E. Loree, "Analysis and comparison of a fast turn-on series IGBT stack and high-voltage-rated commercial IGBTs," *IEEE Trans. Plasma Science*, vol. 34, no. 5, pp 1692-1696, Oct. 2006.

Chapter 5

Protection Coordination of Meshed VSC-HVDC Transmission Systems for Large-Scale Wind Farms

5.1 Introduction

The Supergrid is a conceptual and ambitious European development to assist the integration of renewables and European connectivity [5.1], [5.2]. It is a high-voltage meshed DC grid that connects together a number of wind farms and onshore substations in participating European countries. High-voltage direct-current (HVDC) technology based on voltage-source converters (VSCs) is a flexible technology that could realise the Supergrid concept even with some weak AC system connections [5.3]. The meshed topology aims to enhance system reliability, which is requisite for transmission networks with a large contribution from offshore wind power. Networks with loops are common in traditional AC transmission power grids, because they are relatively economical compared to the double-line systems and more reliable than radial systems without backup. The potentially large capacity of wind power integrated into AC grids requires the transmission systems to be much more reliable due to its influence on the whole electricity system. If the concept of Supergrid progresses to reality for multiple wind farm connection and integration to onshore systems, issues related to the loop topology should be considered in advance, especially for the untried high-power DC scenario.

Due to the lack of existing high-power DC systems and associated operational experience, currently there is no developed protection scheme that can be used for the VSC-based high-power DC scenario. In order to help solve the DC system

protection problem, radial multi-terminal DC VSC-based overcurrent protection for wind power generation is discussed in Chapter 4, which will form the basis of this chapter. As mentioned, there is little work on VSC-based DC system switchgear configuration for protection. However, for large-scale offshore DC wind farms with HVDC power transmission, proper DC switchgear configuration is essential. Therefore, this chapter will further explore the protection design of meshed networks at the transmission level. Former fault analysis of VSC-cable systems will be summarised and applied. The DC switchgear technology is assumed to be a uni-directional current-blocking power electronic circuit breaker (CB). The key protection issues to realise protection reliability and selection of this meshed DC network are defined and discussed with a consequent CB tripping strategy.

This chapter is organised as follows. In Section 5.2, the multi-terminal DC wind farm topology is introduced along with possible topologies. A typical network section is proposed for study. DC fault characteristics are summarised and applied in Section 5.3. With fault current frequency analysis, the DC cable modelling issue is discussed with comparisons via simulation. DC switchgear options and their allocation are presented in Section 5.4 followed by detailed protection strategy design. Illustrative examples and PSCAD/EMTDC simulations are provided in Section 5.5.

5.2 Multi-terminal Meshed DC Wind Farm Network

Nowadays, multi-terminal DC wind farm topologies that have been researched are mainly radial [5.4], [5.5]. However, a meshed connection is required for future reliable HVDC power transmission [5.2]. There is currently no reported work about the protection of such systems.

5.2.1 Meshed Multi-terminal DC Wind Farm Topology

The topology with loops is commonly used in traditional AC power transmission systems because of its balance between economic costs and reliability. The high-power DC transmission network will need to achieve the highest standard of reliability and availability. If the concept of Supergrid can be realised for multiple

offshore wind farm connection and integration to different onshore AC grids, the protection issues related to the meshed system must be addressed. For the collection grid, the reliability can also be enhanced by introducing redundant cables (discussed in Chapter 6), but usually, the system will operate in open-loop which leaves all the redundant cables as backup in case of faults in cables or devices used during normal operation. If many wind farms are connected together with multiple onshore connections, the transmission system should be optimal to have a loop, or even meshed. Power flows in this network can be much more flexible with a more even utilisation of cable resources, which is one of the most expensive investments. However, this meshed topology makes the protection relay coordination and switchgear system much more complex.

One main problem for a complex loop/meshed system is that the power flow cannot be predicted accurately. The power flow varies as the system condition changes, for example, wind speed oscillations that result in power fluctuations, or possible power flow direction changes due to switch-in or -out of wind farms. Special attention to the loop cables between wind farms is required because of the bi-directional load flow on them. Therefore the possible normal power flow oscillations and direction changes need to be excluded to make the relay setting simpler and accurate in operation. Apart from that, mature protection and relay coordination techniques of meshed AC distribution and transmission systems [5.6]-[5.8] can be analysed and developed for application to this DC system.

5.2.2 Supergrid Section for Protection Test Study

The DC topology investigated is a multi-terminal VSC-HVDC system connecting large-scale wind farms. A typical section of this meshed DC Supergrid with possible switchgear allocation for protection test is shown in Figure 5.1. All the AC/DC rectifiers and DC/AC inverters are sinusoidal pulse-width-modulation (SPWM) VSCs connected with DC cables (lengths as shown). No more detailed DC wind farm collection grids are shown, only the transmission system with converters or centralised step-up DC/DC converters illustrated as VSCs. Each wind farm is represented by an equivalent wind turbine-permanent magnet synchronous generator

(PMSG) set in which maximum-power-point-tracking (MPPT) is fulfilled by the AC/DC VSC. The rectifier VSC and voltage source inverter (VSI) control schemes are that of a single PMSG direct-driven wind power generation system [5.9]. The four wind farms are all of 300 MW rating each – 1200 MW in total – and connected to a ±100kV DC loop with two parallel cables to two separate onshore AC grids.

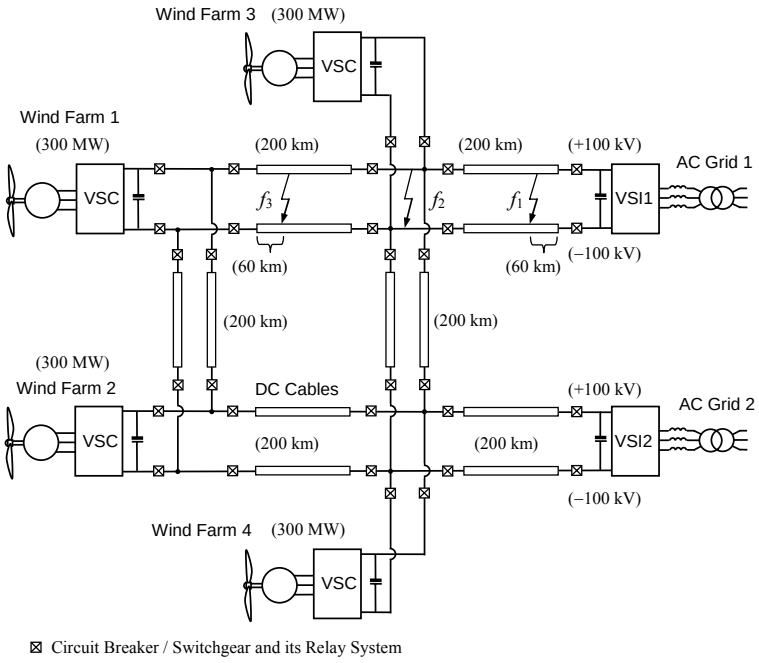

Figure 5.1: A typical section of multi-terminal DC transmission system for Supergrid.

This example transmission section is made according to the following assumptions: 1) Each node has a connection to a wind farm or onshore inverter platform to AC grid substation; 2) The loop here is symmetrical with connections to two AC grids; 3) There might not be real DC bus conductors allocated in an offshore environment, but the node with more than two connections is considered to be a DC bus where bus faults can occur (shown as fault f_2 in Figure 5.1).

This network is simplified to a single-line diagram, Figure 5.2, for node/cable numbering and possible power flow directions indicated with dotted arrows. The Cables 1, 3, 4 and 5 are defined as loop cables; while Cables 2 and 6 are radial cables. It is the bi-directional loop Cables 1, 3, 4, 5 that complicate the protection coordination.

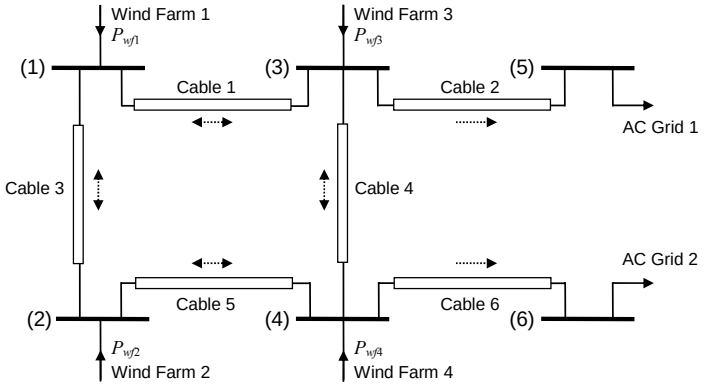

Figure 5.2: Single-line diagram shows system nodes, cable connections, and power flow directions.

IGBT-based VSCs have freewheel diodes – as shown in Figure 5.3(b) – which will be destroyed by the overcurrent that occurs during DC-link discharge. Fault tolerant converters can be applied to avoid allocating a large number of DC CBs. The main idea is to replace those passive diodes with self turn-off power electronic devices, like another IGBT/diode series branch (Figure 5.3(c)) or emitter turn-off devices (ETOs) [5.10] (Figure 5.3(d)). Furthermore, a thyristor-based dedicated high-power DC/DC transformer that can isolate fault currents is proposed in [5.11]. However, in terms of a network, this means all the converters need to be totally immune from DC faults. During the development of the network, at this stage, with mostly conventional VSCs, it is economically infeasible. Therefore, protection scheme design is still a necessity to the development of multi-terminal DC transmission networks.

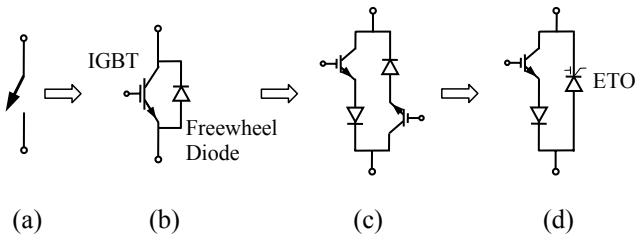

Figure 5.3: Illustration of VSC switch configuration for fault tolerant function: (a) switch symbol; (b) traditional IGBT/diode switch; (c) bi-directional IGBT/diode-series fault tolerant switch; (d) bi-directional IGBT/ETO parallel fault tolerant switch.

5.3 DC Fault Analysis for Large-Scale Meshed Systems

Detailed fault analysis of a VSC-based radial system using a π-model for the cable is reported in Chapter 4 and applied in this chapter. The faults are mainly short-circuit faults and ground faults both on positive and negative cables. The IGBTs of VSCs can be blocked for self-protection during faults, leaving the reverse diodes exposed to the DC-link discharge overcurrent. To solve the complete response of this nonlinear circuit, different time periods are defined with expressions of both the DC-link voltage collapse and cable overcurrent. There are three stages established for this nonlinear system. The frequency characteristics are provided in Table 5.1 for the following cable modelling comparison.

Table 5.1: Frequency of Fault Currents

Fault condition	Phase	Description	Frequency
Short-circuit fault	I	DC-link Capacitor Discharging, Natural Response	$\omega^2 = \frac{1}{LC} - \left(\frac{R}{2L}\right)^2$
	II	Cable Inductance Discharging, Natural Response	N/A
	III	Grid Side Current Feeding, Forced Response	$\omega^2 = \frac{1}{LC} - \left(\frac{R}{2L}\right)^2$
Ground fault	I	Transient Phase, Natural Response	$\omega_s = 2\pi f_s$
	II	Steady-state Phase, Forced Response	$\omega_s = 2\pi f_s$

f_s – the synchronous time frequency; C – DC-link capacitance; R, L – the equivalent resistance and inductance for fault-length cable.

DC bus faults are the same in essence for circuit analysis but different for relay coordination, especially for the uni-directional current-blocking CBs. The distance evaluation protection method proposed in Chapter 4 is used here as well, with a new coordination strategy presented for meshed topology.

5.3.1 Appropriate Cable Modelling for DC Fault Analysis

For large-scale offshore wind farms with HVDC power transmission, detailed and appropriate DC cable models are required for accurate transient analysis. In Chapter 4, the VSC DC fault analysis is based on a lumped π-equivalent cable model. However, no fault current calculation with detailed cable model is analysed. In this

section, the multi-layered underground (or submarine) distributed cables are analysed because they are used in practice for large-scale onshore/offshore wind power integration. Overhead line models are not investigated.

1) Existing Cable Models

There are several cable models available for circuit analysis and computer simulation. Theoretically, the distributed single-conductor cable model is represented by partial derivative equations in time and distance as the original mathematical model. Furthermore, to separate distance and time dependency, the travelling wave model analysis [5.12] is performed for steady-state solution under ideal sinusoidal signals.

For transient response simulations, there are four common models. The most common, and simple, is the π-equivalent model. The Bergeron model is a progression of the simple π-model. It accurately represents the distributed L and C, but with a lumped R to simulate cable power loss. They are accurate at a specified frequency and are suitable for studies where a certain frequency is important (e.g., for AC relay studies) [5.13]. The frequency dependent model in mode represents the frequency dependence of all parameters (not just at the specified frequency as in the Bergeron model). The problem of a frequency dependent transformation matrix can be overcome by formulating the model directly in the phase domain (without diagonalisation) [5.13], which results in the frequency dependent phase model. It also represents the frequency dependence of all parameters as in the mode model, and produces the most accurate transient responses.

Therefore, the choice of cable model mainly depends on the frequency range of the study. Appropriate cable models will be chosen for the DC fault protection analysis with simulation comparison as verification of the former π-model analysis in Chapter 4.

2) Fault Current Frequency

Traditional fault analysis and solutions for AC distribution and transmission systems are well understood and have led to mature technologies. To clarify the analysis for traditional AC system fault conditions, the capacitor discharging part in the AC fault analysis is introduced here as a reference.

In the IEEE Standard 551 (2006) – "Recommended practice for calculating short-circuit currents in industrial and commercial power systems" [5.14] – the normal capacitor discharging currents from power factor correction capacitors or harmonic filters have been considered in ANSI or IEC calculation procedures. Even for conservative models with larger-sized capacitors, the result is still that capacitor discharge currents will have no effect on circuit breaker fault clearing operations. Therefore the Standard still does not recommend that capacitors be added to system simulations with detailed cable model for breaker duty calculations. Because of the low capacitance value, the stresses associated with capacitor discharge currents have high-frequency components. Hence the simulations provided are with the most detailed model – frequency dependent model in phase – for breaker duty determinations.

However, from the analysis of Chapter 4, with a large DC-link capacitor, the frequency is much lower for high power DC systems – in terms of several Hz. Therefore if appropriate simple π-model parameters are chosen, this will be precise enough for fault current calculation. To test the accuracy of the π-model for fault transient response simulation, the first phase of DC-link capacitor discharge is simulated using PSCAD/EMTDC. The most detailed frequency dependent phase model in PSCAD/EMTDC is applied as comparison, which includes all the conductor layers: copper core, sheath, and armour. Detailed cable physical data and underground environment data can be found in [5.15]. The corresponding lumped π-model parameters for simulation comparison are listed in Table 5.2. An ideal DC voltage source is connected to a resistance load through cables. A short-circuit fault is applied across the load to produce a transient response in the system.

Table 5.2: Cable Π-Model Parameters

Parameter	Value	Parameter	Value
Resistance *r*	0.005 Ω/km	Cable length	15 km
Inductance *l*	0.5 mH/km	DC-link capacitor	10 mF
Rated voltage	200 kV	Initial current	4 kA

With appropriate *RLC* parameters (calculated according to [5.16]), the π-model simulation results are close enough to the accurate cable model as shown in Figure

5.4(a). Figure 5.4(b) shows some minor current differences between the two simulation results. This is due to the various frequency components in the overcurrent which see a frequency-independent set of π-model parameters resulting in calculation error. However, the difference is only perceptible towards the end of the fault. The first wave front can be fitted exactly the same as that with a detailed model, which is adequate for accurate protection relay setting and configuration.

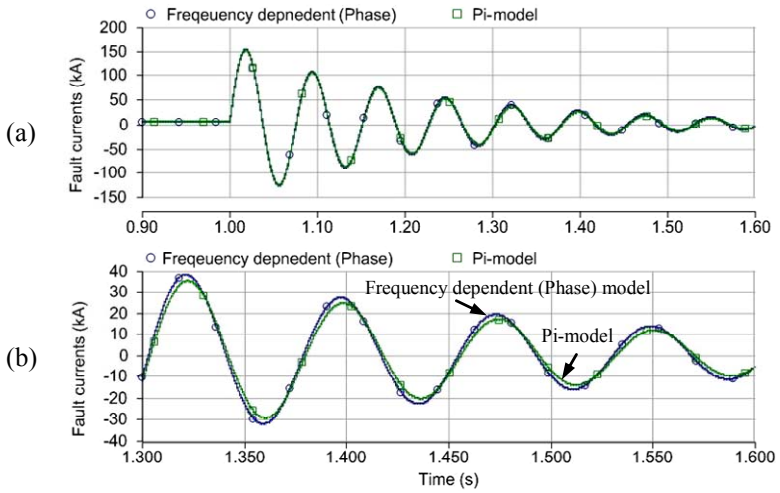

Figure 5.4: DC fault current simulation comparison with frequency dependent phase model and π-model.

5.3.2 DC Bus Fault

When the fault distance estimated from the relay point is zero, the fault can be considered as occurring on the DC bus (which is at the same electrical point as the relay in terms of the equivalent circuit), an example is shown in Figure 5.1 (fault f_2). In Chapter 4, DC bus faults were not analysed specifically in a radial system. Since there is no node with more than one output connection in a radial system, for CB coordination, DC bus faults are the same as cable faults. However, for meshed systems, a DC fault is severe especially at a location with multiple output connections, i.e. the DC bus. That means at least three CBs (one for input-side and two for output-side) are involved and the coordination for uni-directional DC CBs is necessary for their selective operation. This design process will be discussed in the following section.

5.4 Protection Scheme for Meshed DC Systems

According to the analysis in Section 5.3, the protection scheme design depends on the fault characteristics and the type of CB applied. The key issue is the strategy of a selective but reliable CB coordination method. The proposed protection coordination is realised by distance evaluation without communication between distant relays. The CB fault tripping requirements are: 1) The DC current and voltage are required to be continuously monitored during system operation. 2) When overcurrent is detected, the equivalent fault distance is evaluated rapidly using a voltage difference comparison method. 3) The assessed distance will be used to compare with the relay pre-set values to decide when and whether to trip the CB or not.

5.4.1 High-Power DC Switchgear Allocation

High-power DC switchgear is still under development with few mature commercial products. The traditional mechanical structured CB used in AC systems cannot be applied due to the slow fault isolation speed and the requirement of zero-crossings in the fault current. Therefore, power electronic devices are used to quickly block fault currents, such as IGBT and gate turn-off thyristors (GTOs). Generally, CBs of this kind are called solid-state CBs (SSCBs). One option includes a paralleled mechanical switch S_p as an auxiliary switch for lower loss during normal operation, a metal-oxide-varistor surge arrester MOV_{CB}, and power electronic blocking device PE_{CB}, Figure 5.5(a). The PE_{CB} block can be a parallel or series topology. Figure 5.5(b) and 5.5(c) realise bi-directional current block functions. Sometimes, a series inductance L_{CB} and a switch S_s are used as a fault current limiter and to provide an obvious electrical isolation point for the network operator, i.e. as a disconnector. This CB topology can be seen as device redundancy to enhance reliability, as a comparison with topology redundancy which will be discussed in Chapter 6.

The technical challenges for high-power DC CBs are the current isolation capability of power electronic devices, their high costs and their losses. Although some fault tolerant converters can reduce the allocation of CBs, as long as the development of this DC network includes traditional VSCs, reliable system protection relies on DC

CBs. At this stage, in terms of device number, it is still economical to allocate DC CBs. Multi-IGBT devices could be used in series or parallel connection to increase the voltage or current ratings, particularly for high-overcurrent situations.

The DC switchgear allocation is illustrated in Figure 5.6 for the six-node test system. Uni-directional current-blocking DC CBs are used. This is a trade-off option considering both economic costs and function. The CB at each cable end has only one IGBT for fault current blocking but the two CBs can cooperate to isolate faults that occur between them on the cable. This requires only half the number of power electronic devices for fault current cut-off compared to the fully functioned bi-directional CBs, with half the loss but with a reduction in functionality. This CB allocation and configuration will influence the coordination strategy design. If bi-directional functionalised CBs are used, the multi-loop coordination strategy of the AC system can be applied to this DC loop protection analysis [5.6], [5.7].

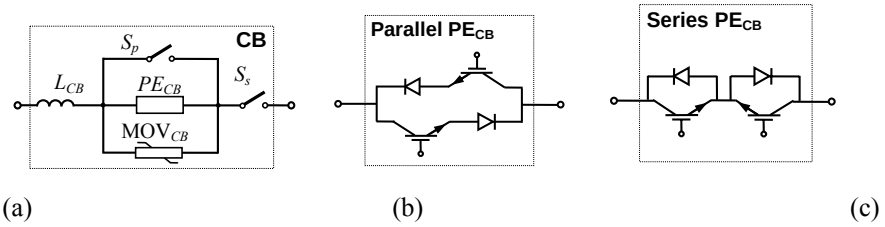

Figure 5.5: A DC CB option: (a) DC CB configuration; (b) parallel connected bi-directional PE block; (c) series connected bi-directional PE block.

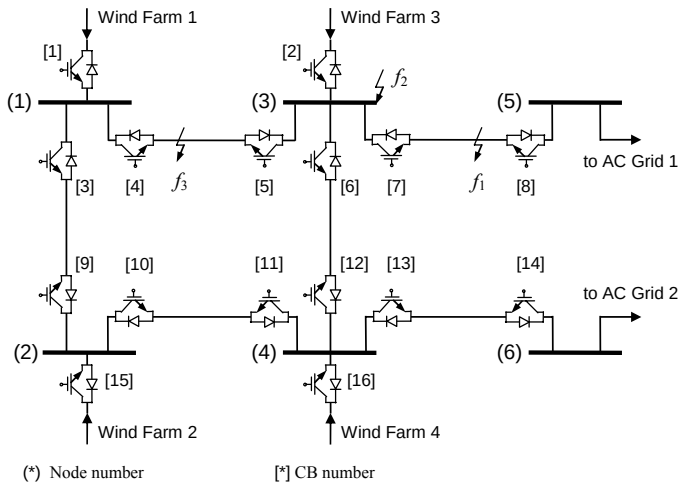

Figure 5.6: DC CB allocation and numbering for relay configuration and coordination.

The operating state of the wind farm depends on the wind resource conditions. The power acquired from a large wind turbine is variable but normally varies over at time period of seconds. Simulation of variable wind speed conditions have been performed using the wind profile shown in Figure 5.7. In the simulation, the whole wind farm is exposed simultaneously to the wind profile which is the most severe case of power flow and current variation on the cable. The wind model applied is from PSCAD/EMTDC with gusts, noise and a rated speed of 12 ms^{-1}. The shear and tower effects which result in a flicker power quality problem [5.17] are not considered. This will not influence the protection system operation.

The results in Figure 5.7 show that: 1) There can be steep current increase and decrease; 2) DC-link voltage fluctuation is not as dramatic as under fault conditions. With many distributed wind-turbines aggregation reduces the fluctuation effect. Hence the power fluctuation due to changes in wind conditions will not influence the relay system performance as long as the rate of change of current is not utilised for fault detection. The DC fault currents are always extreme where overcurrent occurs in milliseconds and is distinct enough from normal fluctuations for fault identification.

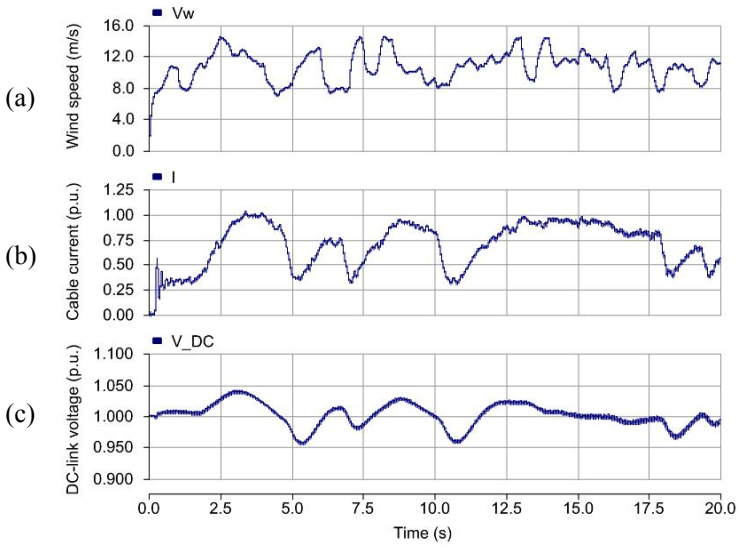

Figure 5.7: DC cable current and voltage responses under wind speed fluctuation: (a) wind speed (ms^{-1}); (b) cable current (p.u.); (c) inverter DC-link voltage (p.u.).

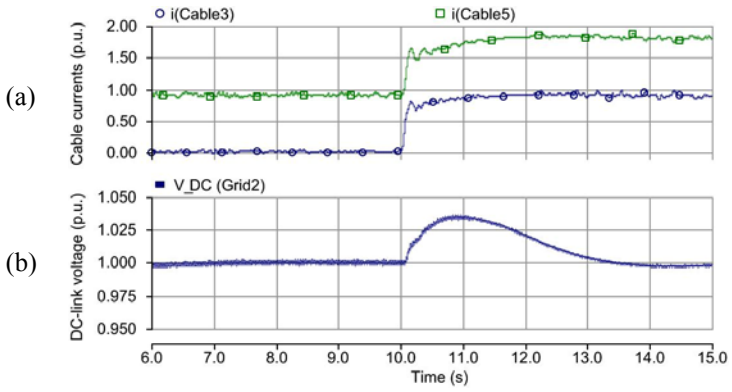

Figure 5.8: DC cable current and voltage responses under sudden power increase: (a) cable currents (p.u.); (b) inverter DC-link voltage (p.u.).

The power flow calculation for this linear system will obey basic physical principles, which will not need a specific algorithm for the convergence of results, like those commonly used for nonlinear AC systems. In this DC system, all the power sources can be calculated separately to estimate current flow according to the superposition theorem. Therefore the theoretical power flow results can be calculated almost instantaneously which is helpful for the real-time decision process. Figure 5.8 shows a power increase due to a change in system operation. There are high rates of change of current in some cables which reinforces the need to not use rate of change of current in the decision making process.

Another issue is the exclusion of current harmonics due to the modulation method of the converters [5.15]. The harmonics are with known high-order frequencies and can be eliminated from the method used to detect faults via frequency detection. Hence, only in the low frequencies given in Table 5.1, current and DC-link voltage amplitude and direction changes will the signals be used to detect fault conditions.

5.4.2 DC CB Relay Coordination Relations

For a very complex multi-loop network, it is necessary to describe the relay coordination relations by definition of the dependency degrees [5.7], [5.8]. The primary protection relay set (PPRS), primary protection dependency degree (PD) and backup protection dependency degree (BD) are defined as functional dependency [5.7].

Protection setting of relay $R_{[x]}$ depends on the relay setting $R_{[i]}$, $R_{[j]}$, …, $R_{[n]}$ to realise coordination. Then $\{R_{[i]}, R_{[j]}, \ldots, R_{[n]}\}$ is called the PPRS. Number n is defined as PD. According to the cooperation principle between primary protective relays and backup protective relays, the protection relay $R_{[2]}$ should cooperate with $R_{[1]}$, i.e., the setting value of $R_{[2]}$ must be calculated in terms of the setting value of $R_{[1]}$. Moreover, the time delay of the backup $R_{[2]}$ must avoid the most serious diode freewheel phase (short-circuit fault phase II in Table 5.1). Analogically, $R_{[3]}$ cooperates with $R_{[2]}$, $R_{[m]}$ cooperates with $R_{[m-1]}$, and $R_{[1]}$ cooperates with $R_{[m]}$ as a loop. Consequently, the cooperation relations among protective relays $R_{[1]}$, $R_{[2]}$, …, $R_{[m-1]}$, $R_{[m]}$ result in a circulation. BD is the number of this relay which can act as backup for others. Table 5.3 shows the PPRS, PD and BD of all the relays in the example section network in Figure 5.6.

Table 5.3: Relay Coordination Relations and Coordination Dependency Degrees

Relay	PPRS	PD	BD	Relay	PPRS	PD	BD
[1]	∅	0	2	[9]	{[1], [4]}	2	1
[2]	∅	0	3	[10]	{[12], [13], [16]}	3	1
[3]	{[10], [15]}	2	1	[11]	{[9], [15]}	2	2
[4]	{[2], [6], [7]}	3	1	[12]	{[2], [5], [7]}	3	2
[5]	{[1], [3]}	2	2	[13]	AC Grid 2	1	2
[6]	{[11], [13], [16]}	3	2	[14]	{[11], [12], [16]}	3	0
[7]	AC Grid 1	1	2	[15]	∅	0	2
[8]	{[2], [5], [6]}	3	0	[16]	∅	0	3

These dependency degrees are used to determine the Minimum loop-Breaking Point Set (MBPS) for multi-loop systems to be broken down to radial systems, then the simple distance coordination method can be carried out to realise selection. If DC/DC isolation transformers are applied [5.11], the system can be automatically separated into radial sub-networks. But this requires reliable DC/DC transformers and additional device costs and power losses will be incurred.

5.4.3 Protection Scheme

The steps of the protection scheme are defined as follows and are illustrated in Figure 5.9.

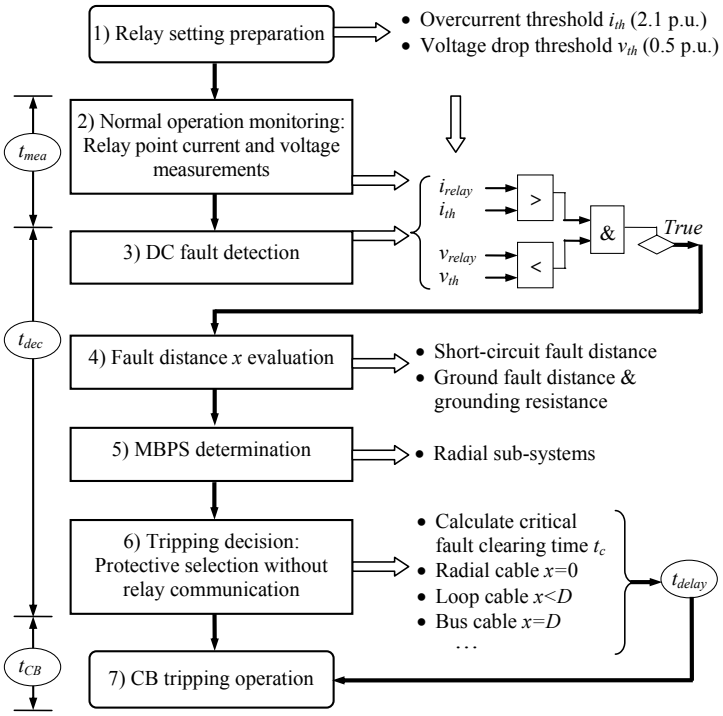

Figure 5.9: The proposed DC meshed network protection scheme.

1) *Relay setting preparation:* At the planning stage, the overcurrent threshold i_{th} and voltage drop threshold v_{th} are set. In this section, i_{th} is chosen as 2.1 p.u. to avoid tripping during normal operation when power flow could be 2.1 p.u. due to a previous CB trip (assume normal operation can be up to 1.05 p.u. for each wind farm). The voltage drop threshold is v_{th} = 0.5 p.u. for the DC-link voltage.

2) *Real-time monitoring:* For each wind resource sampling period (e.g. one second), calculate the system power flows and measure relay point current and voltage amplitudes for each sampling period (e.g. 50 μs) as state monitoring. The measurement equipment should have a small sampling time period to ensure the relays have enough sampling points to deal with fault detection and tripping operation.

3) *Real-time fault detection:* The abrupt change of currents and DC-link voltage collapse are compared with the pre-set threshold values. Practically, this will take at least one current and voltage sampling time-step to complete.

4) *Real-time distance evaluation:* After the fault is detected, the distance calculation is performed using voltage comparison. As proposed in Chapter 4, a reference relay voltage sensor unit (r_i) is equipped for the relative voltage calculation; it is located near the main relay point on the same section of cable, as shown in Figure 5.10, to avoid long distance communication issues. Voltage dividers are used for voltage measurements. The distance between them is known as d, so the fault distance measured from this reference is

$$x = d\,v_{(n)} \big/ \left(v_{(n)} - v_{(r_n)}\right). \tag{5.1}$$

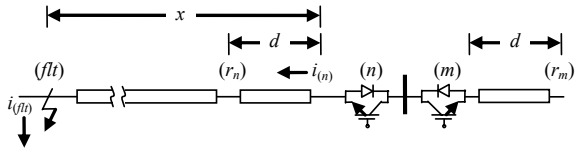

Figure 5.10: Distance evaluation with two voltage divider measurements.

5) *Real-time MBPS determination:* The multi-loop breaking-points are chosen with the BD relation of the minimum distance relay points as the start. Then the system is separated into radial branches with the MBPS.

6) *Tripping decision:* If a fault is detected from step 3), a corresponding relay delay time for the CB will be applied. At this stage a decision is made as to whether the fault is in the protection region of this CB. It will trip after a given delay time as backup protection, or immediately as primary protection. Firstly, the critical time t_c (for short-circuit fault phase II in Table 5.1) is calculated at each relay point as the tripping period upper limit, as proposed in Chapter 4. In respect of the evaluated distance x, the critical time is

$$t_c = \frac{\pi - \arctan\left(V_0 C\omega' / (V_0 C\delta - I_0)\right)}{\omega'} \tag{5.2}$$

where $\omega' = \sqrt{\omega_0^2 / x - \delta^2}$, $\omega_0 = \sqrt{\delta^2 + \omega^2}$, $\delta = R/(2L)$, $\omega^2 = 1/(LC) - [R/(2L)]^2$. C, R, and L are the DC-link capacitance, fault-length DC cable equivalent π-model resistance and inductance respectively. The values of V_0 and I_0 used are from real-time measurement one time-step before the fault detection. This critical time t_c will be used to set the upper limit of relay delay time for backup CBs.

7) *CB tripping operation:* After waiting for the consequent time delay, the CB trips with IGBT block and possible disconnector operation. The total operation time until the fault current is finally extinguished is designated as t_{CB}.

The total protection clearing time includes the measurement time t_{mea}, decision and evaluation time t_{dec}, resulting delay time t_{delay}, and CB time t_{CB}, as shown in Figure 5.9. Again this has to be finished before the appropriate critical time t_c. The selection decision step without relay communication is described in detail as follows.

5.4.4 Protective Selection without Relay Communication

To avoid the use of communication between distant relays, the selection is realised by the following assumptions and measurement allocations.

1) The CBs just connected to one radial cable or a wind farm will operate immediately only when their evaluated distance x is exactly or almost zero. The DC-chopper system across the wind farm DC-link needs to operate to dump all the redundant power. Meanwhile the wind farm needs to be stopped. If x is not zero, it will always wait for a delay time for the primary cable protection to operate and form a possible new power transmission route in the loop.

2) If the CB at one end of the cable detects exactly the cable length D as fault distance, this means the fault has occurred at the DC bus connected to other end of this cable. This CB will trip immediately because the CB near the DC bus cannot block fault current by itself due to the reverse diode of the CB in which reverse current flows. This is the main difference from AC protection, where the CB near an AC bus is the fastest primary protection. However, this depends on the accuracy of distance evaluation algorithm, especially for a ground fault with grounding resistance. Hence an accurate and efficient fault distance evaluation method is required.

3) If the evaluated distance value is negative, that means the fault did not occur on this cable, so it will wait for a delay time (as shown the CB relay point (m) in

Figure 5.10, for the fault (*flt*), $v_{(m)} < v_{(r_m)}$, hence evaluated distance $x = d\,v_{(m)} / \left(v_{(m)} - v_{(r_m)}\right) < 0$).

Three typical fault condition coordination decision examples are shown in detail in Table 5.4 to better describe the decision process. 1) For loop cable fault f_3 in Figure 5.1, firstly the evaluated absolute distance range is used to classify all the relay points, where D is the cable length (e.g. 200 km in Figure 5.1). 2) Then for each category, the "+" distance relays are the primary protections because the fault is detected within its protection range. For others in this category, those only connected to a VSC source are in the second order, because if the primary protection CBs fail to trip, it can be seen as a bus fault, where the VSC definitely needs to be tripped. 3) The others in this category are ranked as the third order.

The ordering is carried on until all the categories are sorted to reach a tripping order result. These rules are the same as for a radial cable fault like f_1. However, for DC bus fault, it is different, as stated the CB near the faulted DC bus cannot isolate fault current flows through reverse diodes. Therefore if a relay evaluated distance is exactly the cable length D, its CB has the priority to trip primarily, e.g. relay $R_{[4]}$, $R_{[8]}$, and $R_{[12]}$ in Table 5.4 under bus fault f_2.

Communication may be needed for CB relays at the same DC bus but because they are physically close communication is practical. A cable ground fault with a large resistance is not as serious as a short-circuit fault and some time delay is permitted. But a ground fault on the DC bus can be precisely detected even without accurate grounding resistance evaluation. For example, it is easy for relay $R_{[2]}$ to identify a bus fault when the ground distance evaluation is exactly the same with $R_{[5]}$, $R_{[6]}$, and $R_{[7]}$. The cable length inductance ratio with typical grounding resistance can be used as a reference for a fuzzy decision. For instance, evaluated distance from $R_{[4]}$ may not be exactly D, but 1.5D. However, it still needs to trip first as the primary protection. A more accurate and faster DC ground fault location and resistance assessment has been proposed in Chapter 4.

Table 5.4: Protective Order Selection without Relay Communication

Loop Cable Fault f_3					Radial Cable Fault f_1					Bus Fault f_2				
Absolute Distance	Distance Sign	Radical Source only	CB Relay	Result Tripping Order	Absolute Distance	Distance Sign	Radical Source only	CB Relay	Result Tripping Order	Absolute Distance	Exact Distance	Radical Source only	CB Relay	Result Tripping Order
$\|x\| \le D$	+	N/A	[4]	1	$\|x\| \le D$	+	N/A	[7]	1	$\|x\| \le D$	$x = 0$	√	[2]	1
			[5]					[8]			$x = D$	N/A	[4]	2
	N/A	√	[1]	2		N/A	√	[2]	2				[8]	
			[2]			–	×	[5]	3				[12]	
	–	×	[3]	3				[6]			$x = 0$	×	[5]	3
			[6]		$D < \|x\| \le 2D$	N/A	√	[1]	4				[6]	
			[7]					[16]					[7]	
$D < \|x\| \le 2D$	N/A	√	[8]	4				[3]	5		$x = -D$	√	[1]	4
			[15]					[4]					[16]	
			[16]					[11]			$x = -D$	×	[3]	5
			[9]	5				[12]					[11]	
			[10]					[13]					[13]	
			[11]		$2D < \|x\| \le 3D$	N/A	√	[14]	6	$D < \|x\| \le 2D$		√	[14]	6
			[12]					[15]					[15]	
			[13]					[9]	7			×	[9]	7
$2D < \|x\| \le 3D$	N/A	√	[14]	6				[10]					[10]	

5.5 DC Wind Farm Protection Simulation Results

A simulation system of the proposed Supergrid section is modelled in PSCAD/EMTDC. Network parameters of the system are shown in Figure 5.1. The PMSG and VSC parameters are provided in Tables 5.5 and 5.6. A detailed frequency dependent phase cable model is employed in the simulations. The same DC cable π-model parameters in Table 5.2 are used for critical tripping time t_c calculations. The proposed protection scheme is applied to this specific DC wind farm system to show the protection results. The faults simulated are short-circuit faults and ground faults at the three selected points in Figure 5.1 and Table 5.4. After the faults occur, the VSC IGBTs are blocked for self-protection. The per unit power calculation uses 600 MW as base value for each grid-side VSI connected to an AC grid. Finally in Section 5.5.4, the aforementioned cable modelling comparison is also performed on this system for a short-circuit fault.

Table 5.5: PMSG Parameters

Parameter	Value	Parameter	Value
Rated power P_n	300 MW	Pole pair no. P_p	100
Rated stator voltage V_{sn}	99 kV	Phase resistance	0.068 p.u.
Rated frequency f_g	50 Hz	Phase inductance	0.427 p.u.

Table 5.6: VSC Parameters

Parameter	Value	
	Wind Farm VSC Rectifier	AC Grid VSC Inverter
Rating Power	300 MW	600 MW
DC Voltage	±100 kV	±100 kV
DC-link capacitance	10 mF	20 mF
Choke inductance	18 mH	22 mH
Transformer voltages	99 kV / 96 kV	96 kV / 110 kV

5.5.1 DC Radial Cable Short-Circuit/Ground Fault Condition

A short-circuit and a positive-side metallic ground fault are applied at f_1 (60 km from the VSI1) at t = 10.0s, respectively. Figures 5.11 and 5.12 are the fault overcurrents

without protection. In Figure 5.11, the total short-circuit fault current for VSI1 side $i_{(fault)}$ reaches more than 210 kA – up to 70 times of the rated value (3.0 kA for 600 MW wind power transmitted in ±100 kV voltage level). The main contribution comes from the discharge of the large DC-link capacitor. After the capacitor discharge phase, the most vulnerable component - diodes - suffer during the freewheel phase (short-circuit phase II in Table 5.1). The diode freewheel overcurrent phase happens after 28 milliseconds, with abrupt VSI current $i_{(VSI)}$ distributed in the three phase diodes $D1$, $D3$, and $D5$ as $i_{(D1)}$, $i_{(D3)}$, and $i_{(D5)}$. This abrupt overcurrent is about 5 times normal (from 15 kA to 75 kA). This has the most serious impact on the VSC-HVDC system and will immediately destroy the converter. At the same time, the AC-side grid currents will feed into the fault point through VSI1 diodes, which results in the oscillation and absorption of active and reactive power from the AC grids (shown in Figure 5.13).

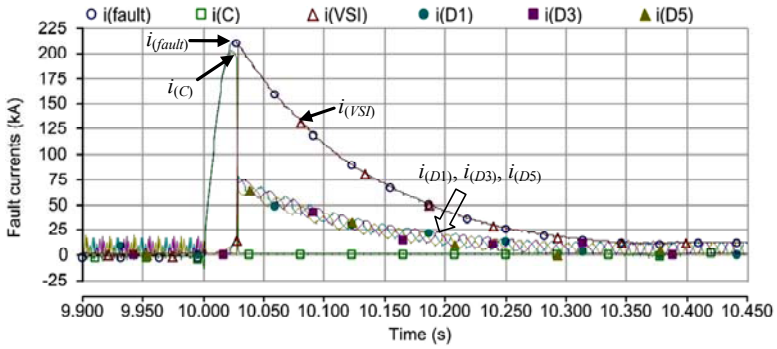

Figure 5.11: Short-circuit fault currents flow through the fault point f_1 $i_{(fault)}$, DC-link capacitor $i_{(C)}$, voltage source inverter $i_{(VSI)}$, and its three-phase diodes $i_{(D1)}$, $i_{(D3)}$, $i_{(D5)}$.

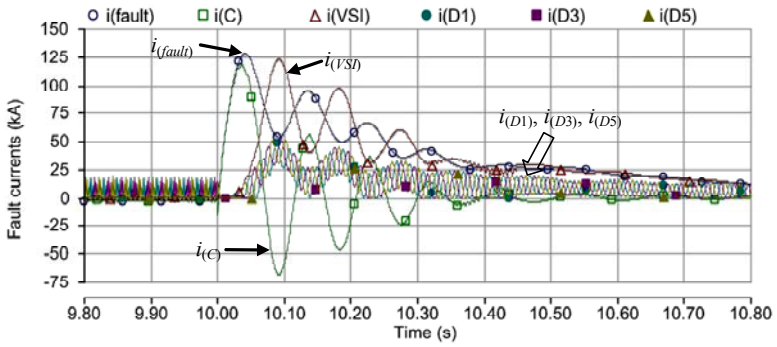

Figure 5.12: Ground fault currents flow through the fault point f_1 $i_{(fault)}$, DC-link capacitor $i_{(C)}$, voltage source inverter $i_{(VSI)}$, and its three-phase diodes $i_{(D1)}$, $i_{(D3)}$, $i_{(D5)}$.

For the positive cable ground fault, although it is metallic, the fault current is not as serious as the short-circuit condition – up to 125 kA in Figure 5.12, as the fault current loop has the transformer winding as a current limiter. Furthermore, there is no severe overcurrent through the freewheel diode. The diode currents increase gradually.

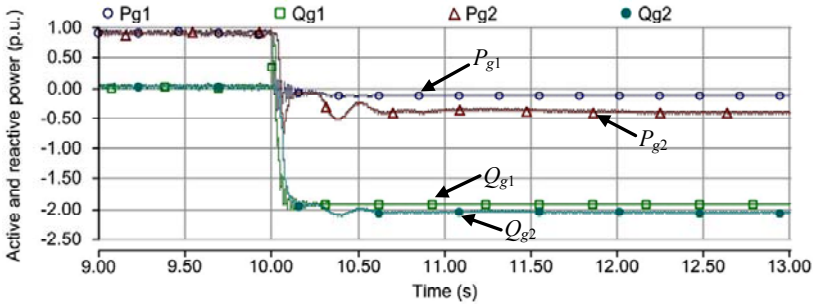

Figure 5.13: Active powers (P_{g1}, P_{g2}) and reactive powers (Q_{g1}, Q_{g2}) of the two grid-side VSIs under short-circuit fault f_1 without CB protection.

With immediate $CB_{[7]}$ and $CB_{[8]}$ tripping to clear the fault, and other CBs as backup protections for coordination, the system will still operate with all the power flows to AC Grid 2, P_{g2} about 1.80 p.u. – twice the value before fault, 0.90 p.u. (shown in Figure 5.14). The system will experience a transient period of a couple of seconds and then reach a new steady-state. There will be no overcurrents that threaten the system devices and all the wind farms still operate to supply power to the AC Grid 2.

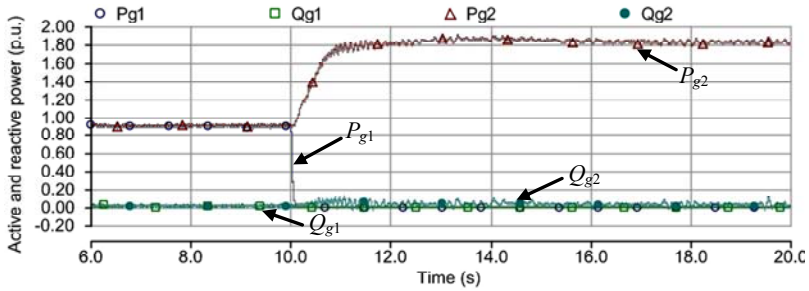

Figure 5.14: Active powers (P_{g1}, P_{g2}) and reactive powers (Q_{g1}, Q_{g2}) of the two grid-side VSIs under short-circuit fault f_1 with CB protection.

5.5.2 DC Loop Cable Short-Circuit/Ground Fault Condition

The fault overcurrents for this fault location are not shown; they are similar to the previous radial cable condition. Here the normal operation condition is introduced.

Because the network is symmetrical, for normal operation, there is no power flowing in the two link-cables (Cable 3 and Cable 4 in Figure 5.2), i.e. they are in stand-by condition. When the fault f_3 occurs on Cable 1, the power from Wind Farm 1 can flow from Cable 3. The tripping of $CB_{[4]}$ and $CB_{[5]}$ will separate the network as two radial branches: The power of Wind Farm 3 flows to AC Grid 1; while the power from the other three flows to AC Grid 2. Simulation results in Figure 5.15 show that the active power of AC Grid 1 P_{g1} reduced to around half of that before fault (from 0.90 p.u. to 0.45 p.u.). For AC Grid 2, the active power increases to 1.35 p.u., that is 3×0.45 p.u. It also takes about three seconds to reach the new state. During this process, the DC-link voltages of VSI1 and VSI2 are still in control, without large reactive power fluctuations.

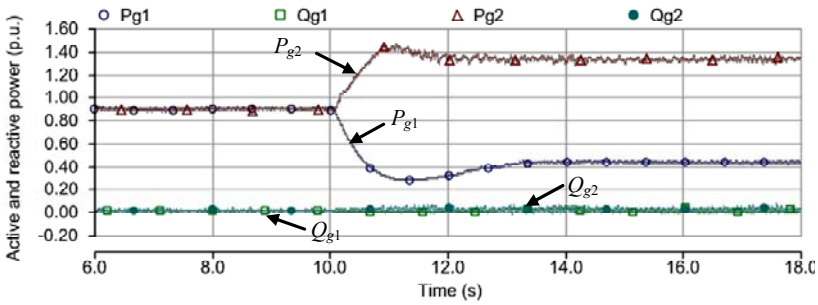

Figure 5.15: Active powers (P_{g1}, P_{g2}) and reactive powers (Q_{g1}, Q_{g2}) of the two grid-side VSI under short-circuit fault f_3 with CB protection.

5.5.3 DC Bus Short-Circuit/Ground Fault Condition

The DC bus fault f_2 with four connections through $CB_{[2]}$, $CB_{[5]}$, $CB_{[6]}$, and $CB_{[7]}$ will result in the tripping of the four CBs as shown in Table 5.4: $CB_{[2]}$, $CB_{[4]}$, $CB_{[12]}$, and $CB_{[8]}$. The protection performance of the resultant AC grid power flow is shown in Figure 5.16. The only cable connection – Cable 2 has to be tripped from $CB_{[8]}$ hence no power is delivered to AC Grid 1. At the same time, Wind Farm 2 has to be curtailed until the bus fault is cleared. However, the other three wind farms still have a cable route (Cable 3 – Cable 5 – Cable 6) for power transmission to AC Grid 2 – 1.35 p.u. in total.

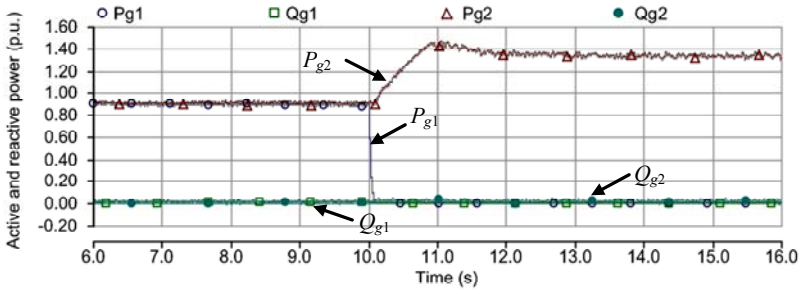

Figure 5.16: Active powers (P_{g1}, P_{g2}) and reactive powers (Q_{g1}, Q_{g2}) of the two grid-side VSI under short-circuit bus fault f_2 with CB protection.

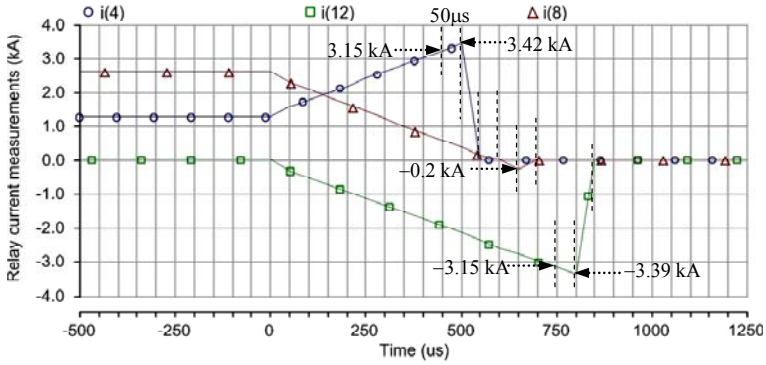

Figure 5.17: Relay current measurements under DC bus short circuit fault f_2 condition: relay $R_{[4]}$ current $i_{(4)}$, relay $R_{[12]}$ current $i_{(12)}$, and relay $R_{[8]}$ current $i_{(8)}$.

The three cables (Cable 1, Cable 2, and Cable 4) connected to DC $\text{Bus}_{(2)}$ will be protected from the tripping of $\text{CB}_{[4]}$, $\text{CB}_{[8]}$, and $\text{CB}_{[12]}$. Hence their relay current measurements are scaled to 50μs division (the simulation time-step) as shown in Figure 5.17 to observe the tripping decision procedure. The overcurrent relay threshold is set to be 2.10 p.u. (3.15 kA) for relay $R_{[4]}$ and $R_{[12]}$. The positive power flow direction is defined as: from $R_{[4]}$ to $R_{[5]}$ for Cable 1; from $R_{[6]}$ to $R_{[12]}$ for Cable 4. Therefore, in Figure 5.17, it takes about 450 μs for $R_{[4]}$ current $i_{(4)}$ to reach that value and then the tripping decision is simulated to be one time-step, i.e. 50 μs. Then the current increases to 3.42 kA, which is considered to be tolerable for the system for a short period of 50 μs. The CB fault current extinguishing time t_{CB} is also chosen to be 50 μs. The DC circuit breaker simulated is a self-defined PSCAD model of uni-directional IGBT/diode switch, with gate control from the relay system. The actual minimum extinction time for the IGBT is set as 50 μs in this case, which is adequate for commercial IGBT devices. Hence in total it takes 500 μs to actually

extinguish the fault current, much less than the freewheel effect time t_c = 54ms for the fault distance of 200 km [calculated from (2)].

For Cable 4, the power flows in the negative direction, and the overcurrent $i_{(12)}$ reaches –3.15 kA after 750 μs and then reaches a maximum of –3.39 kA. Hence in total it takes 800 μs to actually extinguish the fault current, still well below the calculated critical time t_c.

For Cable 2, the normal power flow is only in one direction towards the AC Grid 1. Therefore, as long as the directional element in relay $R_{[8]}$ detects negative current, it will send signal for CB tripping. In Figure 5.17, after crossing-zero, the negative current reaches –0.20 kA in one time-step, and then $CB_{[8]}$ immediately operated after t_{CB} = 50 μs.

The DC voltage measurements as the other detection criterion are shown as Figure 5.18. All three voltages collapse to zero rapidly within 50 μs. This also proves that the main protection is based on overcurrent detection, hence called overcurrent distance protection.

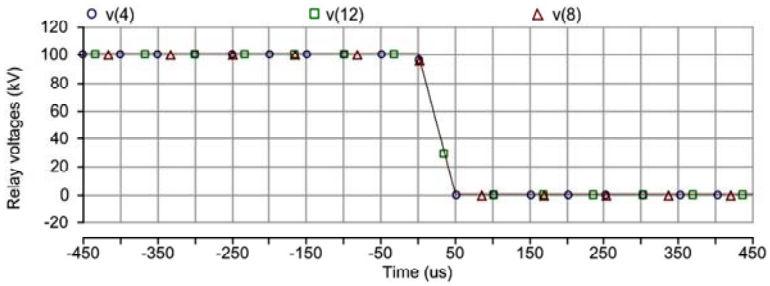

Figure 5.18: Relay voltage measurements under DC bus short circuit fault condition: relay $R_{[4]}$ voltage $v_{(4)}$, relay $R_{[12]}$ voltage $v_{(12)}$, and relay $R_{[8]}$ voltage $v_{(8)}$.

5.5.4 Cable Modelling Comparison

Simulation results of the cable short-circuit fault, f_1, with both detailed model and simple π-model are shown in Figure 5.19. The results with the two models are close, except that some high frequency components in the diode currents have a phase delay due to the single inductance value chosen for π-model. However, the diode freewheel overcurrent period and fault overcurrent amplitude are very close for

analysis and t_c calculation. The ground fault simulation results are not compared here because there is no abrupt change in diode current and the current oscillation pattern is similar to the example given in Figure 5.4.

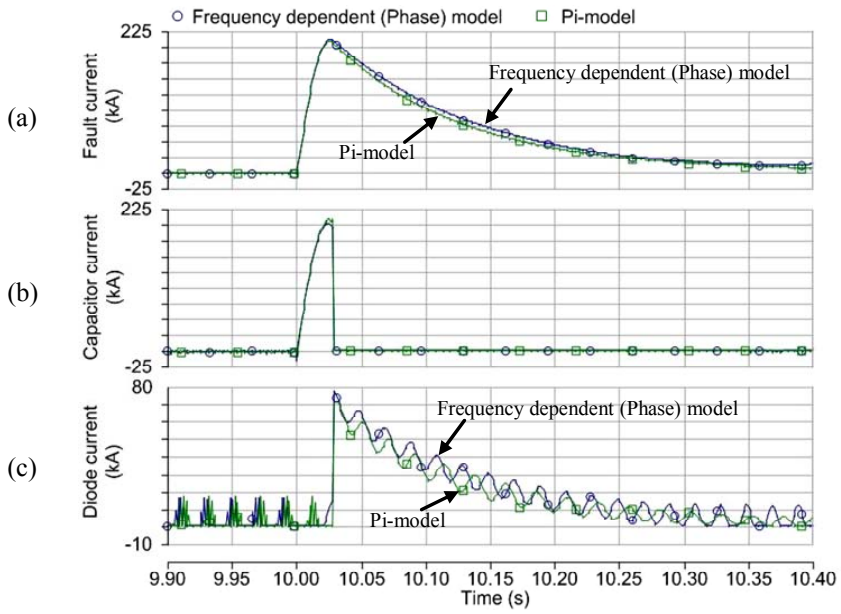

Figure 5.19: DC wind farm fault current simulation comparison with the two cable models: (a) the total cable fault currents; (b) DC-link capacitor discharging currents; (c) VSC diode freewheel currents (Phase-*a* diode).

5.6 Conclusion

This chapter discusses the design of a protection scheme for a meshed DC network topology for wind power grid integration. Key issues are introduced and possible solutions are presented based on a proposed typical network section. DC circuit breakers are allocated and configured with an appropriate coordination strategy. This protection scheme is defined in detail into several steps. Simulation results of three typical fault conditions are provided for verification. This new DC loop network protection is important for realising the future Supergrid.

The DC transmission network with onshore AC grid connections may have multi- and hybrid loops. For instance, one AC transmission cable connecting the two AC grid onshore substations in Figure 5.1 will form a hybrid loop with both AC and DC

connections. The AC and DC CB coordination issue needs to be considered due to the significant difference in operation time, as indeed does the protection influence on other AC CBs located around the onshore substations. Moreover, accurate and fast ground distance evaluation and grounding resistance assessment method is required for real-time coordination application.

5.7 References

[5.1] S. Gordon, "Supergrid to the rescue," *Power Engineer*, vol. 20, no. 5, pp. 30-33, Oct./Nov. 2006.

[5.2] T. Ackermann, "Transmission system for offshore wind farms," *IEEE Power Engineering Review,* pp. 23-27, Dec. 2002.

[5.3] N. Flourentzou, V. G. Agelidis, and G. D. Demetriades, "VSC-based HVDC power transmission systems: an overview," *IEEE Trans. Power Electron.*, vol. 24, no. 3, pp. 592-602, Mar. 2009.

[5.4] P. Bresesti, W. L. Kling, R. L. Hendriks, and R. Vailati, "HVDC connection of offshore wind farms to the transmission system," *IEEE Trans. Energy Convers.*, vol. 22, no. 1, pp. 37-43, Mar. 2007.

[5.5] D. Jovcic and N. Strachan, "Offshore wind farm with centralised power conversion and DC interconnection," *IET Gener. Transm. & Distrib.*, vol. 3, no. 6, pp. 586-595, Jun. 2009.

[5.6] P. M. Anderson, *Power system protection*. New York: IEEE Press, 1999.

[5.7] F. Lu, "Novel method for determining the optimal coordination sequence of directional relays in a complicated multi-loop power network based on coordination relationships between relays," *Journal of Automation of Electric Power Syst.*, vol. 29, no. 24, Dec. 2005.

[5.8] Q. Yue, F. Lu, W. Yu, and J. Wang, "A novel algorithm to determine minimum break point set for optimum cooperation of directional protection relays in multiloop networks," *IEEE Trans. Power Del.*, vol. 21, no. 3, pp. 1114-1119, Jul. 2006.

[5.9] M. Chinchilla, S. Arnaltes, and J. C. Burgos, "Control of permanent-magnet generators applied to variable-speed wind-energy systems connected to the grid," *IEEE Trans. Energy Convers.*, vol. 21, no. 1, pp. 130-135, Mar. 2006.

[5.10] M. E. Baran and N. R. Mahajan, "Overcurrent protection on voltage-source-converter-based multiterminal DC distribution systems," *IEEE Trans. Power Del.*, vol. 22, no. 1, pp. 406-412, Jan. 2007.

[5.11] D. Jovcic, and B. T. Ooi, "Developing dc transmission networks using dc transformers," *IEEE Trans. Power Del.*, vol. 25, no. 4, pp. 2535-2543, Oct. 2010.

[5.12] X. Liu, A. H. Osman, and O. P. Malik, "Hybrid travelling wave/boundary protection for monopolar HVDC line," *IEEE Trans. Power Del.*, vol. 24, no. 2, pp. 569-578, Apr. 2009.

[5.13] B. Gustavsen, G. Irwin, R. Mangelrod, D. Brandt, and K. Kent, "Transmission line models for the simulation of interaction phenomena between parallel ac and dc

overhead lines," *Int. Conf. on Power Sys. Transients*, Budapest, Hungary, 20-24 Jun. 1999.

[5.14] IEEE Standard 551, Chapter 7, Capacitor contributions to short-circuit currents, IEEE recommended practice for calculating short-circuit currents in industrial and commercial power systems, Oct. 2006.

[5.15] F. Mura, C. Meyer, and R. W. De Doncker, "Stability analysis of high-power dc grids," *IEEE Trans. Ind. Appl.*, vol. 46, no. 2, pp. 584-592, Mar./Apr. 2010.

[5.16] A. Ametani, "A general formulation of impedance and admittance of cables," *IEEE Trans. Power Apparatus and Sys.*, vol. PAS-99, no. 3, 902-910, May/Jun. 1980.

[5.17] W. Hu, Z. Chen, Y. Wang, and Z. Wang, "Flicker mitigation by active power control of variable-speed wind turbines with full-scale back-to-back power converters," *IEEE Trans. Energy Convers.*, vol. 24, no. 3, pp. 640-649, Sep. 2009.

Chapter 6

Reliability Enhancement of Offshore Wind Farms by Redundancy Analysis

6.1 Introduction

The optimisation of the wind power collection grid design aims to minimise large-scale offshore wind farms' influence on the main network. Therefore, the reliability of offshore wind farms needs to be assessed in detail because of the time- and financial- aspects of construction and maintenance access issues in the offshore environment. The wind farm reliability is distributed between the wind turbines, the wind power generation systems, and the collection and transmission systems [6.1]. However, detailed large-scale offshore wind farm failure statistics are lacking due to the short time of operational experiences [6.2]. Nevertheless, with the increasing capacity of wind farms in planning and construction, also the requirements of fault ride-through (FRT) capability to wind power generation systems from grid codes of many countries [6.3], it is quite urgent to enhance the reliability and system stability study of wind farm collection and transmission systems.

In terms of existing wind farm operational experience and wind farm failure survey, this chapter firstly discusses the topology and assessment of reliability for collection and transmission systems. Reliability is defined by taking into account the total curtailed power during fault conditions, device failure rate, and mean time to repair (*MTTR*), i.e. disrupted time.

Redundancy is a major way to enhance reliability of onshore distribution and transmission systems. In this chapter, redundancy degree for offshore wind farms is defined considering the redundant device voltage level, redundant cable to normal cable route ratio and redundant devices. The basis of redundant decision-making is

the operational experience of existing offshore wind farms, and the estimated cost data. The proposed method is used for an example practical offshore wind farm scenario. Optimal redundancy design can be achieved with the discussion of enhanced reliability and acceptable economic costs.

6.2 Wind Farm Collection/Transmission Systems and Reliability

6.2.1 Collection Grids

The system of offshore transformers and linking cables are called collection grids [6.4]–[6.6], or collector/collection systems [6.2], [6.7], [6.8]. Like onshore distribution network, the optimal voltage level for offshore wind farm is the medium voltage level, e.g. 33 kV in UK, in order to make a trade-off between the costs and technical performance.

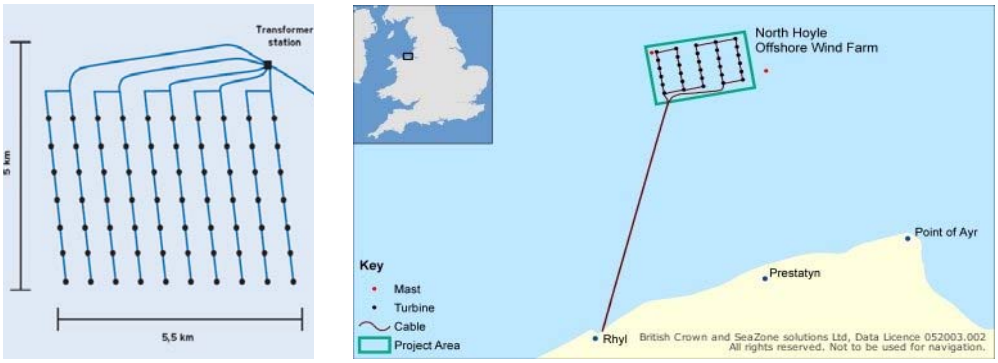

(a) (b)

Figure 6.1: (a) Horns Rev offshore wind farm (Denmark, built in 2002) [6.10]; (b) North Hoyle offshore wind farm (UK, in full operation since 2003) [6.11].

1) Transformer Platform Location(s):

For transformer platforms, most of the existing studies assume that the platform is outside the wind farm region. Reference [6.9] proposes an optimisation method for locating the transformer platform. The principal objective of the optimisation process is to minimise the total cable resources used to connect turbines to the transformer

platforms. The predictable result is that the geometric centre is the optimal position. However, platform outside the wind farm region is simple for consideration, easy for onshore connection, and is the case for almost all the existing offshore wind farms. Figure 6.1 shows two offshore wind farm collection grids. Figure 6.1(a) is the world's first offshore wind farm – Horns Rev offshore wind farm in Denmark. Figure 6.1(b) is the North Hoyle offshore wind farm built in the UK, with redundant cables.

2) Wind Turbine Connections:

Wind turbines in a wind farm are always divided into several groups, in connection forms of string or star. For star connection, the wind turbines in a star always share one common transformer to reduce space and investment. While for string connection, the wind turbines in a string have their own dedicated nacelle transformers. In fact, they are unanimously necessary. Therefore, most studies focused on the detailed string configurations, in which strings are commonly merged into pairs, so-called "forks" [6.6] as shown in Figure 6.1(a). However, there is no topology analysis in terms of the whole collection grids.

6.2.2 Transmission Systems

As discussed in the Chapter 1 literature review, the main decisions for the transmission system to the onshore grid are voltage level and whether the system is AC or DC. For reasons of transmission efficiency, it is always with a high voltage. This is similar to the onshore transmission system. AC or DC transmission is a major discussion until now. Because of the relatively high costs of high-voltage direct-current (HVDC) converters and switchgear, and spacious transformer platforms, AC transmission is preferable in current wind farm constructions, also owing to its mature technologies and operational experiences [6.12], [6.13]. However, the major disadvantage of AC transmission is the charging of cables so that there is a distance limit for power delivery. With larger offshore wind farms and greater distance from the grid, HVDC is promising for future wind farm power transmissions.

6.2.3 Wind Farm Collection and Transmission System Reliability Assessment

The probabilistic reliability index, expected energy not served (*EENS*), is used to assess the reliability of distribution and transmission systems [6.14]. It gives a measure of the amount of power to deliver that can be curtailed during fault conditions. Here the *EENS* of wind farm collection and transmission systems is defined as [6.4]

$$EENS = \sum_{i=1}^{N} \left(q_i \times P_i \times MTTR_i \right) \quad \text{(MWh/year)} \tag{6.1}$$

where N is the total number of components (including medium-voltage circuit breakers, disconnectors, switches, nacelle transformers, and cables). For component indexed i, q_i is the expected failure rate (frequency per year); P_i is the unavailable installed power during its failures; $MTTR_i$ is its mean time to repair.

6.3 Wind Farm Collection and Transmission System Redundancy Definition

There is no clear redundancy definition for wind farm collection and transmission systems since wind farm redundancy is still not well studied. In this section, after analysing existing redundancy choices, by dividing wind farm components into different levels, the redundancy definition of the wind farm system is given. It is the redundancy of collection grids, i.e. the power transmission between turbines and turbine-to-platform cables that requires detailed discussion. One aspect of redundancy concerns the topology. This means the energy that can flow through different paths during faults, instead of being interrupted. Another is in respect of the configuration of switchgear.

6.3.1 Topology Redundancy

Network topology generally includes redundancy. For main grids, this is referred to the power transmission capacity of cables/lines. Conventional transmission grids are

typically designed for "full redundancy" operation for the purpose of reliability. Similarly, the redundancy of wind farm transmission lines and substation transformers is analysed in [6.2] and [6.13]. Reference [6.13] proposes partial redundancy, considering that wind turbine generators only generate at full output for some of the time, with less risk that a capacity limitation will lead to significant loss of energy production. Meanwhile, in an offshore environment the cost of carrying redundant link-to-shore transmission capacity can be restrictive.

However, for collection grid redundancy, only a simple string structure redundancy has been proposed [6.5], [6.7], [6.15]. The simple redundancy lies in the dashed line in Figure 6.2(b). This is a typical "ring" configuration. Reference [6.15] studies the detailed string constructions to include redundancy lines at the end of strings. In a real projects, the North Hoyle offshore wind farm collection grid [Figure 6.1(b)] considered redundancy (with 3 rings), but this is a regular-shaped small offshore wind farm with only 30 wind turbines, 60MW in total [6.11].

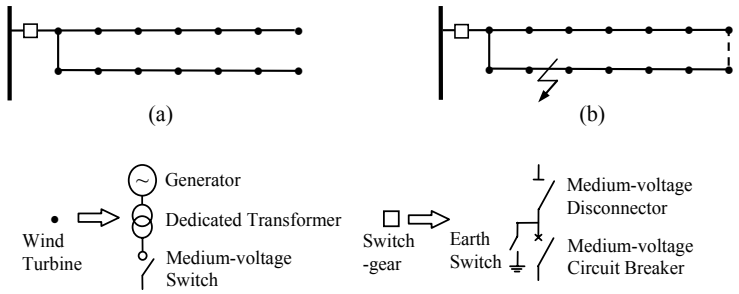

Figure 6.2: Illustration of collection string redundancy.

6.3.2 Device Redundancy

Figure 6.3 shows the difference of device redundancy with switchgear configuration [6.5]. This is in consideration of reducing switchgear costs. Figure 6.3(b) uses the same redundant cable to Figure 6.3(a) but fewer switchgear devices. The offshore environment needs vacuum circuit breakers or gas insulated switchgear, which are quite expensive and require more space volume than onshore conditions. The additional volume is itself costly in an offshore environment.

Figure 6.3: Illustration of device redundancy of collection string switchgear configuration.

Another kind of device redundancy is the transformer redundancy used in grid transmission systems. In substations, 2×70% total load capacity transformers are usually used instead of 1×100%. In this case, when one transformer needs to be repaired, there will still be 70% power supplied to customers, instead of losing all the supply with only one substation transformer.

6.3.3 Redundancy Definition

Redundancy of the wind farm collection and transmission systems is divided into three levels: collection grid level, platform level, and transmission level.

1) Collection Grid Level – Level 1:

As mentioned above, this level has both topology and device redundancy. In the collection grid, here are two kinds of redundant branches: between wind turbines, and between wind turbines and transformer platforms. Here only non-overlap redundant branches are considered (connecting wind turbine points without blocking or overlaying other branches), because in this condition the existing normal operation branches can be fully used (included in the new operational states after fault conditions). Each redundant branch needs switchgear and a protection relay system. In this chapter, the redundancy definition is based on the typical string-radial connection. For each string, usually there will be fewer than 10 wind turbines connected, considering the power limit of submarine cables and the turbine capacity. Example collection grids with 28 turbines in a rectangular area, and their redundant connections are shown in Figure 6.4.

The turbine-platform redundant branch depends on the location of platforms due to the string distribution. Figure 6.4 (a) and (b) illustrate two different string connections with different platform location. The normal operation branch numbers n_{norm} are both 28.

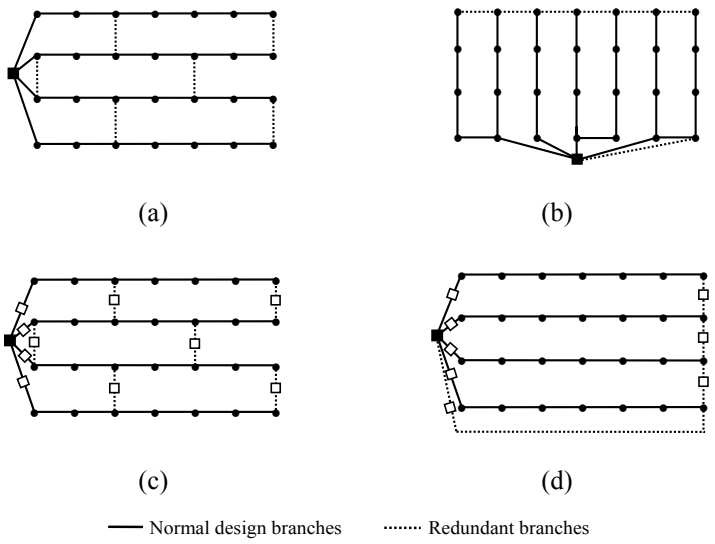

Figure 6.4: Illustration of redundancy allocation: (a) left-side platform with 4 string connection, with redundancy; (b) bottom-side platform with 4 string connection, with redundancy; (c) switchgear distribution; (d) with long redundant cable.

The number of redundant branches n_r can represent the redundancy degree. To normalise, this number is divided by the normal operation branch number, to give the redundancy degree parameter

$$\gamma_1 = 1 + n_r / n_{norm}. \tag{2}$$

So in the examples of Figure 6.4(a) and (b), the redundancy parameters are $\gamma_{1(a)} = 1+6/28 \approx 1.21$, and $\gamma_{1(b)} = 1+7/28 \approx 1.25$.

The existence of redundant branch switchgear makes the switchgear distribution different. Obviously, each redundant branch should have a switchgear system, and also for the strings to connect to the collection transformer, as shown in Figure 6.4(c). No more switchgear is required in normal branches. For the case of Figure 6.4(d), there is one redundant branch much longer than normal-size. This redundancy structure is proposed in [6.8]. Here this case is considered by the length $n_{long} \approx 6$. Use the normal-size branch cost C_{NB} and switchgear cost C_{SW}, so as to equivalence it into a normal-sized branch-switchgear pair.

$$n_{equ} = n_{long} \frac{C_{NB}}{C_{NB} + C_{SW}}. \tag{6.3}$$

If $C_{NB}/C_{SW} = 3$, $n_{equ} = 6\times3/4 = 4.5$, $\gamma_{1(c)} = 1+(4.5+4)/28 \approx 1.30$.

It seems simple to introduce redundant branches to strings because the only difference that can be made is whether to put a redundancy line there. In practice, for large-scale systems the redundancy can be much more complex. Like the case of Gwynt y Môr offshore wind farm [Figure 6.5, submitted in November 2005, consented in December 2008], the irregular layout and flexible location of transformer platforms make things intangible. Therefore, using a systematic approach to optimise collection grid planning/design can substantially decrease the amount of cost incurred.

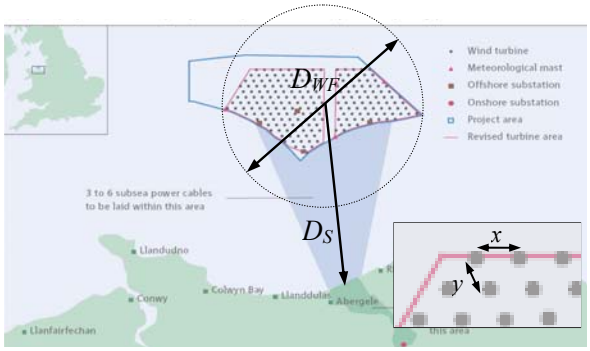

Figure 6.5: The layout features of Gwynt y Môr offshore wind farm (background picture from [6.16]).

In this complex scenario, the wind turbine of one group can be connected to the transformer or a turbine of another group. The wind turbines at each string terminal, if close to the other transformer platform, can be connected to it as a backup. This influence will lead to the change of γ_1 as

$$\gamma_1 = 1 + \left(\sum_{i=1}^{G} n_{ri} + 2n_{g-g} \right) \Big/ \sum_{i=1}^{G} n_{norm,i} \tag{6.4}$$

where G is the group number; n_{ri}, n_{norm}, and $n_{g\text{-}g}$ are the redundant, normal, and group-to-group branch numbers respectively. The number 2 means the group-to-group redundant branch introduces redundancy to both groups.

2) Platform Level – Level 2:

In this level, it is the platform transformer redundancy used as discussed before. This is the same with traditional substation transformer redundancy, e.g. normally γ_2 = 1.4.

3) Transmission System Level – Level 3:

This level redundancy degree γ_3 is very similar to the level-1 redundancy. But the differences are the voltage level and much smaller number of platforms and onshore substations. Also, the cost of long transmission cables makes redundancy even more uneconomical. So the number of options for redundancy design is much more limited at this level.

The total redundancy can be defined by multiplying the redundancy degrees of each level

$$\gamma = \prod_{i=1}^{3} \gamma_i \,. \tag{6.5}$$

6.4 Wind Farm Redundancy Design

6.4.1 Offshore Wind Farm Layout Feature

The position of wind turbines in a wind farm is determined by assessing environmental condition and wind resources, to maximise the wind resource utilisation accounting for environmental impact. Therefore, it is not part of the configuration options in this chapter. But the features of this layout will generally influence the final choice of collection grid and transmission lines. The basic features are summarised and shown in Figure 6.5.

The area of a wind farm project is always concentrated in a local area with respect to its distance to the onshore substation. This can be evaluated by the wind farm to-shore-Distance (D_S) / geometric area Diameter (D_{WF}) Ratio (DDR):

$$DDR = D_S / D_{WF}. \tag{6.6}$$

The distance between wind turbines are represented by a parallelogram with x, y as side lengths (normally $x = y$).

6.4.2 The Design Process Description

The proposed optimisation procedure is illustrated in Figure 6.6. First, based on the fixed wind farm layout, choose transformer platform location(s). Second, design the normal operation string structure with cost limit consideration as traditional works. Third, in three levels (collection grid, platform, and transmission system), perform redundancy design. After the analysis of reliability and economic cost assessment comes the study of the optimal redundancy degree with detailed redundancy configuration.

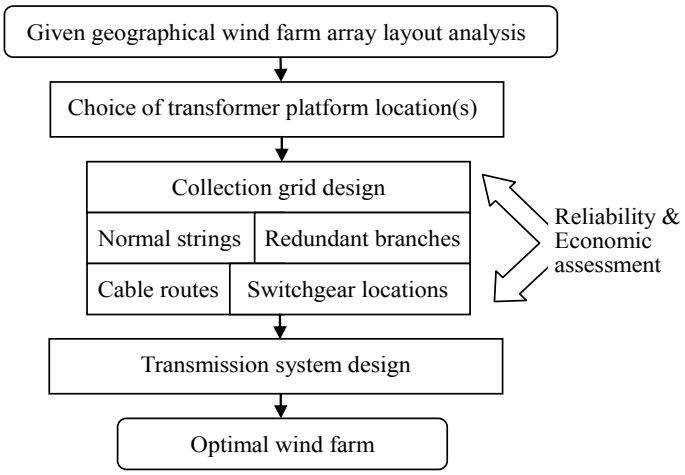

Figure 6.6: Flow chart of wind farm design process.

6.4.3 Choice of Transformer Platform Number and Location

The choice of appropriate platform number and location depends on the total number of wind turbines and the required capacity of the transformers.

1) Number of Platforms:

The transformer platforms can also have redundancy, but due to the cost of building platforms and the space limit, platform number redundancy is not considered here.

However, transformer redundancy can be considered as discussed before. That is to say, only total installation capacity is considered. Wind turbines are divided into this number of groups. After dividing wind turbines into several groups (usually 20-30 wind turbines in each group), each group is allocated a platform.

2) Platform Location(s):

The choice of each platform location – the principal objective of the optimisation process is to minimise the total length of medium-voltage cable used to connect the turbines to the transformer platforms. The transformer substations are always located near the onshore substation side to minimise the high-voltage transmission cable length. If this *DDR* is large (for example 4-8), this means the diameter can be neglected against the distance, so the transformer substation can be located near the onshore side edge of the wind farm. If *DDR* is small (<1, and predictably the case for connecting some large-scale offshore wind farms along a coastline), using the geometric centre is more optimal, as shown in [6.9]. In Figure 6.7, for Gwynt y Môr offshore wind farm, the positions of platforms are chosen, so the group is divided as in Figure 6.7.

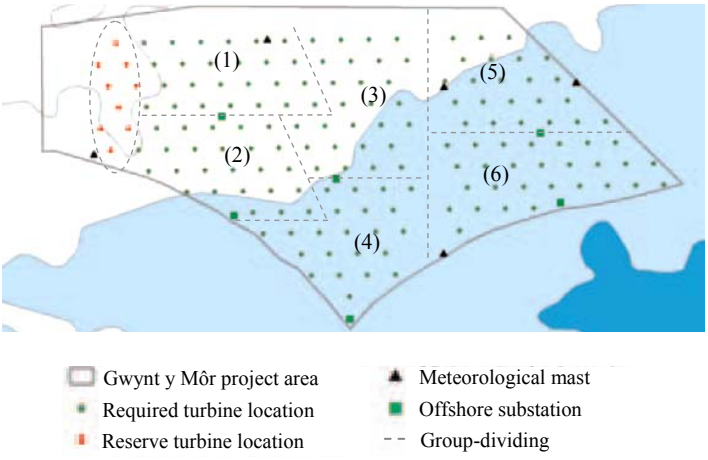

Figure 6.7: The group-dividing and transformer platform locations (background picture from [6.16]).

6.4.4 Normal Collection Grid Topology Design

The collection grid is firstly designed without redundancy. For each group, the wind turbine is connected to platforms in strings to form a radial tree system. There has been research about normal collection grid topology design, including normal optimisation method [6.9] and genetic algorithms (GA) method [6.17]. The former is used here. The strings can be evolved from the substations as trees including the shortest distance from each wind turbine to the next point (substation or wind turbine). Normally, each string includes less than 10 wind turbines. Figure 6.8 and Table 6.1 show an example of normal collection grid design.

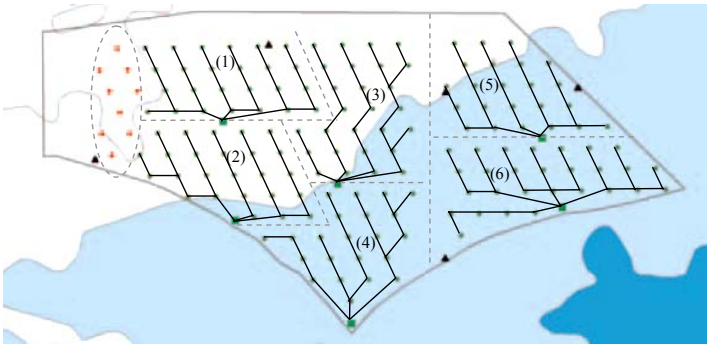

Figure 6.8: Normal collection grid string design.

Table 6.1: Group Division and Normal Collection Grid Design

Group	WTG No.	Normal Branch No. n_{norm}	Group	WTG No.	Normal Branch No. n_{norm}
1	25	25	4	22	22
2	25	25	5	23	23
3	27	27	6	28	28
Total	250	250			

6.4.5 Redundancy Design

1) Collection Grid Level – Level 1:

First, connect the platform to the nearest turbines of a neighbour group, if they are not in a same string. The cable loading is limited to connecting 10 turbines.

Therefore, then connect the terminal turbine in a string with the smallest number of turbines to the neighbour group with almost 10 turbine in its string. During this process, the redundant branch should not be longer than $2x$.

Each group itself requires redundancy. This is similar to traditional string redundancy study, but much more flexible with the above among-group redundancies. After the group-to-group connection, the objective of this step is to make sure each turbine has two connections. So it is required to check turbines with only one connection, and then connect it to the nearest turbine. For example, in Figure 6.9, if there are 13 group-to-group branches, for each group, the redundant branch number is $n_{r1} = 6$, $n_{r2} = 4$, $n_{r3} = 4$, $n_{r4} = 2$, $n_{r5} = 3$, $n_{r6} = 4$. In this condition, all the normal branches can be switched out without any power curtailed. The redundancy parameter γ_1 becomes 1.196, which is the maximum level-1 redundancy in this example. The final collection grid design is shown in Figure 6.9. Longer redundant lines (>$2x$) are not preferable in this case.

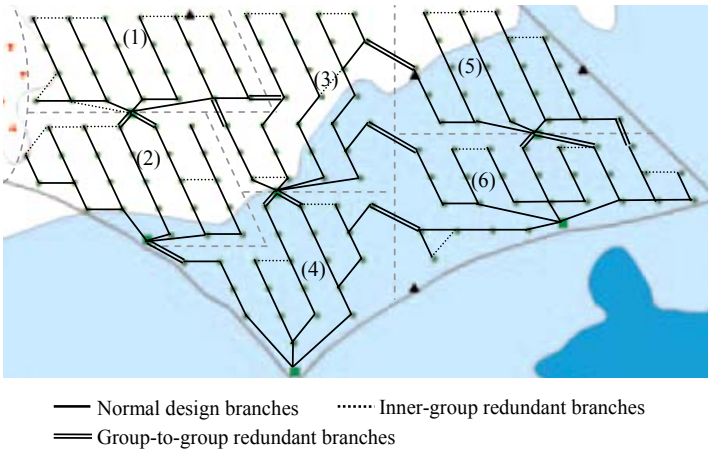

Figure 6.9: Collection grid redundancy design, $\gamma_1 = 1.196$.

2) Platform Level – Level 2:

As mentioned previously, the redundancy degree $\gamma_2 = 1$ to 1.4.

3) Transmission System Level – Level 3:

Figure 6.10 shows the normal transmission cables and potential redundant cable routes in the example wind farm.

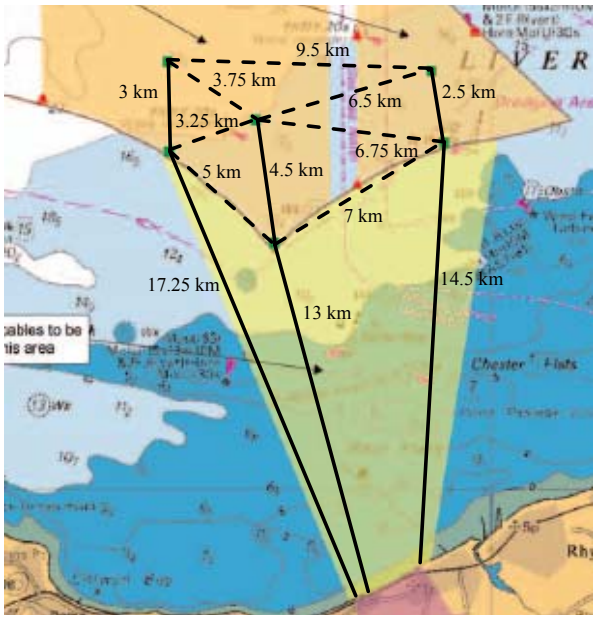

Figure 6.10: Transmission system design (background picture from [6.16]).

The transmission cables are also firstly designed without redundancy and then the redundant transmission cables chosen. If the *DDR* is very small, and if there are many large-scale offshore wind farms close to each other, the "Supergrid" can be economically realised. So in terms of voltage level, the redundancy degree ranges from "Supergrid" – to connect the wind farms along one coastline area together to make a high voltage network – to only adding medium voltage redundant lines between wind turbine strings, as shown in Figure 6.10.

6.5 Example Wind Farm Design Analysis

The above Gwynt y Môr offshore wind farm is used as the example system for the proposed design method. The total power capacity will be 750 MW. Here choosing 3 MW wind turbines for the wind farm, there are 250 turbines in total, as shown in Figure 6.7. For the layout feature, here use $x = y = 1$ km. *DDR* is about 1.03 due to the given D_S (about 17.5 km) and D_{WF} (about 17 km).

6.5.1 Reliability Assessment

The reliability is assessed by *EENS* defined in (6.1). The failure rates and *MTTR* for offshore wind farm devices are listed in Table 6.2.

Table 6.2: Failure Rates and MTTR for Offshore Wind Farm Devices [6.4]

Offshore Wind Farm Component		Failure Rate q_i (per year)	$MTTR_i$ (h)
Wind turbine tower	Nacelle transformer	0.0131	240
	120 m tower cable	0.015 (per km)	240
	Medium-voltage switch	0.025	240
Collection grid	Medium-voltage circuit breaker	0.025	240
	Medium-voltage disconnector	0.025	240
	Medium-voltage submarine cable	0.015 (per km)	1440
Platform	Transformer	0.0131	240
Transmission system	High-voltage submarine cable	0.015 (per km)	1440

6.5.2 Economic Assessment

The detailed device cost information is usually confidential, so here the estimated split construction expenditure of North Hoyle offshore wind farm is used, Tables 6.3 and 6.4. Considering the device difference and number of devices in Table 6.4, an estimate of the per unit device costs for Gwynt y Môr wind farm is listed in Table 6.5.

Table 6.3: North Hoyle Offshore Wind Farm Information [6.18]

Component		Attribute	Quantity
Wind Turbine Generators (WTGs)		Vestas V80, 2 MW	30
Cable	Transmission cables (2)	Diameter 139 mm, 37 kg/m	10.781 km, 13.176 km
	Collection grid cables	Diameter 105 mm, 21 kg/m	350 m (North-south) 800 m (East-west)
Wind farm area			10 km^2

Table 6.4: Estimated North Hoyle Wind Farm Construction Expenditure [6.18]

Component		Estimated Cost (£ million)
Civil	Manufacture, supply and install WTG foundations	15.5
	Cable laying offshore	5.5
Electrical	Cable supply	4.0
	Supply and installation of substation equipment	1.5
WTGs	Supply and install WTGs	40.0

Note: The onshore components and other costs (management, distribution network connection, consultant, etc.) are omitted here.

Table 6.5: Estimated Offshore Wind Farm Component Per Unit Costs

Component		Total Cost (£ million)	Estimated Per Unit Cost (£ million)	
WTGs	Foundations	15.5	1.85 (per WTG)	
	Supply and install	40.0		
Cables	Cable supply	4.0	Collection grid cable	0.376 (per km)
	Cable offshore laying	1.5	Transmission cable	0.50 (per km)
Supply and installation of substation equipment		1.5	Transformer	0.75
			High-voltage switchgear (2)	0.25
			Medium-voltage switchgear (2)	0.125

During the cost estimation, the substation costs are split between the collection transformer and switchgear to strings, as well as onshore transmission lines. Given that transformer and cable costs increase with capacity, the relation between cost and capacity is estimated to be linear. Cable costs increase with cable length, cable overload capability, and additional switchgear. In [6.7] the foreign exchange rates and inflation factors are taken in to account, but these factors are not considered in this chapter.

6.5.3 Summary and Comparison

Different redundancy degrees are considered and compared. The incurred reliability costs are estimated in British pounds or million pounds per MWh/year (£ million per MWh/year). This data is also not applicable, so for each level, choose four proper

values to compare with the required extra device costs. The extra device quantity, redundancy degree, increased cost and *EENS* costs are shown below: Level 1 – Table 6.6 and Figure 6.11, Level 2 – Figure 6.12, Level 3 – Table 6.7 and Figure 6.13.

Table 6.6: Level 1 - Device Cost Increase and EENS with Different Redundancy

$n_{g\text{-}g}$	n_r	γ_1	Cost Increase (£ million)	*EENS* (MWh/year)
0	0	1.000	0	70662
2	4	1.032	4.506	52632
4	7	1.060	8.511	40602
5	9	1.076	11.216	33504
7	12	1.104	13.719	24774
10	18	1.152	17.728	12622
13	23	1.196	21.036	4470

$n_{g\text{-}g}$ – the number of group-to-group redundant cables;

n_r – the number of inner group redundant cables.

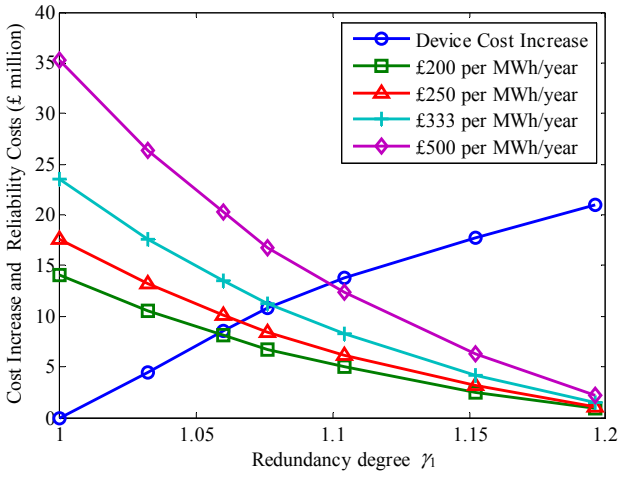

Figure 6.11: Collection grid level – level 1 cost and reliability analysis (different £ per MWh/year values represent different conditions of cost incurred on average for an MWh loss per year).

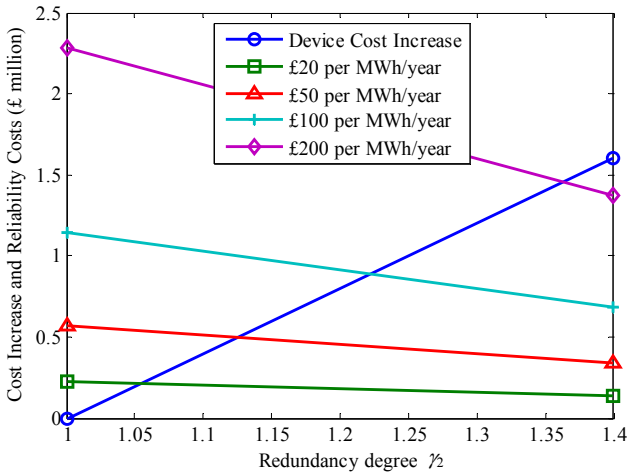

Figure 6.12: Platform transformer level – level 2 cost and reliability analysis (different £ per MWh/year values represent different conditions of cost incurred on average for an MWh loss per year).

Table 6.7: Level 3 - Device Cost Increase and EENS with Different Redundancy

Redundant Cable length (km)	Switchgear No.	γ_1	Cost Increase (£ million)	*EENS* (MWh/year)
0	0	1.000	0	282744
3.75	2	1.081	13.375	88269
11.50	4	1.234	20.750	9600
22.25	8	1.455	41.906	0

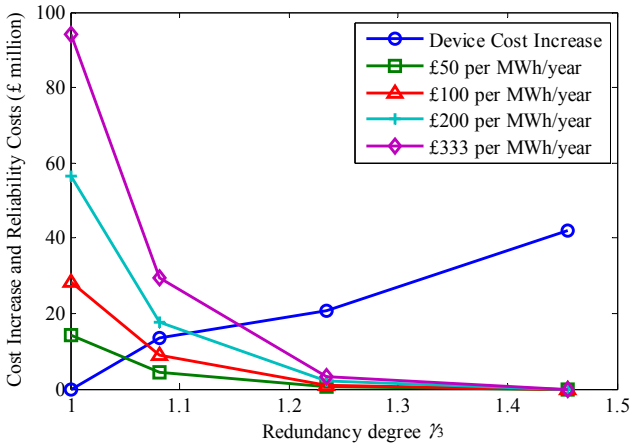

Figure 6.13: Transmission system level – level 3 cost and reliability analysis (different £ per MWh/year values represent different conditions of cost incurred on average for an MWh loss per year).

Collection grid (level-1) redundancy design has many options so here we use seven points; platform assessments (level-2) use two points to show the linear relationship; for transmission system (level-3), due to the limited options, four points are shown. From the above comparison, if the *EENS* loss information is available, the optimal redundancy degree can be found at the point of reliability cost curve across the increased device cost curve. The total maximal redundancy $\gamma = 1.196 \times 1.4 \times 1.455 = 2.436$ can be considered as the full redundancy condition.

In [6.19], it is mentioned that the fault likelihood and the associated costs are assumed to be lower than the costs for the additional devices. Therefore, redundancy is not taken into consideration. This may be true for small wind farms. But the comparison results show that redundancy is necessary for large-scale offshore wind farms due to economic aspects.

This systematic design method is in favour of comparing numerous options for complex offshore wind farm electrical system design. In addition, the results of AC and DC wind farms can be compared to explore the difference related to the diverse cost distribution among equipment, foundations and space, and individual device reliabilities. Hence it will be helpful for DC wind farm design, notwithstanding the disadvantage of high-cost DC devices. However, key to this method is accurate offshore wind farm operation statistics and detailed AC and DC equipment costs for accurate optimisation results.

6.6 Conclusion

The growing scale of future offshore wind farms makes reliability enhancement important during the planning and design phases. After analysing the importance and necessity of redundancy in wind farm collection and transmission systems, a detailed systematic redundancy design method is proposed and described from both technical and economic standpoints. The syntheses of cost and reliability measures are defined. The final degree of redundancy can be achieved using reliability and economic loss statistics. Results show that the balance between reasonable investment in

redundancy and the reliability of offshore wind farms can be analytically reached. More practical operational statistics and economic analysis are required for future modern wind farm applications, especially for large-scale DC offshore wind farm scenarios.

6.7 References

[6.1] P. J. Tavner, J. Xiang, and F. Spinato, "Reliability analysis for wind turbines," *Wind Energy*, in Wiley Interscience, vol. 10, pp. 1-18, 2007, [Online]. Available: http://www3.interscience.wiley.com/cgi-bin/fulltext/112701014/PDFSTART

[6.2] R. A Walling and T. Ruddy, "Economic optimization of offshore wind farm substations and collection systems," *5th Int. Workshop on Large-Scale Integration of Wind Power and Trans. Networks for Offshore Wind Farms*, Glasgow, UK, Apr. 7-8, 2005.

[6.3] A. I. Estanqueiro, J. M. Ferreira de Jesus, J. Ricardo, Amarante dos Santos, and J. A. Peças Lopes, "Barriers (and solutions...) to very high wind penetration in power systems," in *Proc. of IEEE Power Eng. Society General Meeting*, Tampa, Florida, USA, Jun. 24-28, 2007.

[6.4] A. Sannino, H. Breder, and E. K. Nielsen, "Reliability of collection grids for large offshore wind parks," in *Proc. of the 9th Int. Conf. Probabilistic Methods Appl. to Power Syst.,* Stockholm, Sweden, Jun. 11-15, 2006.

[6.5] B. Franken, H. Breder, M. Dahlgren, and E. K. Nielsen, "Collection grid topologies for off-shore wind parks," in *Proc. of the 18th Int. Conf. Electricity Distribution*, Turin, Italy, Jun. 6-9, 2005.

[6.6] L. Liljestrand, A. Sannino, H. Breder, and S. Thorburn, "Transients in collection grids of large offshore wind parks," *Wind Energy*, in Wiley Interscience, vol. 2, pp. 1-12, Jul. 2007, [Online]. Available: http://doi.wiley.com/10.1002/ we.233

[6.7] J. Green, A. Bowen, L. J. Fingersh, and Y. Wan, "Electrical collection and transmission systems for offshore wind power," *Offshore Technology Conference*, Houston, Texas, USA, Apr. 30-May. 3, 2007. Available: http://www.nrel.gov/wind/pdfs/41135.pdf

[6.8] G. Quinonez-Varela, G. W. Ault, O. Anaya-Lara, and J. R. McDonald, "Electrical collector system options for large offshore wind farms," *IET Renew. Power Gener.*, vol. 1, no. 2, pp. 107-114, Jun. 2007.

[6.9] P. D. Hopewell, F. Castro-Sayas, and D. I. Bailey, "Optimising the design of offshore wind farm Collection networks," in *Proc. of the 41st International Universities Power Eng. Conf.*, pp. 84-88, Newcastle-upon-tyne, UK, Sep. 6-8, 2006.

[6.10] VATTENFALL Company. 2007. http://www.vattenfall.com/www/vf_com/vf_com/Gemeinsame_Inhalte/DOCUMENT /360168vatt/569396horn/P0277546.pdf

[6.11] Npower renewables. North Hoyle offshore wind farm. http://www.npower-renewables.com/northhoyle/components.asp

[6.12] H. Brakelmann, "Efficiency of HVAC power transmission from offshore-windmills to the grid," *IEEE PowerTech Conf.*, Bologna, Italy, Jun. 23-26, 2003.

[6.13] A. B. Morton, S. Cowdroy, J. R. A. Hill, M. Halliday, and G. D. Nicholson, "AC or DC? Economics of grid connection design for offshore wind farms," in *Proc. of the 8th IEE Int. Conf. on AC and DC Power Transmission*, pp. 236-240, Melbourne, Vic., Australia, Mar. 28-31, 2006.

[6.14] J. Choi, T. D. Mount, R. J. Thomas, and R. Billinton, "Probabilistic reliability criterion for planning transmission system expansions," *IEE Proc. Gener. Trans. Distri.*, vol. 153, no. 6, pp. 719-727, Nov. 2006.

[6.15] P. Gardner, L. M. Craig, and G. J. Smith, "Electrical systems for offshore wind farms," in *Proc. of the 20th British Wind Energy Association Wind Energy Conf.*, Cardiff, UK, Sep. 1998.

[6.16] Npower renewables. Gwynt y Môr offshore wind farm. http://www.npower-renewables.com/gwyntymor/index.asp

[6.17] M. Zhao, Z. Chen, and J. Hjerrild, "Analysis of the behaviour of Genetic Algorithm applied in optimization of electrical system design for offshore wind farms," in *Proc. of 32nd Annual IEEE Conf. Ind. Electron.*, pp. 2335-2340, Paris, France, Nov. 6-10, 2006.

[6.18] J. M. F. Carter, "North Hoyle offshore wind farm: design and build," *Proc. of the Institution of Civil Engineers, Energy 160 Issue ENI*, pp. 21-29, Feb. 2007. Available: http://www.atypon-link.com/doi/pdf/10.1680/ener.2007.160.1.21

[6.19] T. Ackermann, "Transmission system for offshore wind farms," *IEEE Power Engineering Review,* vol. 22, no. 12, pp. 23-27, Dec. 2002.

Chapter 7

Conclusions and Future Work

7.1 Conclusions

Reliable protection systems for offshore wind farms are a prerequisite for the development of this renewable energy industry. However, due to lack of operational experience, this is a relatively new area of research. In this thesis, the protection issues related to wind power generation systems, collection grids and transmission systems are investigated. The contributions of this thesis in the context of wind power system protection are summarised as follows.

- Detailed performance analyses during various fault conditions of two popular variable-speed wind power generation systems – doubly-fed induction generator (DFIG) (in Chapter 2) and permanent magnet synchronous generator (PMSG) (in Chapter 3) are reported. Appropriate protection schemes are proposed for different topologies in order to protect the vulnerable power electronic converters. For DFIG, rotor overcurrent expressions are derived for various fault conditions. Based on that, a new series dynamic resistor-based protection circuit is proposed to protect the rotor-side converter without short-circuiting the rotor winding. This is advantageous in avoiding grid voltage deterioration from reactive power absorption, compared with conventional crowbar protection. Used in line with the traditional crowbar and DC-chopper protection, the proposed method can greatly enhance the DFIG system fault ride-through capability. Comprehensive PSCAD/EMTDC simulation studies are carried out as verifications. For PMSG, the protection systems are aimed at reducing the DC-link overvoltages caused by interruption

of the power transmission route. Both large-scale and small-scale topologies are studied for possible stand-alone or offshore applications. Series and parallel topology and DC or AC side resistor allocation options are examined and compared by simulation work. Application of pitch control for large-scale wind turbine to reduce overspeed effect due to electrical faults is also included in rotor shaft protection.

- The PMSG-based wind power generation system is expanded into a radial DC wind farm. In terms of wind farm collection and transmission systems, DC system protection schemes based on traditional AC network protection principles are presented in Chapter 4. DC switchgear allocation is illustrated with typical wind farm connection examples. The currently promising voltage-source conversion technology is investigated in detail for fault overcurrent analysis and critical stage definitions. This nonlinear system analysis not only defines the most critical stages that need to be avoided, but also instructs fault location. For small-scale radial wind farm collection systems, a coordination method without using communication devices between distant cable circuit breakers is proposed with a simple option of reverse-diode protection. Based on the fault analysis, a fault location method for ground fault conditions is proposed in particular. This fault location method is immune to variations in the relatively large ground fault resistances, distances, and system operation conditions, to effectively realise protection coordination.

- In Chapter 5, for large-scale wind farm integration, a typical meshed HVDC transmission system section is presented for DC fault protection design and test, in order to realise a reliable DC network for wind power connections. This topology includes multi- onshore grid connections and loop cable routes. Simulation system is built in PSCAD/EMTDC environment. With economic uni-directional current-blocking power electronic circuit breakers, a new protection coordination scheme is proposed for loop cable faults, radial cable faults, and DC bus faults. Special coordination between circuit breakers at the terminals of the same cable under DC bus faults is performed. Detailed

frequency dependent cable model is considered and compared with π-model which is used for theoretical analysis. Results show that for fault conditions, π-model is adequate for overcurrent analysis. The system reliability and power delivery capability under fault conditions are improved by effective fault isolation and possible loop power delivery routes.

- In Chapter 6, for the purpose of enhancing system reliability redundancy is introduced into wind farm planning. Wind farm reliability and redundancy degree are defined to describe a redundant system topology. After analysing the importance and necessity of redundancy in wind farm collection and transmission systems, a detailed systematic redundancy design method is proposed and described from both technical and economic standpoints. The final degree of redundancy is optimised using reliability economic loss statistics. With reasonable investment in redundancy, the reliability of offshore wind farms can be significantly improved.

In conclusion, the wind power generation system protection problems introduced in this thesis and the solution investigations seek to contribute to both the understanding and applications of protection in the field of large-scale offshore wind power integration to existing onshore power networks. From the perspectives of individual wind power generation systems, to an entire wind farm, even multiple large-scale wind farm connection systems, the electrical fault analysis and protection issues are discussed systematically. Future research aspects of this topic are discussed for the promising high-power DC network applications.

7.2 Future Work

Possible future work is listed as follows:

- Experimental test rig for protection system design is required to verify the protection schemes proposed in this thesis. However, this depends on the effective fault simulation hardware for this potentially destructive experiment.

Real-time simulation software or real-time digital simulator (RTDS) are possible ways to perform system fault and relay coordination simulation. For computer simulation, appropriate simulation software or even development of dedicated simulation modelling for fault analysis are required for efficient large-scale system simulation and real-time applications. The analysis of PMSG demagnetisation during fault conditions should be performed in detail as well.

- Research on multi-terminal DC network for wind power collection and transmission still requires more detailed work. In particular, the development and implementation of fault tolerant high-power voltage-source converters, for example those based on a multi-modular converter, and solid-state DC/DC step-up converters, with high efficiency and power control performance could be considered. For example, resonant converter applications for connection of systems at different DC voltage levels.

- Reliable and high-current interruption performance DC circuit breakers based on power electronic devices are urgently required. Detailed topology and associated relay system design should be tested at realistic power levels. This is prerequisite for application to large-scale DC networks in the future. Appropriate fuse should also be chosen for DC application as backup for circuit breaker switchgear systems.

- DC cable fault location methods should be tested with practical measurement sensors to verify their robustness and accuracy thereby providing the possibility of proposing improved algorithms. This is important for the industrial application of the proposed fault location method.

- More specific and dedicated wind farm construction and operational cost statistics and analysis are required for more accurate economic analysis and general planning instruction, in order to make a reasonable balance between the topology redundancy and system reliability. Wind power economics is a new area of academic research.